School of Biosciences

Sensing local biological environments using coherent optical nanoscopy

Dafydd Sion Harlow

PhD Thesis
School of Biosciences
Cardiff University

July 28, 2022

Contents

List of Figures

List of Tables

Abstract

Vibrational microscopy, specifically coherent anti-Stokes Raman scattering (CARS), has emerged in recent years as a very powerful imaging technique. CARS provides the user with a chemically specific, label free, means of imaging with three dimensional spatial resolution at video rates, close to the diffraction limit. Although increasingly promising, CARS is subject to two notable drawbacks, in addition to it's diffraction limit, hindering it's ability to sense materials at the nanoscale. Firstly, in the detection of CARS signal there is a significant non-resonant background contribution, and secondly there needs to be a large number of oscillators in the focal volume to generate a detectable signal. This thesis explores a novel heterodyne dual polarisation epi-detected coherent anti-Stokes Raman scattering technique (eHCARS), in the vicinity of plasmonic gold nanorod structures, aimed at pushing the resolution and sensitivity limits of this chemically specific label free technique down to the nano scale, whilst suppressing CARS non-resonant background and incoherent background.

Interferometric detection allows the shot noise limited CARS field to be detected (amplitude and phase) separated from non-resonant contributions. The eHCARS signal is measured from various sized silicone oil droplets, suspended on a glass substrate, exploring the signal generation pathways resulting from the interfaces of materials with differing linear and non-linear susceptibilities. Silicone on glass chosen as the oil has a molecular resonance peak close to the molecular resonances of biological materials.

The local surface plasmon resonance (LSPR) from plasmonic gold nanorods (NRs) are investigated. Specifically of interest as they provide local field enhancement in the vicinity of CARS, enhancing the CARS signal allowing the detection of weaker CARS signals, meaning the detection of less molecular bonds in the focal volume. As well as providing a significant enhancement to the CARS signal, gold NRs behave as sub-diffraction limited volumes, enabling the detection of objects in their vicinity that are smaller than the wavelength of light. Enhancement to the eHCARS signal from silicone oil in the vicinity of bare gold NRs (bNRs), silica coated NRs (sNRs) and nanorod dimers of various size was measured. bNRs providing a good signal enhancement of up x10 more signal at the bNR compared to the surrounding silicone oil. However, bNRs were observed to be unstable during laser exposures undergoing significant signal variation during the measurement timescale. Concluding that the instability was a result of the bNRs being reshaped by the laser, sNRs were chosen as it was believed that the silica shell would constrain the shape of the NR. sNRs provided around x15 more signal in their vicinity compared to the surrounding silicone oil, and were seemingly stable during the duration of the measurements. Enhancement to the eHCARS signal in the vicinity of gold nanorod dimers, fabricated by focused ion beam lithography, (FIB) of various length was

measured, with up to a x100 enhancement measured for a dimer where the antenna, and bonding modes align with the CARS, pump and Stokes wavelengths.

Acknowledgements

I'd like to extend my deepest gratitude to Prof Paola Borri and Prof Wolfgang Langbein for their close mentoring, and invaluable supervision during my time at Cardiff University. I feel extremely privileged to have spent time working within the Quantum Optoelectronics and Biophotonics group.

I would also like to thank Dr Lukas Payne and Dr Iestyn Pope, for answering countless questions and assisting with my training. I'm very grateful to Martina Recchia for her assistance with sample preparation and assistance with the experiments.

Lastly I'd like to thank my wife to be Jasmine for supporting me throughout this process.

Chapter 1

Introduction

In the past four centuries scientists have been deeply invested in developing optical tools for resolving the microscopic world in more detail. Ironically, the invention of the optical microscope in the early 17th century itself is unclear, with disputed origins between the Dutch family of spectacle makers, the Janssen's, and Cornelis Drebbel. With an added dispute that Galileo himself might have been the founder, directing an elongated telescope downwards towards smaller structures instead of upwards towards the stars [5, 6]. The founders may have thought that microscopes were a novelty at first, a scientific toy, with no accounts of significant discoveries or work involving microscopes for some years to follow. The first significant work involving the optical microscopes, in this case a microscope built by Galileo, were Cesi and Selluti's illustrations of insects in the book *Apiarium*. It was again some years to follow before any other work was published, possibly due to the difficulties at the time in lens making, accounted by Galileo in a letter to Cesi in 1924 [7, 8]. Hooke would later, in 1665, utilise his own water-lens microscope to discover the small units of life, he called 'cells' [9], made possible by the introduction of an illumination source in his microscope. However, even though he wasn't the first to observe organisms with a microscope, Antonie van Leeuwenhoek, is often said to be the father of microbiology, and the first true microscopist. He observed microorganisms, in 1675, for the first time, which he named 'animalcules', utilising his pioneering craft for lens design and manufacture; his small bi-convex lenses allowed him to magnify up to $\times 250$, and avoided the common issues of aberration in compound microscopes at the time [10, 11]. The ingenious, basic, technology of the optical microscope has been used for hundreds of years, finding a use case in most scientific fields; from drug discovery to microchip design.

There have been many techniques based on the conventional light microscope improving image contrast. Phase contrast microscopy by Zernike [12] and differential interference contrast (DIC) microscopy by Nomarski [13], both utilise the optical path difference to create contrast in objects that would otherwise be transparent in transmission. Light microscopy techniques are limited in resolution by the diffraction limit. Described by Abbe [14], the smallest resolvable length, d, is limited by the wavelength (λ) and numerical aperture of the lens (NA) as follows,

$$d = \frac{\lambda}{2NA} \tag{1.1}$$

This means that the resolution of optical light microscopy is limited to a few hundred nanometers in the visible part of the electromagnetic spectrum. Also to be

considered is the Rayleigh criterion, Eq. 1.2 for a diffraction pattern for a circular aperture, where it states that the smallest possible resolvable angle between two point sources is θ, D is a circular aperture diameter.

$$\theta = \frac{1.22\lambda}{D} \tag{1.2}$$

Meaning that two point sources can only be resolved if they are angularly separated by angles $> \theta$, or when the centre of the diffraction pattern of one source is overlapping the first minimum of the diffraction pattern of another source [15].

One of the first techniques that would push the detection of nano-objects beyond the diffraction limit was Zsigmondy's Nobel prize winning work on the ultramicroscope [16]. The detection of the scattered light from Virginia, USA colloid nanoparticles in this case is perpendicular to the excitation direction, with Zsigmondy being able to detect particles as small as 4 nm. In this case the technique resulted in diffraction limited spots in the image, then from their scattered light and movement Zsigmondy was able to calculate their size. Moving beyond the optical microscope in the detection of nano-objects was the first scanning electron microscope (SEM) [17], where beams of electrons are used to scan structures and subsequently the scanning probe microscope (SPM) [18], achieving an atomic resolution, which is a true spatial resolution improvement since these techniques do not use light. More recently within light microscopy, cutting edge scanning near-field techniques utilising an enhancement from the scanning tip, detecting a Raman spectrum during the scan have recently been successful in providing nanometer resolution spectroscopic imaging of 2D surfaces [19, 20, 21]. The near-field scanning techniques provide chemists with an excellent tool for studying chemical mechanisms and interactions. However, for a biological use case, the super resolution scanning techniques are restricted to imaging very small regions of a fixed 2D surface, and take a long time to do so. The requirement for fixed sample sites makes them unsuitable for most biosensing applications of non-fixed molecules.

Typically biologists turn to fluorescence microscopy, providing excellent specificity of labelled structures, with contrast only from objects that fluoresce [22, 23]. Nanometer resolution is possible by single-molecule localisation fluorescence (e.g PALM) [24]. To achieve such resolution in PALM, it's crucial to utilise fluorophores that have a switching behaviour with a large contrast between on and off states (e.g photo-activated green fluorescent proteins). Due to the Nyquist criterion, it is also necessary to use extremely high density of labels, which can cause over expression, where tagged protein are modified. Staining procedures in general introduce an outside influence that can cause organelles and membranes to undergo structural or functional changes.

The caveat that holds for any super-resolution techniques based on single-molecule localisation is that, to achieve high resolution (beyond the diffraction limit) it is necessary to take many repeated measurements with single fluorophores being on and off at different spatial positions, typically using higher power illumination fields. When applied to biological samples, this means that with long experiment durations it is impossible to image something living, that is moving faster than the timescale of the measurement, and the high illumination/excitation powers inflict photo-damage

or changes during the course of the measurement.

Multi-photon scanning microscopy, where nonlinear signal is generated only in the focal volume where high photon densities are reached, has provided biologists with an excellent tool providing more 3D resolution and contrast compared to wide-field optical techniques [25, 26]. Fluorescence techniques lack in molecular specificity without tagging, providing no further information other than the positional or 'on-off' state of the fluorophore. Furthermore, microscopy techniques based on the Raman effect were explored, as the retrievable spectral information provided information unavailable in fluorescence [27]. Coherent Raman Scattering (CRS), a non-linear multi-photon confocal vibrational microscopy technique, has shown great promise over the last few decades to be the foundations of a high speed, resolution and label-free chemically specific imaging technique [28, 29]. Unlike fluorescence there is no need to tag specific molecules, as a unique signal is generated from each different bond type by the Raman process [30]. CRS techniques, such as coherent anti-stokes Raman scattering (CARS) [31, 32, 33, 34] and stimulated Raman scattering (SRS) [35, 36] have been extensively used in lipid biology for a number of different applications. CRS techniques allow for chemically specific detection of cellular and sub-cellular environments, generating hyperspectral images where individual components can be isolated [37, 38, 39]. CRS techniques are well suited to lipid biology, taking advantage of the large number of CH bonds in lipid acyl chains to generate signal.

In spontaneous Raman scattering, the detected signal is an incoherent superposition of fields generated by the number (N) of oscillators (molecules) in the focal volume. The Raman intensity is proportional to N in the focal volume and the incident field intensity (I_{i}) as follows,

$$I_{\mathrm{R}} \propto N \times I_{\mathrm{i}} \tag{1.3}$$

and provides a weak signal (owing to the small Raman scattering cross-section of bio-molecules) containing a significant autofluorescence background, not suitable for high resolution or sensitivity. However, by exciting the molecular bonds with short high power laser pulses it is possible to coherently enhance the Raman scattering, done so by interfering two optical fields (pump and Stokes, with intensity $\mathrm{I_P}$ and $\mathrm{I_S}$) to generate a beating frequency matching the resonance of the molecular vibrations, that efficiently drives the oscillations. On a molecular level the electron cloud is then oscillating at the difference in pump and Stokes frequencies, altering the optical properties of the material. There is a periodic modulation of the polarisability, that can then be probed by a secondary incident field, (in our setup we use the pump again as our probe), which will be modified to give us the CARS emission. Here the scattered light constructively interferes as there is a constant phase relationship between the N oscillators, vibrating in synchronisation. The CARS intensity is quadratically dependent of the number of oscillators in the focal volume,

$$I_{\mathrm{CARS}} \propto N^2 I_{\mathrm{P}}^2 I_{\mathrm{S}} \tag{1.4}$$

allowing for higher sensitivity than spontaneous Raman and video rate acquisition times. Detecting at the CARS optical frequency, given by

$$\omega_{\mathrm{CARS}} = 2\omega_{\mathrm{P}} - \omega_{\mathrm{S}} \tag{1.5}$$

with ω_P and ω_S being the optical frequencies of the pump and Stokes fields respectively. The signal here is free from excitation background, as ω_{CARS} is well separated from the excitation fields. CARS microscopes have developed significantly since the first spatially scanning CARS microscope built in 1981, by Dr Michael Duncan [40]. Unfortunately, as I_{CARS} is typically detected, which is proportional to the modulo square of the field E_{CARS} and in turn of the non-linear susceptibility (χ^3), there is a considerable background signal in conventional CARS microscopy. Originating from the interference of the resonant and non-resonant parts of the χ^3 is an asymmetric spectral lineshape of the resonant response, as well as a non-resonant background contribution [41].

Another way of implementing CRS is to detect the signal at either the frequency of the pump or Stokes excitation fields. This technique is called stimulated Raman scattering (SRS), and it is a type of interferometric homodyning CRS technique. In SRS the phase of the CRS signal is matched with the excitation fields providing an amplitude and phase change to the excitation frequency detected. The amplitude change is proportional the the imaginary part of the χ^3 whilst the phase change is proportional to the real part of χ^3. SRS detection is implemented by modulating one of either the pump or Stokes beams and then detecting at the others frequency using a lock-in detection. Detection in this way is necessary due to the excitation field amplitude being much larger than the CRS signal amplitudes. SRS allows for the non-resonant background to be separated as truly only the resonant part of the susceptibility response is detected as an amplitude change of the incoming fields. However, in SRS there are other contributions to the background signal with non-linear origins. There is a nonlinear absorption arising from the sequential absorption of pump and probe photons, which has an amplitude variation similar to the SRS signal [42]. There is also nonlinear scattering which arises from a refractive index change induced by one of the excitation fields and felt by the other. This cross-phase modulation modifies the angular distribution of beams, causing an intensity variation in the detection [43, 44]. Photothermal effects, such as, thermal lensing can occur causing an intensity variation [45, 46]. The detection of SRS is free from nonlinear background contributions [47], by exploiting the fact that the nonlinear artefacts in SRS are symmetric under a sign change in the pump-probe frequency difference, whereas the SRS signal is antisymmetric. When choosing whether to use SRS of CARS the user must consider the fact that CARS is detected at a new frequency but contains a non-resonant background and SRS is background free but is detected by homodyning an excitation frequency. Therefore one might select SRS where a more sensitive sensing is required (lower concentration of molecules) but use CARS when there is an abundance of signal for the ease of implementation.

There have been many methods developed that compensate for the non-resonant background in CARS. One of these, is to detect the CARS intensity over a large spectral range, hyperspectral CARS [38, 48, 49], to retrieve the phase of the non-linear susceptibility, using appropriate spectral transformations linking the detected amplitude with it's phase. Requiring a CARS measurement to be performed at each frequency, it is not suited for video rate imaging. Hyperspectral CARS is an extremely useful tool when wanting to identify specific molecular components in a fixed cellular environment [50] but limited by imaging time. Frequency modulated CARS (FM-CARS), where the frequency of the pump and Stokes beams are mod-

ulated, and then the modulated CARS signal detected in a lock-in amplifier, has been shown to suppress the non-resonant background whilst maintaining video rate imaging [51]. Elliptically polarised CARS has also been shown to suppress the non-resonant background, with a $\sim \times 6$ improvement to the signal to noise ratio [52] done so by detecting the cross-polarisation component, assuming that the isotropic non-resonant background has a specific co-polarisation direction. It is also possible to separate the instantaneous non-resonant background from the resonant signal by time gating [53, 54]. A novel way of detecting the CARS intensity is by measuring two vibrational frequencies simultaneously. In this method, called Dual CAlRS (D-CARS), the differential CARS signal can be detected free from non-resonant background. D-CARS has been implemented utilising femto-second laser pulses, and spectral focussing (using the dispersion from glass blocks) [55], to excite a pair of CARS vibrations alternatively within the pulse train sequence, such that the signal from both vibrations are detected simultaneously. The differential CARS signals are extracted with lock-in detection [38, 56, 57, 58]. SRS, D-CARS, and FMCARS both offer a non-resonant background free CRS technique, capable of video rate acquisition speeds.

Typically, CARS is detected in the forward direction (FCARS), where the detection is made in the same direction as the excitation. The radiation pattern of CARS signal is dependent on the size of the scatterer, in the incident propagation direction (axial dimension). When the axial diameter of the scatterer is larger than or equal to the excitation wavelength the CARS signal is confined to the forward detection. Whereas, for an object much smaller than the wavelength, the CARS emission is symmetrically forwards and backwards emitted [59, 60]. FCARS is therefore limited by the CARS radiation pattern caused by its axial point spread function (psf) (which extends approximately $1\,\mu$m) and the bulk nonresonant background to detecting objects that are close to the diffraction limit Eq. 1.1 in size. However, in epi-detection (backwards towards the excitation direction) it's possible to resolve objects that are much smaller than the excitation wavelength, due to their symmetric emission, separated from the forward-emitted bulk nonresonant background. Epi-CARS provides an excellent tool for chemically specific imaging of objects, thin layers such as lipid bilayers, and interfaces that are smaller than the PSF [61, 62, 63].

The latest reported revision of an interferometric CRS technique by Langbein *et al* [64, 65], used and characterised in this thesis, is a dual-polarisation heterodyne detection epi-CARS technique (eHCARS), with balanced photodiode detection. By temporally and spatially overlapping the epi-CARS field with a reference beam, that does not pass through the sample, and detecting the interference by balanced photodiode detection the amplitude and phase of the CARS signal is obtained. Previously reported interferometric techniques utilised a reference beam at the sample overlapped with both pump and Stokes beams, detecting the field amplitude by homodyne detection (no frequency shift [66], and the first HCARS reported by Jurna *et al* [67]. In these cases having the reference at the sample means that there is no balanced detection to suppress classical noise, and there is more risk of sample photo damage by the reference beam. In the case of the heterodyne-CARS technique explored in this thesis, the reference interferes with the CARS signal outside the sample, and is detected by a balanced photodiode detector, leading to a suppression of the non-resonant, and incoherent background without additional risk of

photodamage. Furthermore, the reference power can be chosen to be dominant, such that the signal is shot-noise limited. As the full CARS field information is detected the amplitude and phase of the signal allows for not only distinguishing between resonant and non-resonant responses, but also provides topographical information. For small objects, such as thin layers, interfaces, and nanoparticles that are much smaller than the axial psf, the epi-detected signal is resulting from the χ^3 of a single sub-diffraction limit object. This means that the phase of the epi-detected signal can provide information regarding the axial position and height differences with nanometer precision [64, 68].

In the eHCARS technique discussed, the technical realisations of heterodyne interferometric detection suppresses any incoherent contribution, owing to it's interferometric nature (only the coherent CARS field interferes with a phase-locked reference). Moreover, epi-detection provides topographical information as well as signal from sub-diffraction limited scatterers by removing the bulk background. Therefore in itself eHCARS is a promising new technique for label-free, chemically specific, imaging of interfaces. However, it must be noted that the vibrational contrast is intrinsically much less than what is typically achieved in fluorescence. Single molecule detection is possible in fluorescence [24, 69], whilst in conventional CRS, sensitivity has only been demonstrated down to $\sim$ 100 oscillators so far, using specially tailored Raman tags (while with endogenous biomolecules, the sensitivity limit is typically 10^4-10^5 vibrations in the focal volume) [70]. To achieve single molecule sensitivity utilising a vibrational microscopy technique, the local field enhancement of plasmonic materials has to be exploited. Single molecule detection has been demonstrated in surface enhanced Raman scattering (SERS) [71, 72, 73] and in surface enhance CARS (SECARS) [74, 75, 76]. By driving the local surface plasmon resonance (LSPR) on a metallic nanoparticle (NP) at the CARS frequency a confined enhanced field is generated in it's vicinity. Meaning that biomolecules in the close vicinity of the plasmonic NP will contribute to the enhanced field. The near-field spatial distribution around the plasmonic NP's does not follow the diffraction limit Eq. 1.1, therefore sub-diffraction limited volumes generating signal within the enhancement region can be detected. NP's providing local field enhancement (LFE) to the eHCARS signal, will mean that the number of bonds required in the focal volume to generate a detectable signal is lower, and will provide a sub-diffraction limited volume allowing nanoscale sensing. In SE-eHCARS the detected signal variations are directly coupled to contributing factors to the signal at the nanoscale region near the plasmonic nanoparticle, therefore nanoscale objects that enter this region will provide detectable signal changes that aren't diffraction limited; but are limited to the size of the nanoparticle. Implementing SE-eHCARS should address the two major downfalls of CRS, the requirement of a large number of oscillators in the focal volume to generate a detectable signal, and the diffraction limit of the PSF. Once implemented, SE-eHCARS will provide a low-concentration background free, chemically specific, label-free, and topographically sensitive vibrational imaging technique, capable of fast acquisition times (video rate) at laser intensities suitable for biological imaging. Surface enhanced vibrational microscopy techniques could be referred to as a label-free technique only if the nanoparticles aren't placed internally within the biological environment, so that's only when the material of interest is placed on top or near the nanoparticles. Once the nanoparticles are placed within the biological environment the technique can no longer be considered label free as

the environment is perturbed or modified by the gold nanoparticles presence. Even placing the gold nanoparticles in the vicinity of the bio-environment there should be consideration for any influence.

The scope of this thesis is to explore the eHCARS technique in the vicinity of plasmonic nanoparticles, using a model system, to characterise and understand the generated signals. The ultimate, ambitious, goal beyond this thesis is to utilise SE-eHCARS to image biological systems such as lipid nanodomains and to detect lipid rafts. The existence of lipid rafts is still debated by scientists, partly due to the lacking of a tool capable of imaging such an object at video rates [77, 78]. The CRS techniques that precede SE-eHCARS lack the nanoscale sensing and low molecular concentration sensitivity to directly image lipid rafts in lipid bilayer systems. Due to the nanoscale sensing advantage gained by utilising plasmonic nanoparticles in the vicinity, one could place a lipid bilayer on top of a gold nanoparticle and sense the eHCARS signal from the bilayer at the nanorod achieveing enhanced nanoscale detection. The sensing of biological environments was not achieved during this thesis as much difficulty was met when attempting to do eHCARS in the vicinity of gold nanoparticles; due to gold nanoparticle heating and reshaping. The focus of this thesis was driven towards characterisation of eHCARS and ensuring that a stable SE-eHCARS signal in the vicinity of gold nanoparticles was achieved.

Chapter 2

Theoretical Background

2.1 Non-linear vibrational microscopy

The motivations for exploring a vibrational microscopy technique stems from the drawbacks associated with typical fluorescence and other widefield microscopy techniques that rely on optical path length difference to obtain contrast. Fluorescence in itself is a very powerful technique, with well established use cases for biological imaging applications. The issue with fluorescence microscopy is that to obtain a signal, the object of interest must either itself be capable of fluorescing under photoexcitation or one has to tag the objects of interest with fluorescent probes. There is a risk when introducing probes that tagged biological elements, such as proteins, can be modified or over expressed within the environment. Stained organelles and membranes can undergo structural and functional changes. Alternative imaging techniques such as phase-contrast or differential interference contrast microscopy don't require the user to label the objects of interest. Contrast is obtained by the techniques sensitivity to optical path differences. In this case the identification of specific objects within the image relies on the user doing so in the analysis based on the shape and thickness of objects observed, given the context of the experiment. Vibrational microscopy, specifically Raman based, techniques provide a label free and chemically specific option. Coherent Raman scattering provides a nonlinear vibrational microscopy modality which will be exploited in this thesis.

A very simple way of introducing the nonlinear regime is to envisage a hydrogen atom interacting with an E-field Fig. 2.1. The hydrogen atom is represented by a positive charge surrounded by a cloud of negative charges, Fig. 2.1(1.). In the presence of an E-field the negative charge cloud is distorted Fig. 2.1(2.), the distorted atom can then be represented as a dipole Fig. 2.1(3.), with dipole moment,

$$\mu(t) = -er(t) \tag{2.1}$$

For small displacements, $r(t)$, there is a harmonic binding potential where the force applied by the E-field causes a linear change in the displacement. The induced polarisation, $P(t)$, is given by the N number of electric dipole moments per unit volume.

$$P(t) = N\mu(t) \tag{2.2}$$

The susceptibility, χ, in the weak field, $E(t)$, limit, which describes the degree of induced polarisation in response to $E(t)$, is related by

$$P(t) = \epsilon_0 \chi E(t) \tag{2.3}$$

When the E-field is removed, the distorted cloud returns to its original state [79]. Eq. 2.3 shows that P depends linearly on an applied $E(t)$. If the $E(t)$ is oscillating over time, it's expected that the displacement of charges will follow the same oscillation in a linear fashion.

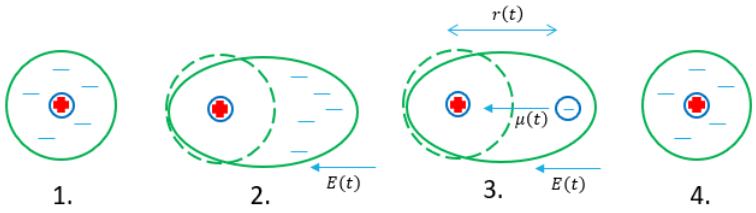

Figure 2.1: Hydrogen atom in the presence of an E-field. 1.) H-Atom in the ground state, represented by a single positive charge surrounded by a cloud of negative charges. 2.) In the presence of an E-field, $E(t)$, the charge cloud becomes distorted, negative charges moving away from the direction of the $E(t)$. 3.) Representing the distorted atom as a dipole with a positive and negative point charge, dipole moment $\mu(t)$. 4.) Removal of the E-field resulting in the atom returning to its ground state.

From Eq. 2.3 we see that greater $E(t)$ field strengths on the hydrogen atom model results in a larger displacement of charges. For large $E(t)$ we can no longer assume the electron binding potential to be harmonic and must consider the fact that there are anharmonic effects at play; such that $P(t)$ is no longer linear dependent on $E(t)$. If we assume that the anharmonic contributions are small, it's possible to express the induced polarisation as a taylor series,

$$P(t) = \epsilon_0[\chi^{(1)}E(t) + \chi^{(2)}E^2(t) + \chi^{(3)}E^3(t) + ... + \chi^{(n)}E^n(t)] \tag{2.4}$$

with n^{th} order nonlinear contributions. The first order, n= 1, is the linear regime, the second order is n= 2 and so on.

In nonlinear microscopy typically ultrafast laser pulses in the pico to femto second range are used to induce nonlinear optical effects that are related to the electronic polarisability of the material, owing to the high peak fields of short pulses, while time-averahe powers can be kept to a moderate level (dependent on the pulse repetition rate).

2.1.1 Raman scattering principles

2.1.1.1 Spontaneous Raman Scattering

When light interacts with a molecule, the incident light is either absorbed or scattered. The phenomenon called Raman scattering, first observed by Raman in 1928 [30], occurs when light is scattered inelastically. The majority of light is scattered elastically by Rayleigh scattering, but there is a small portion of the scattered light that is shifted in energy, either gaining or loosing energy inelastically. The Raman scattered light that looses energy is called the Stokes and the scattered light that gains energy is called the anti-Stokes. In Fig. 2.2, the incident and Rayleigh scattered light are shown in green, the Stokes in red and the anti-Stokes in blue.

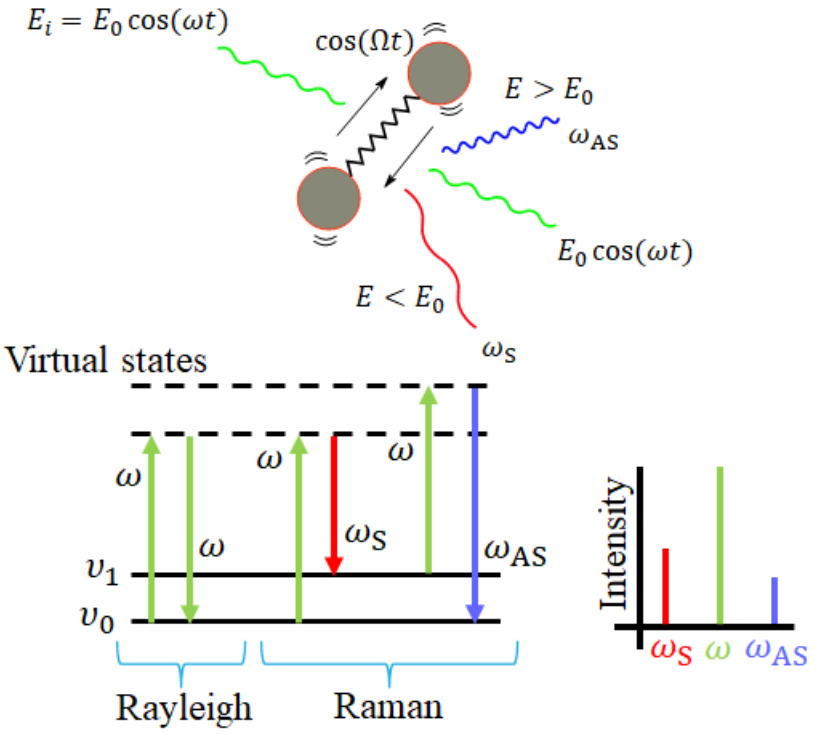

Figure 2.2: Spontaneous raman

Consider a diatomic molecule, as shown in Fig. 2.2, with incident light, $E(t)$, oscillating at the optical frequency ω. The incident light field induces a dipole moment in the molecule, $p(t)$, given by

$$p(t) = \epsilon_0 \alpha(t) E(t) \tag{2.5}$$

The molecular bond's displacement oscillates sinusoidally by

$$x(t) = A\cos(\Omega t) \tag{2.6}$$

where Ω is the frequency of the oscillation and A is the amplitude. In this case as the displacements are very small, the polarisability, $\alpha(t)$, can be described by a Taylor expansion at a small perturbation from its equilibrium position.

$$\alpha(t) = \alpha_0 + \left(\frac{\partial \alpha}{\partial x}\right)_0 x(t) \tag{2.7}$$

Using the expression for the linear function of displacements, the dipole moment Eq. 2.5 becomes,

$$p(t) = \epsilon_0 E_0 \cos(\omega t)\left[\alpha_0 + \left(\frac{\partial \alpha}{\partial x}\right)_0 A\cos(\Omega t)\right] \tag{2.8}$$

which contains Rayleigh and Raman components and can be expanded to give [80],

$$\text{Rayleigh} = \epsilon_0 \alpha_0 E_0 \cos(\omega t) \tag{2.9}$$

$$\text{Stokes Raman} = \frac{\epsilon_0 (\partial\alpha/\partial x)_0 E_0}{2} A\cos\left(\omega t - \Omega t\right) \tag{2.10}$$

$$\text{anti-Stokes Raman} = \frac{\epsilon_0(\partial\alpha/\partial x)_0 E_0}{2} A\cos(\omega t + \Omega t) \tag{2.11}$$

where $(\omega t - \Omega t) = \omega_{\mathrm{S}}$ and $(\omega t + \Omega t) = \omega_{\mathrm{AS}}$. As shown in Fig. 2.2, the ω_{S} is red shifted and ω_{AS} is blue shifted compared to the Rayleigh frequency ω by the resonant frequency Ω of the vibrational resonance.

2.1.1.2 Coherent Anti-Stokes Raman Scattering

The spontaneous Raman scattered light intensity, I_{R}, depends on the incoherent superposition of fields generated by the N oscillators in the focal volume oscillating due to an incident field intensity I_{i}

$$I_{\mathrm{R}} \propto N I_{\mathrm{i}} \tag{2.12}$$

The typically small Raman scattering cross sections of biomolecules result in a weak signal strength, not suitable for detecting small concentrations of molecular bonds. It's possible to enhance the Raman scattered light by interfering two optical fields, of pump ω_{p} and Stokes ω_{s} frequencies, to coherently excite the molecular resonances at their frequency difference, Ω, where

$$\Omega = \omega_{\mathrm{p}} - \omega_{\mathrm{s}} \tag{2.13}$$

The beating frequency Ω is sufficient to drive large molecular vibration amplitudes inducing molecular specific nonlinear polarisations when Ω approaches the resonance of the specific molecule. It can be shown that an induced dipole in the presence of an external field undergoes a force proportional to the field squared. Therefore the driving force, generated by the interference of the ω_{p} and ω_{s} field is proportional to

$$E_{\mathrm{A}}^2(z,t) = A_{\mathrm{p}} A_{\mathrm{s}}^* e^{i(Kz - \Omega t)} \tag{2.14}$$

where $K = k_{\mathrm{p}} - k_{\mathrm{s}}$, $k = 2\pi/\lambda$ being the wavevector of light and z is the thickness of the sample,and the resonant condition in Eq. 2.13 is satisfied [79].

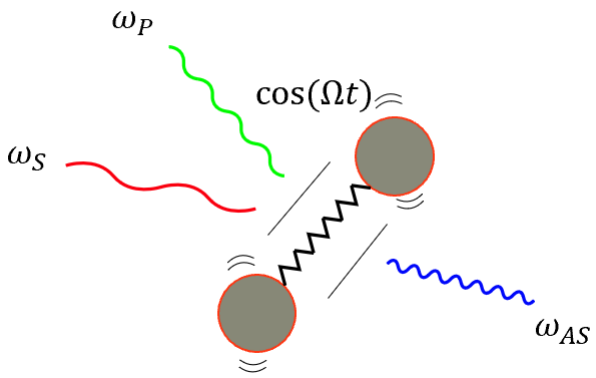

Figure 2.3: Coherent Raman Scattering

The induced non-linear polarisation of N resonant oscillators, $P = Np(z,t)$, driven by E_{i} results in 4 different scattering components [80].

$$\text{Coherent Stokes: } P(\omega_{\mathrm{cs}}) \propto x^*(\Omega) A_{\mathrm{s}} e^{i(2k_{\mathrm{s}}z - k_{\mathrm{p}}z)} \tag{2.15}$$

$$\text{Coherent Anti-Stokes: } P(\omega_{\text{as}}) \propto x(\Omega) A_{\text{p}} e^{i(2k_{\text{p}}z - k_{\text{s}}z)} \tag{2.16}$$

$$\text{Stimulated Raman gain: } P(\omega_{\text{s}}) \propto x^*(\Omega) A_{\text{p}} e^{ik_{\text{s}}z} \tag{2.17}$$

$$\text{Stimulated Raman loss: } P(\omega_{\text{p}}) \propto x(\Omega) A_{\text{s}} e^{ik_{\text{p}}z} \tag{2.18}$$

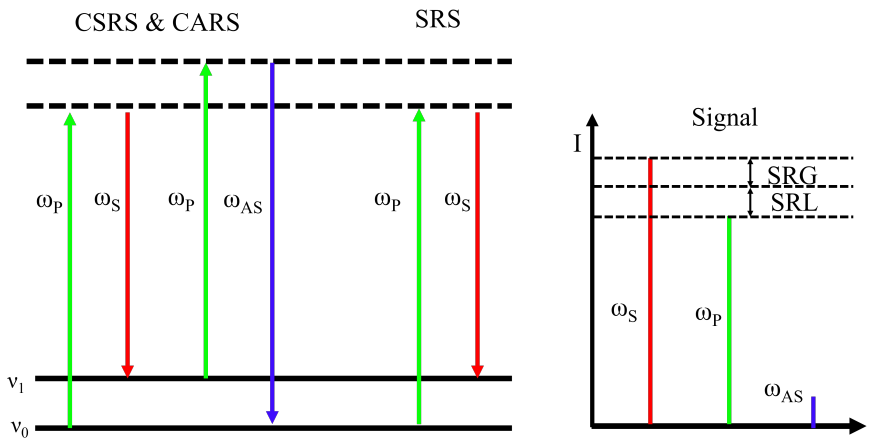

Figure 2.4: Left: Coherent Stokes Raman scattering (CSRS), CARS and SRS vibrational processes. Right: Output spectra of the CRS process, where either a gain to ω_S, loss in ω_P, or ω_{AS} is detected.

The CARS intensity is given by

$$I_{\text{CARS}} \propto N^2 \left|\chi^{(3)}\right|^2 I_{\text{p}}^2 I_{\text{s}} \left|\frac{\sin(\Delta k z/2)}{\Delta k/2}\right|^2 \tag{2.19}$$

where $\Delta k = k_{\text{as}} - (2k_{\text{p}} - k_{\text{s}})$. When $\Delta k z$ approaches zero, the phase matched condition is reached [81]. For CARS processes we see that the intensity is proportional to $N^2 I_{\text{p}}^2 I_{\text{s}}$, and providing a signal enhancement [79]. The increased signal is due to the constructive interference of scattered fields that are being coherently driven.

When detecting CARS, not only is there a contribution from non-resonant processes unrelated to Raman, such as fluorescence, there is also a non-resonant CARS and four wave mixing CARS background present [80, 81].

$$I_{\text{CARS}} \propto \left|\chi_{\text{nr}}^{(3)}\right|^2 + \left|\chi_{\text{r}}^{(3)}\right|^2 + 2\chi_{\text{nr}}^{(3)} \Re\left\{\chi_{\text{r}}^{(3)}\right\} \tag{2.20}$$

As shown in Eq. 2.20 there are three contributions to I_{CARS}, a strong resonant contribution, followed by a weaker non-resonant background and a term including both a resonant and non-resonant contribution. The resonant and non-resonant CARS contributions are shown in Fig. 2.5.

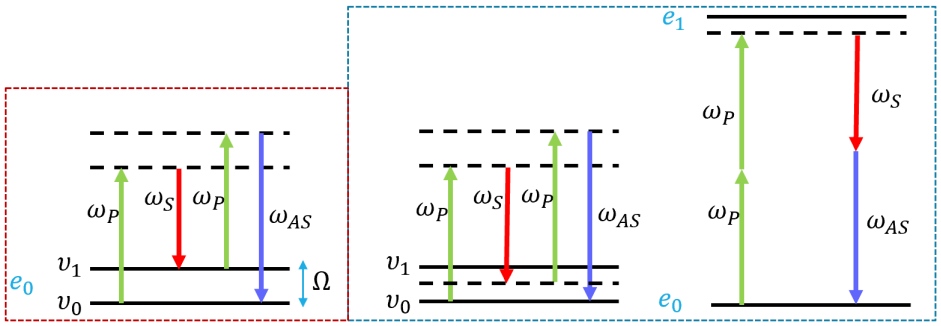

Figure 2.5: Red box: Resonant CARS process. Blue box: Left shows CARS Non-resonant background and right is a non-resonant contributions including a four-wave mixing term enhanced by two-photon electronic transitions.

The mixing of resonant and non-resonant CARS is sufficient such that in the detection of I_{CARS} the maximum intensity of the signal is shifted to lower wavenumbers compared to the resonance. As well as being shifted, the I_{CARS} peak has an asymmetric shape due to the mixing non-resonant background term [80]. Stimulated Raman loss (SRL) and Stimulated Raman gain (SRG), are both stimulated raman scattering (SRS) processes, and are coherent. SRS can be detected as a reduction or gain in the ω_{s} or ω_{p} excitation field intensity by modulating the opposite excitation frequency. SRS is a homodyne interferometric technique and is free from non-resonant background.

2.2 Metallic nanoparticles

2.2.1 LSPR

The optical properties of metallic nanoparticles (NP's) are considerably different from their bulk metal counterparts. The collective motion of free electrons driven by an excitation field is known as localised surface plasmon resonance (LSPR)[82]. Plasmons are considered to be bosonic quasi particles, a cloud of electrons that are displaced around a lattice of positive charges [83]. When a metallic object is smaller than the wavelength of light, such as for NP's, the incident E-field can penetrate the surface and manipulate the surface conduction electrons, polarising the electron cloud within the confines of the objects shape. The polarisation of the electron cloud results in a dipole-like interaction with the confined positive lattice charges. The coulomb interaction between the distorted cloud and lattice charges acts as a restoring force to the polarisation. The excitation field and coulomb restorative force then behave like a damped oscillator. The positive lattice charges act to restore the polarised electron cloud back to it's equilibrium position. A metallic material such as gold is well fitted for plasmonic resonance applications. The collective motion of free conduction electrons, that do not interact with each other, around fixed nuclei is described in the Drude model for such materials. There is no interaction between free electrons, however, they do elastically collide with the stationary nuclei.

To arrive at the Drude model, one can begin with deriving the Lorentz model of optical polarizability. The Lorentz model [84] considers a system where electrons

orbit a fixed nucleus and are described by a series of classical damped harmonic oscillators that are driven by an E-field, $\mathbf{E}$. The force F from $\mathbf{E}$ on a charge, e, is

$$F = -e\mathbf{E} \tag{2.21}$$

The oscillating E-field drives an oscillation with a damping coefficient, γ, and natural frequency ω_0. The force, F, as a function of the electrons displacement from equilibrium, $\mathbf{r}$, over time can be written as

$$F = m\left(\frac{d^2\mathbf{r}}{dt^2} + \gamma\frac{d\mathbf{r}}{dt} + \omega_0^2\mathbf{r}\right) \tag{2.22}$$

Using complex notation to represent both the displacement $\mathbf{r} = \mathbf{r}_0 e^{-i\omega t}$ and field $\mathbf{E} = \mathbf{E}_0 e^{-i\omega t}$ a solution for the above equation of motion can be obtained

$$\mathbf{r} = \frac{-e\mathbf{E}}{m^*\left(\omega_0^2 - \omega^2 - i\gamma\omega\right)} \tag{2.23}$$

where m^* is the effective electron mass. A single electron displacement of $\mathbf{r}$ results in an induced polarisation of

$$\mathbf{p} = \frac{e^2\mathbf{E}}{m^*\left(\omega_0^2 - \omega^2 - i\gamma\omega\right)} \tag{2.24}$$

From here an expression for the dielectric function can be obtained by substituting $\mathbf{p}$ into

$$\varepsilon\left(\omega\right) = 1 + \frac{\mathbf{p}}{\varepsilon_0\mathbf{E}} \tag{2.25}$$

making the assumption that all n oscillators do not interact we find that

$$\varepsilon\left(\omega\right) = 1 + \frac{ne^2}{\varepsilon_0 m^*\left(\omega_0^2 - \omega^2 - i\gamma\omega\right)} \tag{2.26}$$

The Drude model assumes no restorative force between free electrons, therefore within the Drude model Eq. 2.26 becomes

$$\varepsilon\left(\omega\right) = 1 - \frac{ne^2}{\varepsilon_0 m^*\left(\omega^2 + i\gamma\omega\right)} \tag{2.27}$$

when $\omega_0 = 0$. The material plasma frequency is given by

$$\omega_p = \sqrt{\frac{ne^2}{m^*\varepsilon_0}} \tag{2.28}$$

and represents the resonant frequency of the plasma oscillation.

LSPR result in a strong absorbance of light, which leads to emission of high coherent field strengths close to the NP's when utilised for SE-CARS [85]. Spherical NP's have one absorption, one LSPR, whereas nanorods (NR's) have two absorption bands, a sketch is shown in Fig. 2.6. The absorption bands in NR's correspond to the polarisation of free electrons along the length and width of the particle, named the longitudinal and transverse resonances. The extinction cross-section,

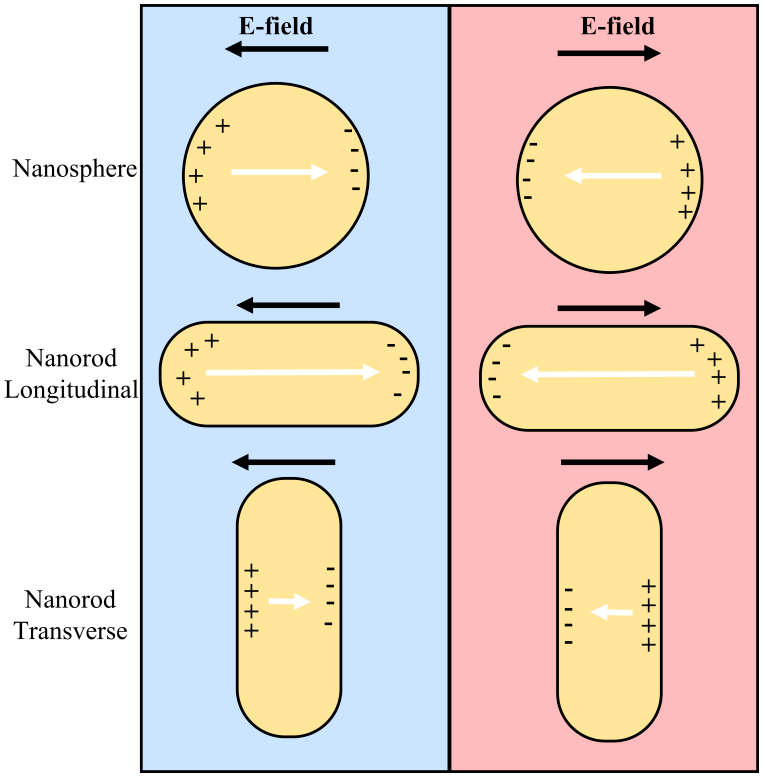

Figure 2.6: The top is a sketch of the induced polarisation in a nanoshpere. Below is the longitudinal and transverse induced polarisation in a nanorod. Two cases are shown,blue and red column, for an applied E-field phase shifted by π.

which describes the metallic NR's shape dependent interaction with light can be derived as

$$\sigma_{\text{ext,nr}} = \frac{2\pi V N \epsilon_{\text{m}}^{3/2}}{3\lambda} \sum_i \frac{(1/P_{\text{i}}^2)\epsilon_{\text{i}}}{(\epsilon_{\text{r}} + ((1-P_{\text{i}})/P_{\text{i}})\epsilon_{\text{m}})^2 + \epsilon_{\text{i}}^2} \tag{2.29}$$

according to Gans theory. Where the depolarisation factor, P_{i}, for NR's is given by [86],

$$P_{\text{L}} = \frac{1-e^2}{e^2}\left[\frac{1}{2e} ln\left(\frac{1+e}{1-e}\right) - 1\right] \tag{2.30}$$

$$P_{\text{T}} = \frac{1-P_{\text{L}}}{2} \tag{2.31}$$

where e is the ellipticity, related to the aspect ratio, a =length/width, as

$$e^2 = 1 - a^{-2} \tag{2.32}$$

From this point it is possible to see that any small variation of the NR's aspect ratio has a significant effect on the absorbance band, and consequently the LSPR. As well as a shape dependence, there is a shift in the LSPR dependent on the surrounding refractive index. This high tune-ability and sensitivity is one of the reasons gold NR's are of such interest in the bio-sensor industry [87] [88].

Laser induced gold nanoparticle reshaping has been suggested and used as a technique for fabricating specific shaped gold particles, with the pulse intensity and duration having an effect on the resulting shape of the nanoparticle [89, 90]. It has been shown that femtosecond laser pulses induce much more reshaping than

nanosecond pulses. In addition to controlled reshaping, the ultrafast heating and then heat transfer by phonon-coupling to the local environment can be used as a localised temperature controller, and can sometimes lead to localised boiling or scorching in vivo or solution [91, 92]. It has been shown that there is a reduction in the metallic nanoparticles plasmonic response once exceeding 770K [93]. For LSPR sensing applications it is important to mitigate reshaping effects and minimise the measurements influence the surrounding environment whilst maintaining high signal enhancement. The difficulty with stabilising a nanoparticle from photothermal effects in surface enhancement measurements is shielding the particles often leads to coating the particle with a different material, such as silica, or oxides of titanium and aluminium, introducing a new refractive index and increasing the distance between the nanoparticle and substrate, thus lowering the amount of signal enhancement [94].

Chapter 3

Materials and Methods

3.1 Sample Preparation

3.1.1 Glass preparation

High grade Menzel Gläser 24x24 mm cover glasses that are nominally 0.16-0.19 mm in thickness were used to suspend samples. Menzel Gläser coverslips were chosen for their surface uniformity and optical homogeneity. Typically, for optical measurements of bulk materials, micron-scale structures, and photoluminescence of objects that are suspended on cover glass, it is sufficient to simply scrub the glass surfaces with acetone. This is done by soaking a piece of lint-free optics paper with acetone and scrubbing the glass in a linear motion in one direction, until no debris can be detected by eye on the glass. In most cases the glassware is already polished and cleaned from factory and this is sufficient to remove a significant amount of the debris. However, when performing high sensitivity and resolution measurements of single nanostructures and interfaces, it is important that the glass surfaces the sample is suspended on is free from debris of the same order of the measurement resolution. In focus debris can sometimes present difficulties when trying to distinguish between metallic nanoparticles and nanoscale dielectric debris. Whilst the defocus aberration from large debris on the glass can cause distortion blur at the imaging plane of focus. Following an acetone scrub, a chemical glass cleaning protocol can be done to extensively clean the surfaces. Both a Piranha etch and a sonication of glass in hydrogen peroxide were tested for cleaning using the Teflon coverslip holder shown in Fig. 3.1. Glass cleanliness was determined by visual inspection in extinction with a 100x 1.45 NA objective to ensure there was no dielectric debris on the glass surface, a surface was deemed clean if there was one piece of dielectric debris every 10 μm. The surface uniformity of the coverslips was not directly characterised, as there are no features present in the eHCARS measurements from the glass interface it suggests one can assume that the surface roughness is less than the resolution limit of the technique.

Before proceeding with the cleaning procedures glass slides had to be cut by hand to size first. The sample stage on our inverted microscope receives a non-standard (50mmx25mm) size microscope slides. A diamond scribe lubricated with isopropanol and any suitable straight edge template was used to scribe a fault line in the glass slide. The fault line was then tapped gently from underneath, and broken by pushing up through the scribe line from underneath, rather than bending

from above. This technique resulted in the cleanest glass breakages, leaving minimal burrs. It's important to cut the glass before cleaning the glass and assembling the sample to minimise the risk of glass dust contamination.

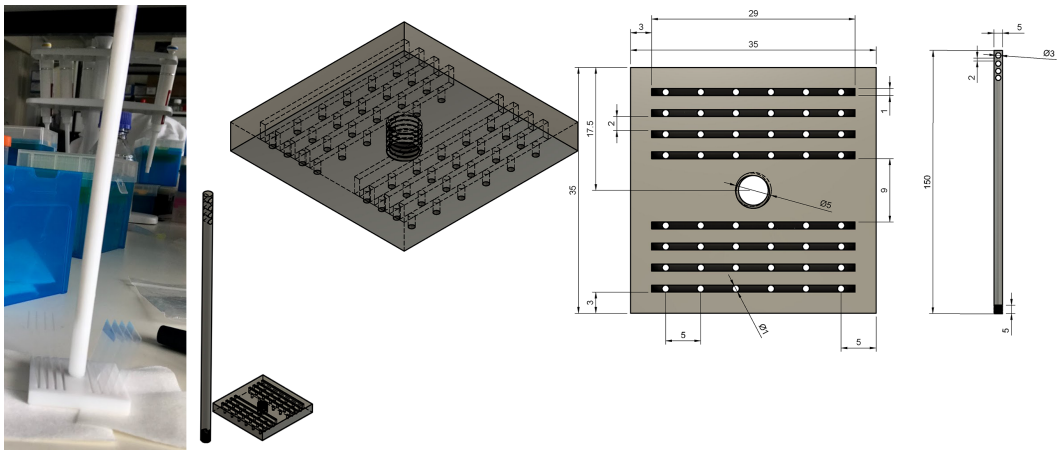

Figure 3.1: Left: Milled teflon coverslip holder with eight slots and a removable carrying rod. Right: Design with units given in mm.

3.1.1.1 Piranha solution

Acidic piranha solution is a mixture of hydrogen peroxide (H_2O_2) and sulphuric acid (H_2SO_4), Eq. 3.1. The solution reacts violently with any organic matter and has been used in various applications to treat and clean silica or quartz based surfaces; even to clean archaeological glass samples of soiled debris [95, 96]. When combining the solution there is hydration of H_2SO_4 producing Peroxymonosulfuric acid (Caro's acid) (H_2SO_5) which is an extremely corrosive and strong oxidiser (discovered by Heinrich Caro in the late 19th century [97]). Alongside the hydration reaction there is the dehydration of hydrogen peroxide producing both hydronium (H_3O^+) and bisulfate ions ($H_2SO_4{}^-$) along with an oxygen free radical ($O^\bullet$) Eq. 3.2 [98].

$$H_2SO_4 + H_2O_2 \longrightarrow H_2SO_5 + H_2O \tag{3.1}$$

$$H_2SO_4 + H_2O_2 \longrightarrow H_3O^+ + H_2SO_4{}^- + O^\bullet \tag{3.2}$$

The presence of $O^\bullet$ radicals, that have an unpaired valence electron, are what gives the solution the ability to completely carbonsise organic matter leaving only carbon dioxide (CO_2), water (H_2O), and oxygen (O_2). It is thought that $O^\bullet$ attacks the carbon linkages within organic materials to form carbonyl groups that subsequently react with a second $O^\bullet$ to form CO_2. Simultaneously to the dehydration by free radical attack is the hydration of sulphuric acid that removes H_2O, and the formation of O_2 by the joining of two $O^\bullet$. The resulting solution is therefore extremely dangerous to handle and can be explosive upon contact with specific solvents, such as acetone. In addition to cleaning, as piranha solution is a strong oxidiser it hydroxylates, Fig. 3.2, the surface of glass (SiO_2) by oxidising any molecule that is attached to the Silicon (Si). Hydroxylation provides the surface with possible binding sights for molecules of interest; one can therefore functionalise the surface with an intermediate molecule to then attach the structures of interest permanently to the glass [99, 100]. The presence of the acid in the piranha solution catalyses the reaction

given by Eq. 3.3 with the attachment of the hydroxyl group (−OH) occurring by the oxidisation steps from Eq. 3.4 to Eq. 3.5.

$$Si_2O + H_2O \rightleftharpoons 2\,SiOH \tag{3.3}$$

$$R{-}O{-}R + H^+ \longrightarrow R{-}OH^+{-}R \tag{3.4}$$

$$R{-}OH^+{-}R \longrightarrow R{-}OH + R^+ \tag{3.5}$$

$$R^+ + H_2O \longrightarrow HO{-}R + H^+ \tag{3.6}$$

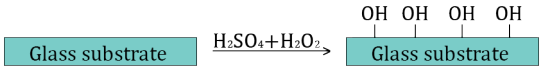

Figure 3.2: Sketch of the hydroxylation of a glass substrate.

For cleaning (etching) cover slips and slides the glassware was firstly scrubbed with acetone soaked lint free optics paper, rinsed thoroughly with Milli-Q deionised H_2O, and dried with nitrogen (N_2). The two 100 ml beakers, and measuring cylinders that would eventually contain both the H_2SO_4 and H_2O_2 separately were rinsed with concentrated H_2SO_4 to remove any contaminants. A 3:1 (volume:volume) ratio, 60 ml of concentrated H_2SO_4 to 20 ml of 30%wt H_2O_2 was measured and placed in the separate 100 ml beakers. The beaker containing the H_2SO_4 was then submerged in a water bath held at 95° C, and a stir bar was added.

Figure 3.3: Top:Water bath placed on a hotplate at 95° C, protected by a sheet of foil. Beakers containing water for the swirling rinse post etch; 600 ml, 150 ml, 100 ml. Two 100 ml beakers to receive the H_2O_2 and H_2SO_4. Two 600 ml waste beakers used to hold tweezers and for any piranha solution waste. 1 L beaker filler with tap water that can be used to dilute waste or spills. Bottom left: Water bath at 95° C with a 100 ml beaker containing 80 ml of piranha solution and eight Menzel Gläser 24x24 mm cover glasses held in place by a teflon coverslip holder (Fig. 3.1). Bottom right: Fume hood was closed and supervised during the etching process.

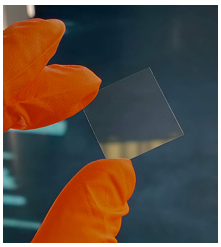

Figure 3.4: Coverslip after hydrogen peroxide cleaning method shown under room light.

Making sure that the stirring was sufficiently calm, the H_2O_2 could then be added slowly 5 ml at a time to the hot H_2SO_4. Once all the H_2O_2 had been added the dried glassware placed in the teflon coverslip holder, Fig. 3.1, could then be lowered into the piranha solution carefully. The glassware was left submerged for 30 mins under constant supervision. Once the duration had passed, the glassware was swirled gently in milli-q H_2O three times to remove the etching solution, dried (N_2), and stored under a N_2 atmosphere until required.

3.1.1.2 Hydrogen Peroxide

Since the process of cleaning glassware by piranha etching is fairly labour intensive and relatively dangerous, it was thought that similar results could be achieved by simply sonicating the glassware in sequential solvent baths and using H_2O_2 for the hydroxylation process alone. H_2O_2 itself is a strong oxidiser and is sufficient for hydroxylating the surface if the glass was left submerged for a much longer duration; timescale of days rather than the minutes that a piranha etching takes. Acetone scrubbed glassware placed on a teflon coverslip holder would firstly be submerged in a 150 ml bath of toluene and sonicated for approximately 20 mins. Secondly, by using the threaded teflon pole, the holder containing the coverslips was lifted from the toluene and placed directly into a 150 ml bath of acetone and sonicated for another 20 mins. Toluene as a solvent can readily dissolve plastics and oils, and is not water soluble. Acetone's polar nature, arising from it's carbonyl group (C=O), allows it to be water soluble and effective at dissolving any water based contaminants. The acetone wash was also somewhat responsible for aiding in the washing of any toluene residues before continuing into the next step. After the acetone sonication, the coverslips were rinsed thoroughly with Milli-Q water and placed in a third beaker containing 150 ml of Milli-Q water. Next, the beaker of water containing the coverslips was placed in the microwave and bought up to a rolling boil for 3 mins. The glass was boiled in such a way to further aid in the removal of contaminants by both the heating and vigorous motion of boiling; this step would also make sure any acetone traces had evaporated. After boiling and allowing the glass to cool, they were rinsed again with Milli-Q water and placed in a 150 ml bath of 30%wt H_2O_2 and sonicated for another 20 mins. Following the sonication the coverslips were kept submerged in the hydrogen peroxide for at least 24 hrs before use; this was to provide time for the glass surface to undergo hydroxylation. The glass could then be stored in large batches under H_2O_2 in the fridge at 4° C until needed, taking note of the storage duration so that the H_2O_2 could be changed periodically. H_2O_2 decomposes to H_2O and O_2 slowly over time, which would lower the concentration and thus likely impede the glass hydroxylation.

3.1.2 Contact angle study

A simple test could be done to test if the glass had been hydroxylated sufficiently by the H_2O_2 submersion. Using a spherical assumption to model the water droplet size, reported by Chatterjee *et al*[101], one can estimate the contact angle θ of small water droplets if it's volume V and radius r are known using Eq. 3.7. The contact angle gives a measure of the glass's hydrophilicity, smaller angles correspond to greater hydrophilicity. Since the hydroxyl groups are polar, a hydroxylated surface will be hydrophilic. A surface is considered to be hydrophilic when the contact angle θ <90°; hydrophobic when θ >90°.

$$\frac{3V}{\pi r^3} = \frac{2 - 3\cos\theta + \cos^3\theta}{\sin^3\theta} \tag{3.7}$$

To measure the contact angle a 2 μl is placed on the glass coverslip and it's radius measured using the hydrophilicity test pattern. It is comprised of concentric rings that increase in radius outwards by 3 mm per ring. To do so a camera is used to take a picture from directly above, the scale can then be calibrated using the test pattern and the radius of the droplet can therefore be estimated. Using this estimation Eq. 3.7 is solved for θ. The contact angle of a water droplet was measured for 12 glass coverslips that were cleaned using the H_2O_2 method and 2 coverslips that were simply scrubbed using an acetone soaked piece of lint free optics paper. Firstly, it is possible to see by eye in the photographs, Fig. 3.5, that the 2 μl water droplets placed on the H_2O_2 cleaned coverslips spread over a significantly larger area than the droplets placed on the acetone scrubbed glass, which suggests a lower contact angle. Once estimated using the hydrophilicity test pattern there is confirmation that the H_2O_2 treatment has produced a more hydrophilic surface than an out of the box glass coverslip. It is estimated that the contact angle for a H_2O_2 cleaned coverslip is ≈10°, Fig. 3.5.

3.1.3 Nanoparticle samples

Bare gold nanorods (gold rods without a shell) with CTAB, BNRs, that have a LSPR of 605 nm, aspect ratio 2.3, and silica coated nanorods (SNRs) with LSPR of 646 nm with aspect ratio of 2.8 were purchased from Nanopartz. The gold rods were colloidally suspended in H_2O. It was important to ensure that the nanoparticles (NPs) were permanently fixed to the glass substrate so that correlative measurements could be done. Both diffusion over time whilst submerged in silicone oil and optical trapping by the laser can cause NPs to detach from a glass surface if they were simply drop cast or spin coated on to the surface. NPs were covalently bound to the glass substrate using an intermediate functionalisation molecule that attached to the hydroxyl groups formed during the H_2O_2 treatment on the glass. For covalently binding the raw gold NRs to glass, (3-Mercaptopropyl)trimethoxysilane (3MT) was used [2, 3, 102, 103, 104, 105]. 3MT functionalisation of the hydroxylated glass coverslips results in the silanisation of the hydroxyl group on the glass, leaving the sulphur atom present from the 3MT readily available for binding to a reducing agent, in this case binding directly to the metallic NP, see Fig. 3.7 ii.). The silica coated NRs contain a surface amine functional group on the outer silica shell, therefore tosyl chloride (4-toluenesulfonyl chloride) was used to functionalise and covalently bind the NRs to the glass. Similarly, the hydroxyl groups on the glass react with the tosyl chloride forming a tosyl-activated intermediate, a sulfonyl ester, which is

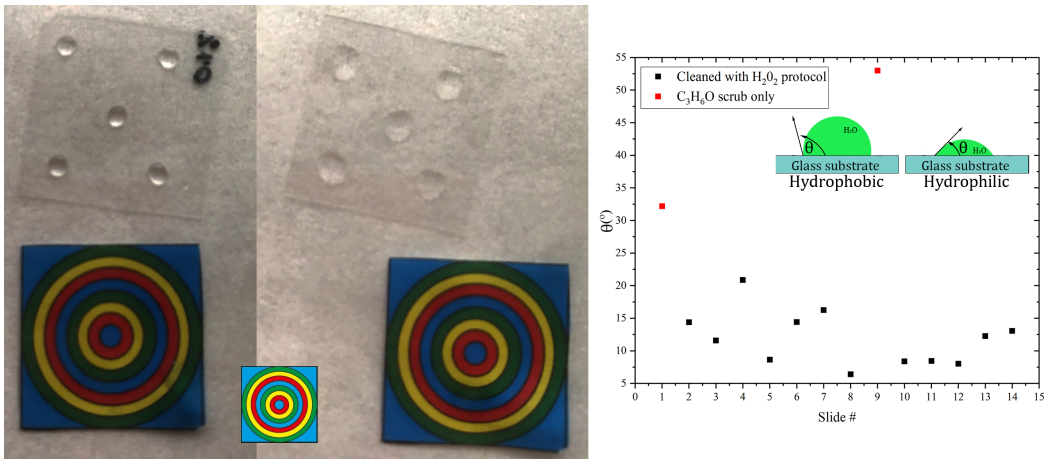

Figure 3.5: Left: Picture of five 2 μl droplets of deionised water pipetted on to an acetone (C_3H_6O) scrubbed glass coverslip. Middle: Picture of five 2 μl droplets of deionised water pipetted on to a glass coverslip cleaned by the H_2O_2 and solvent bath sonication method. A graphic of the hydrophilicity test pattern is also shown for clarity, each concentric colour ring has a radius 3 mm larger than the previous. Right: Contact angle measured for 12 glass coverslips cleaned by H_2O_2 method and 2 coverslips that were only acetone scrubbed. Ploy inset: Sketch of the contact angle measurement for both a hydrophobic and hydrophilic substrate.

then nucleophilically attacked allowing the nitrogen present in the amine of the gold functional group to bind with the silicon in the glass [4], see Fig. 3.7 iii, iv.). Tosyl chloride was chosen specifically as it has a short linker chain, such that it would not contribute significantly to the CARS signal in the vicinity of the rods.

3.1.3.1 Functionalisation protocol

Cleaned and hydroxylated coverslips are firstly rinsed of any H_2O_2 residue with DI.H_2O, and dried with N_2. A functionalisation solution of 3MT or tosyl chloride is then prepared in a 100 ml beaker; the 3MT solution used was 1% by volume 3MT to Toluene, and the tosyl chloride with acetone solution was 10% by weight tosyl chloride. The coverslips were placed in a teflon holder, submerged in the functionalisation solution of choice and left for up to 1 hr. Using the rod to lift the teflon coverslip holder, they were removed from the functionalisation solution and rinsed sequentially in 3x100 ml beakers containing the corresponding solvent by swirling gently. Following the solvent wash, was a sequential rinsing in 3x100 ml beakers of DI.H_2O. Finally, the coverslips were dried with N_2 and stored under N_2 atmosphere in falcon tubes.

3.1.3.2 Sedimentation of nanoparticles

The process is the wetting of functionalised surfaces with a solution of NP's so that by slow diffusion over time NPs will covalently bind to the glass as shown in Fig. 3.7. The sedimentation protocol is the same for both 3MT and tosyl chloride binding. Functionalised coverslips are marked (so that the top surface where nanoparticles are going to be bound can be identified) and placed in a petri dish on a piece of lint free optics paper. A dilution of NP in H_2O was made to achieve a concentration of

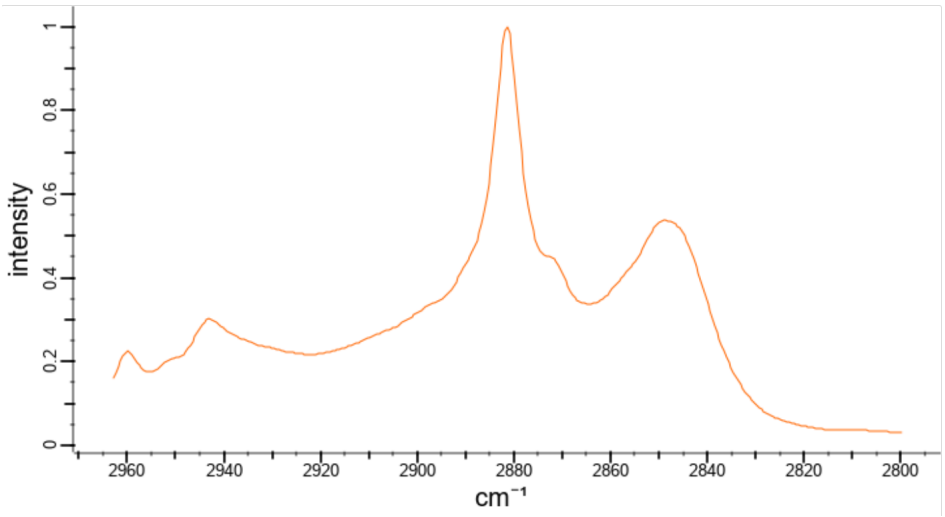

Figure 3.6: CTAB Raman spectrum obtained from *Wiley Spectrum bank* [1]

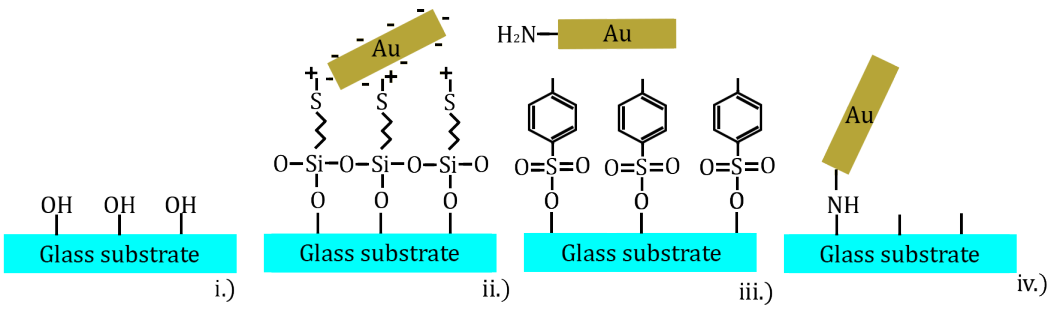

Figure 3.7: i.) Hydroxylated glass substrate. ii.) Gold nanoparticle bound to the glass substrate by silanisation of the hydroxyl group. iii.) Tosyl-activated intermediate, with an amineated gold NR in the vicinity. iv.) Gold nanorod bound to the glass substrate by amine linkage of the tosyl activated intermediate [2, 3, 4] (charges on the gold rod indicate a negative zeta potential).

10^7 ptl/ml (ptl=particles), which gives a separation of ≈1 ptl/μm in the final sample. To aid in avoiding aggregation a pH buffer was added to the dilution, adjusting the pH according to the zeta potential of the specific NP used. Aggregation of NR's would mean the local field enhancement is arising from a larger volume, increasing the resolution limit and provide a greater enhancement than one would expect from one particle. The NP solution was added one, ≈10 μl, droplet at a time to the top surface of the coverslip until a meniscus forms covering the entire surface. Once coated, a piece of paper towel soaked in H_2O was placed near and covered by a large inverted water-bath for up to 1 hr. The paper towel was thought to increase the humidity beneath the waterbath, minimising the amount of evaporation that would cause 'coffee ringing' of particles at the edges of the droplet. After 1 hr had passed, the coverslips were hosed with H_2O and sequentially swirled in 3x100 ml beakers of H_2O before being stored under N_2 in a falcon tube, making sure the side of the slip containing the NPs was marked.

3.1.3.3 Squeezed silicone oil samples

Glass coverslips coated in NPs were squeezed using a vice on to microscope slides separated by silicone oil. The squeezed sample minimised the amount of unfocused debris aberration observed when imaging the sample. A 30 μl droplet of n=1.52 silicone oil is placed in the middle of a hydrogen peroxide cleaned slide and a NP coated coverslip is placed on top; the NP side making contact with the silicone oil. The slide and slip were then wrapped in a piece of optics paper, and protected by placing a sacrificial glass slide and off-cut of cardboard on top and below, Fig. 3.8. The cardboard protected the glass from the sharp edges of the vice, whilst the sacrificial glass ensured a flat squeeze was applied to minimise lateral drift. Optics paper was added to prevent scratching. The configuration was placed inside a vertically mounted vice and clamped tightly together; ensuring that the stationary part of the vice was at the bottom to aid with aligning the squeeze. After squeezing, the sample slide and coverslip were wiped of excess silicone oil and sealed with nail varnish around the edges. This typically yielded a silicone oil layer thickness of 10 μm.

3.1.3.4 3MT's effect on hydrophilicity

The hydrophilicity of coverslips functionalised with 3MT was tested using the spherical assumption model Eq. 3.7 for a 3MT concentration range of 0%-1% (by volume). One can clearly see that the hydrophilicity falls with increasing concentration of 3MT, suggesting that the 3MT is reacting with the hydroxyl groups on the glass Fig. 3.9. An important outlook to take from this result is the following. If one would want to attach biological material, such as a lipid bilayer, on top of the covalently bound nanoparticles there would need to be some consideration for the effect of attaching such material to a less hydroxylated surface.

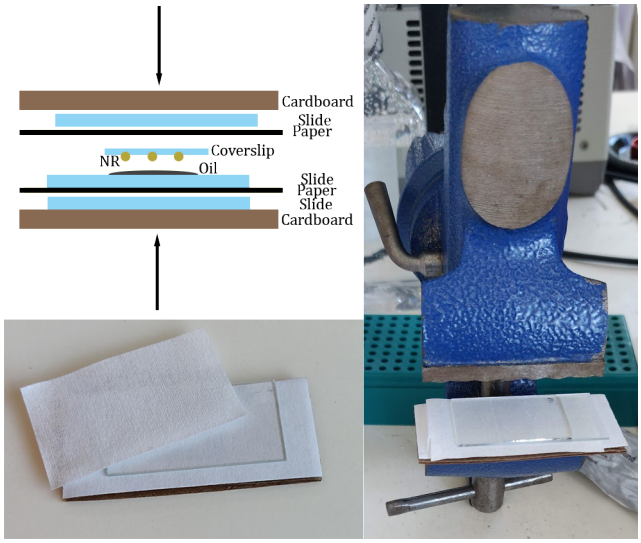

Figure 3.8: Top left: Sketch of how the sample was protected whilst squeezing with a vice; the arrows show the direction the force was applied. Bottom left: Sacrificial slide and off-cut cardboard covered with optics paper used to protect the sample. Right: Sample mounted in the vice without the top layer of protection added.

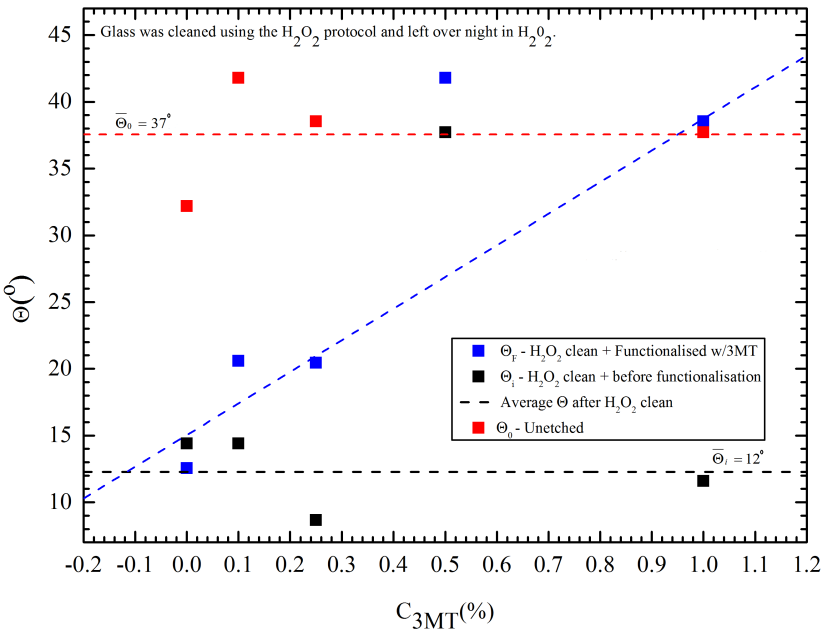

Figure 3.9: Estimated hydrophilicity of coverslips treated with 3MT in a range of different concentrations. Calculated using the spherical assumption model and hydrophilicity test patterns, see Fig. 3.5. Fit values that are extrapolated to negative concentration values are to be ignored, they are included to ease reading the zero concentration contact angle values.

3.1.4 Oil-droplets

A 24 mm x 24 mm imaging gasket from Sigma, with imaging well diameter of 20 mm and thickness of 0.5 mm, was glued to the centre of a microscope slide that had been cleaned by the H_2O_2 protocol. A solution of 0.25% Agarose in DI.H_2O was prepared in a falcon tube and heated in the microwave until dissolved. 30 μl of agarose was pipetted into the centre of the imaging gasket, with a further 5 μl of silicone oil pipetted on top of the agarose droplet. Silicone oil is not soluble in water, therefore, when a cleaned coverslip is placed on top, sealing the imaging gasket, the oil is pressed against the coverslip forming dome shaped oil droplets on it's surface.

3.2 Microscope setup

3.2.1 Microscope stand

Our multimodal imaging system is based on an inverted Nikon Ti-U microscope stand (objective is below the condenser). The microscope has a 100W Halogen white light with variable intensity and an adjustable filter wheel. A piezoelectric NanoLP200 nanostage with xyz degrees of freedom and 0.4 nm resolution, is mounted on to a xy micromechanical stage, the sample mounting configuration is shown in Fig. 3.10. The stand has both a CMOS 10.1 megapixel Canon EOS 40D, and sCMOS PCO Edge 5.5 (PCO) cameras attached (specifications to follow).

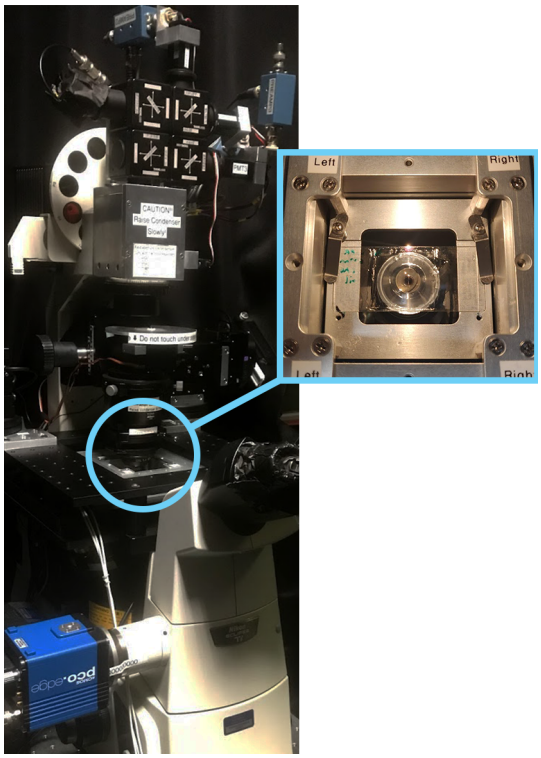

Figure 3.10: Picture of the Nikon Ti-U microscope. Circled in blue is the mounting location of the sample, a sample is shown mounted for reference.

3.2.2 Microscope elements

Objective: 100x oil

Nikon CFI plan Apo lambda series 100x, 1.45NA, n=1.518 oil immersion objective, with a working distance of 0.13 mm. Chromatically corrected for 435 nm to 850 nm. 0.17 mm coverslips are to be used.

3.2.2.1 Objective: 60x water

Nikon CFI plan Apo IR Lambda-S Nano Crystal 60x, 1.27NA, n=1.33 water immersion objective, with a working distance of 0.17 mm. Chromatically corrected for 435 nm to 1064 nm. 0.15 mm to 0.19 mm coverslips can be used. This objective has an adjustment collar that adjusts the position of the central lens group to account for variations in glass coverslip thicknesses. When using a high numerical aperture coverslip thickness variations can cause abberation. The collar was adjusted to optimise the SRS signal in the silicone oil as shown in Fig. 3.11.

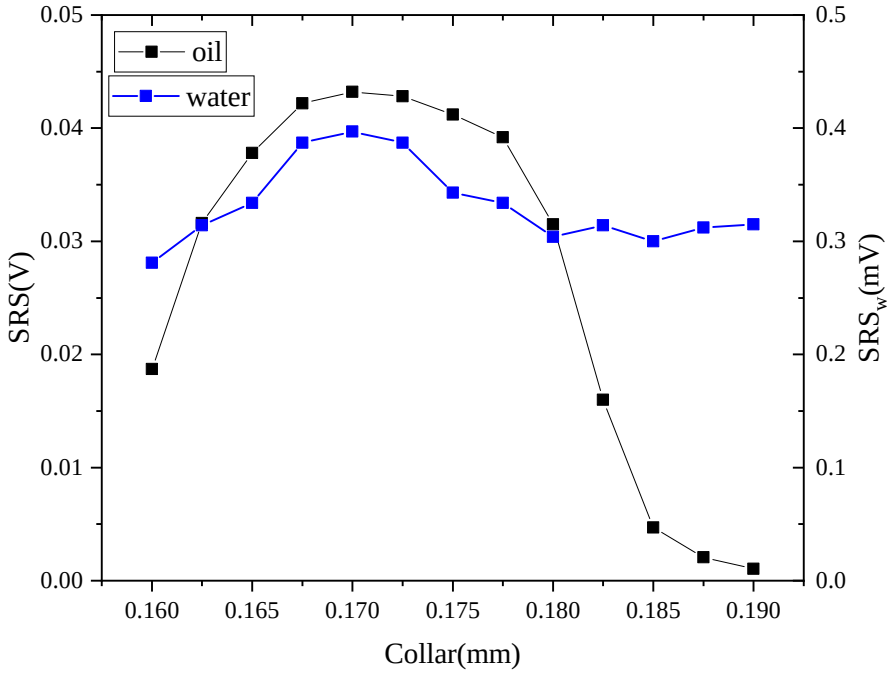

Figure 3.11: Collar ring adjustment to an SRS signal from silicone oil at 2904 cm^{-1}

3.2.2.2 Condenser: 1.34NA oil

Nikon 1.34NA HNAO lens n=1.518 oil immersion condenser, with a working distance of 1.96 mm, focal length of 10.5 mm and far field diameter of 28.1 mm.

3.2.3 Extinction

Characterisation of NPs geometrical shape can be performed by either wide-field extinction or single particle extinction spectroscopy in our setup utilising a technique described in detail by Payne *et al* [106, 107, 108]. Widefield extinction was performed using the CFI plan Apo lambda series 100x, 1.45NA, n=1.518 oil immersion objective. A rotatable linear polariser, situated above the condenser, was rotated to

provide the in-plane polarisation angle (θ) to the halogen white light illumination in steps of 30 °from 0 °to 150 °. Two images, I_1 and I_2, were taken of the sample at corresponding positions P_1 and P_2, shifted by S, calculated by first calculating

$$R_i = \frac{3\lambda}{2NA} \tag{3.8}$$

Where R_i is the measurement radius of the NP, given by the illumination λ, and the NA of the objective. S is calculated by

$$S = 2R_i + 100\,nm \tag{3.9}$$

to avoid overlap of airy patterns. The shift was applied in the x axis of the nanostage using the PCO.edge 5.5 sCMOS camera to detect the transmitted light. 128 averages at both positions were done in the camera software, using a 20 ms exposure, using the full sensor size of 2560×2160 pixels to capture the maximum amount of particles in the field of view. The normalised transmission is calculated by,

$$T_+ = \frac{I_1}{I_2} \tag{3.10}$$

with the T_+ denoting that the I_1 image has been chosen as the signal and I_2 the reference. The shift was repeated to produce a sequence of N=10 sequential images at each position (P_1,P_2,P_1,P_2....etc), and were sequentially averaged to reduce the systematic sensor noise. The extinction image, $\Delta_\pm$, is calculated as follows,

$$\Delta_\pm = 1 - \frac{1}{N}T_\pm \tag{3.11}$$

and contains both a positive Δ_+ and negative Δ_- contrast separated by the shift, S, along the x axis.

For single particle spectroscopy the setup is nearly identical to wide-field extinction; able to use the linear polariser and white light illumination through the 100x objective. Instead of detecting the transmission in a camera the signal is sent to a spectrometer. A single particle is aligned in the centre of the spectrometer slit opened and is illuminated with white light to produce two shifted spectra I_1 and I_2, similarly to widefield extinction. The spectrum is collected utilising the Horiba Jobin-Yvon spectrometer and Andor camera, by taking 200 acquisitions, at P_1 and P_2 separately, with an exposure of 11ms, with the 100lines/mm grating and input slit opening of 80 μm. The slit parameters correspond to a spectral resolution of 1.2nm/pixel. A 2x5 binning of the Andor CCD was used to aid with vertical particle localisation and to provide bins with a local reference that could be subtracted to improve the noise. The size of the bins were chosen to minimise the leakage of signal from the centre bin. The normalised spectrum is calculated from the centre bin's spectrum using

$$T_+ = \frac{I_1 - I_{1,\mathrm{r}}}{I_2 - I_{2,\mathrm{r}}} \tag{3.12}$$

where I_r is the average of the background signal in the adjacent bins that do not contain NP signal Eq. 3.11 is then used to calculate the extinction spectrum, which can be repeated for numerous polarisation angles.

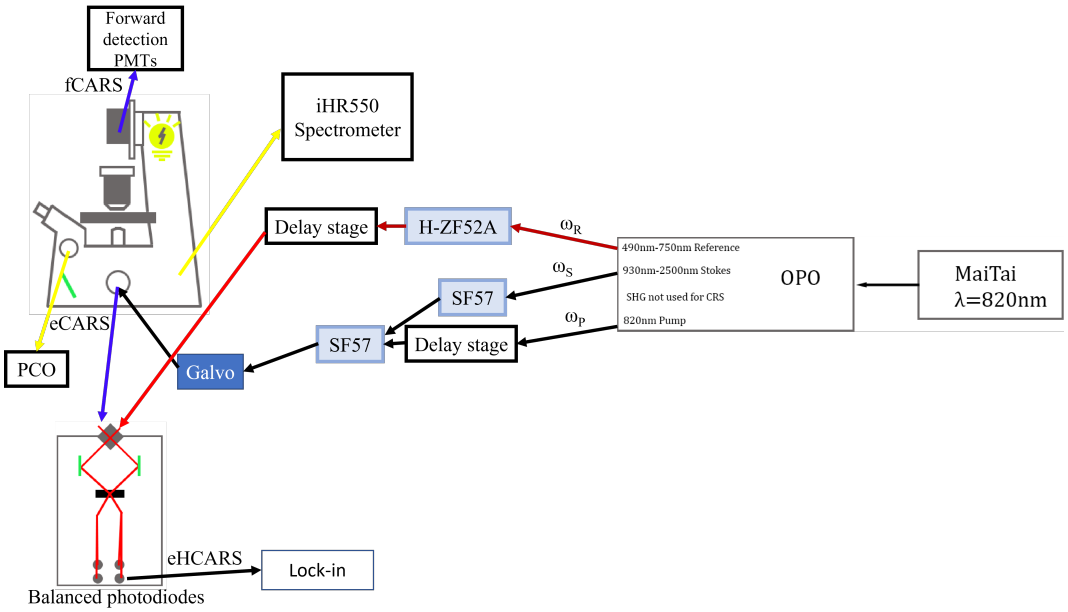

Figure 3.12: Sketch of the setup showing the key components.

3.2.3.1 PCO.edge 5.5 sCMOS Camera

Scientific CMOS 5.5mega pixel (2560x2160pixels with 6.6 μm pitch) is a low noise water cooled camera used primarily for wide-field sample navigation and extinction measurements. At full resolution the PCO is capable of recording at a frame rate of 100 Hz and at 1024x1024, 200Hz. It has 3×10^4 e full well capacity, and 1.1 e rms read noise. The low read noise makes the PCO an excellent tool for imaging NPs in widefield.

3.2.3.2 Horiba Jobin-Yvon iHR550 spectrometer

Czerny-Turner type imaging spectrometer with 550mm focal length that has 3 gratings; 150 l/mm, 600 l/mm, and 1800 l/mm, offering the option of high spectral resolution or high throughput.

3.2.3.3 Andor CCD

Attached to the iHR550 spectrometer is the water cooled DU-971N, Newton, Andor CCD utilised for detecting the specta. The sensor is made from 1600x400pixels that are 16x16 μm in size. It is an electron multiplying CCD, the charge on each pixel is multiplied before readout, that can be cooled down to -100° C which allows for single photon sensitivity with a maximum of 3.6fps at full resolution.

3.2.4 epi-Heterodyne-CARS setup

3.2.4.1 Setup description

The Spectra Physics MaiTai is a mode-locked titanium-sapphire tunable (690 nm to 1040 nm) laser; the fundamental remains at 820nm in our setup. It provides 100 fs pulses with repetition rate of v_L=80 MHz that are frequency doubled to pump a Inspire Radiantis Newport/Spectra physics OPO; outputting the pump, signal and

idler beams at a pulse duration of approximately 150fs at 80 MHz. In our setup, the 820 nm fundamental is used as the pump beam, the idler is used as the tunable Stokes beam. The signal beam is tunable in the wavelength range 490 nm to 750 nm and corresponds to an idler range of 930 nm to 2500 nm. The excitation fields are co-linearly polarised exciting the OPO (horizontally orientated relative to the table). To perform CARS by spectral focussing, specific length and anti-reflection coating dispersive H-ZF52A and SF57 glass blocks from Fortune optics were used to apply an equal linear chirp to both pump and stokes pulses, providing an instantaneous frequency difference (IFD) between the pump and stokes. The glass blocks can be interchanged to provide varying amounts of linear chirp dependent on the IFD required. Both fields are recombined by a dichroic beamsplitter, and then move onwards to the sample generating the CARS signal by driving molecular vibrations at the selected IFD. The IFD can be tuned by adjusting the time delay of the pump beam using a 15 cm PI-Linear delay stage, M-403.8PD, the spectral resolution is then given by the elongation of the temporal envelope by a few picoseconds [109].

Epi-CARS signal recombines with the reference beam at a non-polarising beam splitter (NPBS). For heterodyning the reference beam is also linearly chirped by H-ZF52A glass blocks and a delay is provided to it by a PI-Linear delay stage. The chirp and delay is adjusted to achieve spectral and temporal overlap (accounting for the additional chirp the CARS field experiences propagating through the optics of the microscope stand) with the generated epi-CARS signal before the two fields recombine. The two beams, from the interference between the CARS and reference fields after the NPBS, are separated into horizontal and vertical polarisation components using a Wollaston prism (WP). The resulting four beams are then detected by two balanced pairs of photodiodes, using the photo-current difference between the two pairs of diodes; the horizontal polarisation is focussed on the top pair and the vertical on the bottom. Heterodyne detection is done with a dual-channel lock-in amplifier to detect the interference of the epi-CARS signal with the reference beam. This is done by using an TeO_2 acousto-optic modulator (IntraAction) and driver to up-shift the optical frequency of the stokes beam to v_s=77 MHz, resulting in a $-v_s$ shift to the CARS field (the CARS field is proportional to the complex conjugate of the stokes field), the resulting beat frequency, v_L - v_s=3 MHz, is detected.

The setup is also capable of detecting forward scattered signals, such as forward-CARS and two photon fluorescence (TPF). Photon multiplier tubes (PMTs) are attached in forward detection to the Nikon Ti-U microscope. There are a series of dichroic and bandpass filters ordered in such a way that wavelengths of 642 nm - 707 nm are sent to the CARS PMT, 468 nm - 552 nm to the TPF PMT, 391 nm - 437 nm to the SHG PMT, and 790 nm - 860 nm to the SRS photodiode. FCARS is generated in exactly the same way as the eHCARS signal but is detected in forward geometry as an intensity rather than a field. SRS, on the other hand, utilises the stokes beam AOM to modulate the amplitude and detect the stimulated raman loss at the pump field as an intensity modulation at a photodiode using a ZI HF2 lock-in amplifier. Mounted on the Nikon Ti-U microscope is a LP200 mad city labs piezoelectric nanopositioning stage, and manual microstage-LT that can be used to scan the sample coarsely in a 25 mm x 25 mm range. However, for a finer scan it is possible to move the nanostage with a resolution of 0.4 nm over a range in XYZ of 200 μm^3 with 15 ms response time. The CARS microscope utilises a raster type

scan to construct images. A Thorlabs PM100 power meter with a silicon photodiode head was used to measure the pump and stokes beams whilst a thermal-sensor head was used to measure the higher power of the reference beam [64, 65].

3.2.4.2 Setup calibration

The CARS wavelength λ_{CARS} is given by λ_{P} and λ_{S} as follows,

$$\frac{1}{\lambda_{\mathrm{CARS}}} = \frac{2}{\lambda_P} - \frac{1}{\lambda_{\mathrm{S}}} \tag{3.13}$$

and has a corresponding IFD given by,

$$\frac{1}{\omega} = \lambda_{\mathrm{P}} - \lambda_{\mathrm{S}} \tag{3.14}$$

The relation between IFD and λ_{CARS} is shown below in Fig. 3.13.

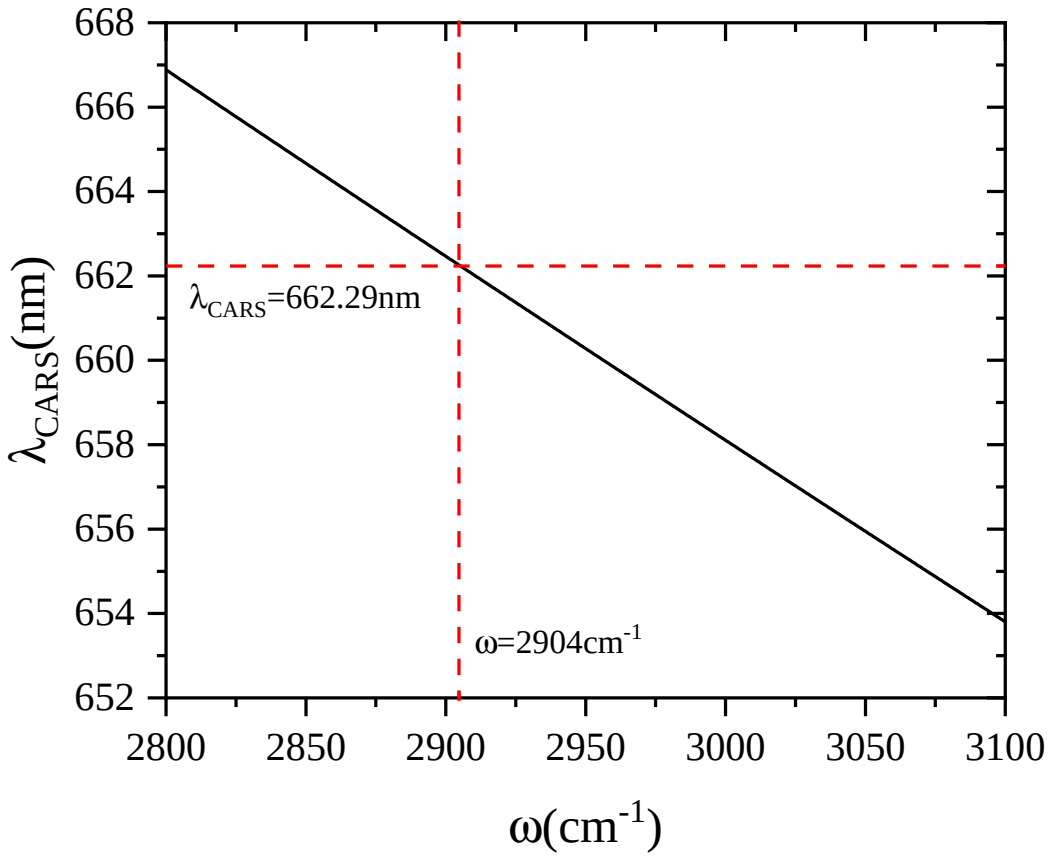

Figure 3.13: Plot of the CARS wavelength and corresponding IFD. The red dotted lines indicate the measurement parameters used for eHCARS measurements of silicone oil.

For calibration of the pump and reference delay a polystyrene (PS) sample was used as it has a well defined aromatic resonance at 3050cm^{-1}, aromatic CH vibrational resonance. Each measurement would follow a calibration where a sample with known vibrational resonance spectrum would be measured first. It should be noted the measurement shown in Fig. 3.14 was taken from a focal plane maximising the

SRS and CARS signal from inside a PS film, hence the eHCARS signal is not maximised and is out of focus. The eHCARS signal is sensitive only to interfaces that are perpendicular to the excitation axis. In this instance the SRS/CARS spectrum is maximised as it is used to calibrate the IFD (delay stage position) the known PS spectrum. The IFD spectrum is obtained by varying the overlap of the linearly chirped pump and stokes, Gaussian, pulses and a range of $150\,\mathrm{cm}^{-1}$ can be probed before the pulses are no longer overlapped.

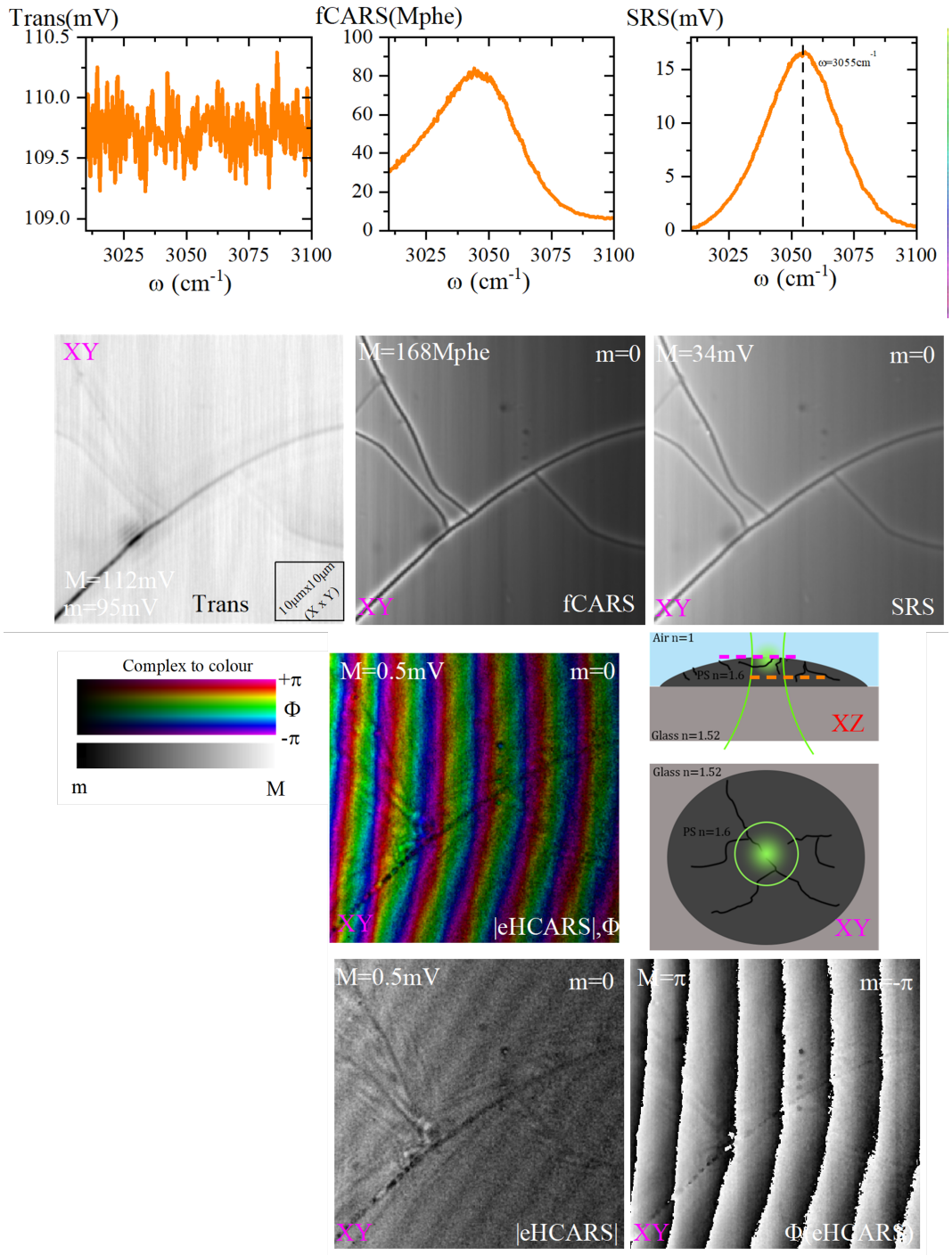

Figure 3.14: Calibration measurement of a polystyrene film on a glass substrate. The top spectra, in orange, are delay scans in transmission, fCARS and SRS, detuning the pump and Stokes overlap to probe a range of IFD's. Below are images in transmission, SRS, fCARS and eHCARS of a drop cast polystyrene film on a glass substrate. 100x 1.45NA objective, 1ms dwell time, 50 μmx50 μm xy image. The image labelled |eHCARS| is the eHCARS amplitude and Φ is the eHCARS phase. The Φ|eHCARS|,Φ image shows the amplitude and phase encoded into a value-hue plot, where the amplitude is the value and the phase is the hue. A sketch is included illustrating the sample geometry and planes of an XZ and XY scan. A 10 μmx10 μm box is shown in the transmission image, representing the scale in 2D (scale is conserved between XY and XZ measurements).

An example power dependence of the eHCARS (amplitude) from a glass-oil interface is shown in Fig. 3.15. The glass-oil signal power dependence was used to aid in the retrieval of the interface signal, when calculating the complex enhancement ratio, when using low pump and Stokes powers imaging gold nanorods.

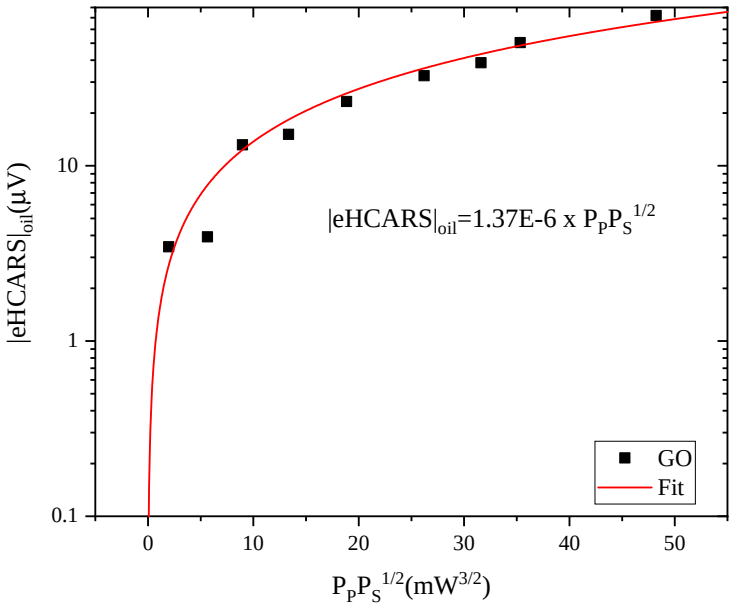

Figure 3.15: Glass-oil interface eHCARS power dependence.

eHCARS measurements were lock-in offset corrected before analysis. The real and imaginary parts of the signal were independently centred at zero, example shown in Fig. 3.16

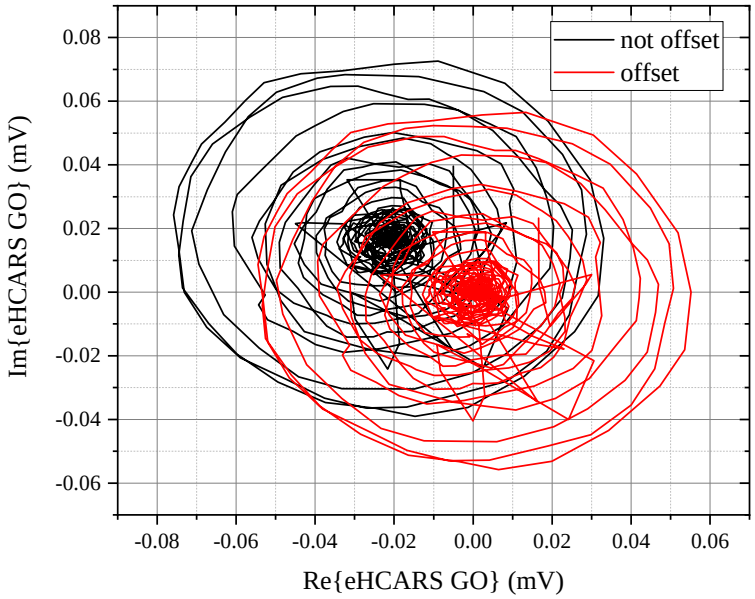

Figure 3.16: Example of the lock-in offset correction for a glass-oil eHCARS signal applied to the real and imaginary parts of the measured eHCARS signal.

Chapter 4

eHCARS from oil droplet interfaces

In this chapter a model oil droplet sample was considered to illustrate the advantages of epi-detected heterodyne CARS over fCARS and SRS for interface sensing. Silicone oil was specifically chosen for the model system as it has a very strong resonant peak at $2904\,\mathrm{cm}^{-1}$, see Fig. 4.1. As the future applications of the technique are in the imaging of lipid materials, it is appropriate to select a material that has a resonance within the range of $2800\,\mathrm{cm}^{-1}$ to $3050\,\mathrm{cm}^{-1}$ where one might detect the strong and 0broad -CH vibrational resonances present in lipids.

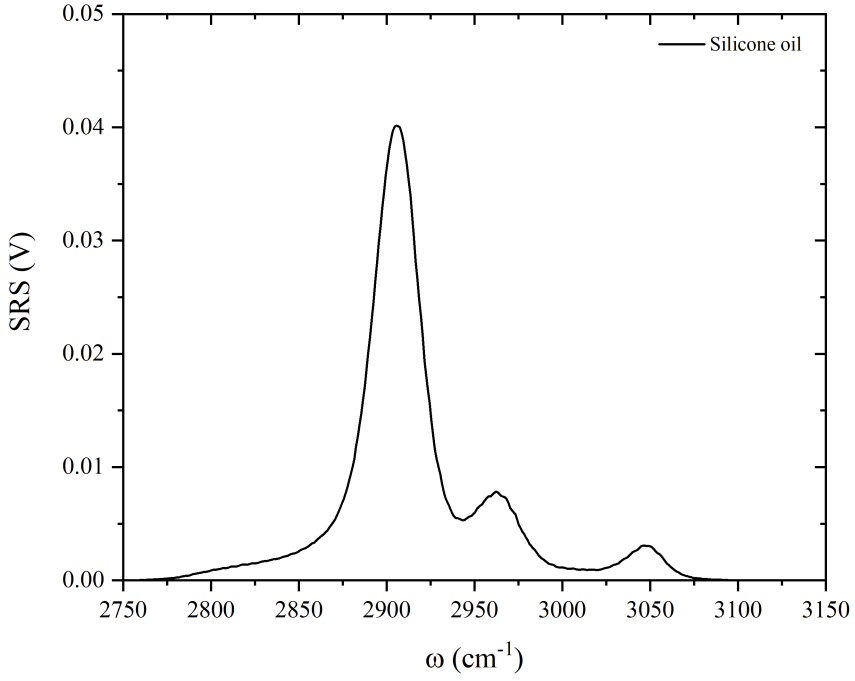

Figure 4.1: Silicone oil SRS spectrum measured by shifting the delay stage to probe IFD's in the range of $2750\,\mathrm{cm}^{-1}$ to $3150\,\mathrm{cm}^{-1}$.

In the regime where objects of interest are smaller than the excitation wavelengths, forward CARS contains a non-resonant background arising from the bulk material. FCARS is only suitable for detecting large objects, whereas one can separate the non-resonant background by detecting the CARS signal in epi-direction.

ECARS is generated from the interface, perpendicular to the epi-direction, of two large materials with different $\chi^{(3)}$ or from scattering objects smaller than the excitation wavelength [59]. Forward generated CARS may also be epi-reflected from a surface and detected in epi-direction. This selective sensitivity to perpendicular interfaces and small objects, combined with the full field information retrieved from a heterodyne detection, is what provides nanoscale topographical detection. Oil droplets on a glass substrate in water were considered to characterise and better understand the behaviour of epi-detected heterodyne CARS signal from different interfaces. Oil droplets were placed on a glass coverslip forming hemispheres (dome like shape). The sample was prepared by fixing silicone oil droplets on to a glass coverslip and sealing in an agarose environment with a gasket, see Sec. 3.1.4. What was to be imaged then was an array of various sized oil droplets attached to the flat glass surface below, surrounded by a 0.25% solution of agarose in water. A differential interference contrast (DIC) image, shows how the oil droplets have been attached to the glass coverslip in Fig. 4.2.

It is evident from the DIC image that the oil droplets consistently form relatively smooth shaped hemispheres on the glass surface. Both the 20 μm and 12 μm diameter droplets have what could be small bubbles of air or water trapped inside. Some of the droplets have not formed hemispheres with a perfectly circular base attaching to the coverslip. If one was concerned about the shape uniformity of the droplets then it would likely be beneficial to not press on the cover slip as the agarose is setting around the droplets. In this case the coverslip was squeezed slightly as the agarose was setting, possibly distorting the shape of the oil droplets. However, the droplet shape was not overly important for the experiments that were to follow. What was required from this sample was the three different interface types between the different materials. Moving upwards ($+z$) relative to the plane shown in Fig. 4.2, everywhere outside the oil droplets there is an interface between glass and water (GW), inside the oil droplets there is a glass-oil interface (GO), and at the top of the oil droplet there is an oil-water (OW) interface. Each interface provides a different situation with respect to the change in their non-linear susceptibilities ($\chi^{(n)}$).

4.1 Forward detected CRS vs epi-detected eHCARS

The epi-detected signal from the oil droplets was firstly compared with the forward detected measurement capabilities of the setup. Three dimensional SRS, fCARS and eHCARS measurements of the silicone oil droplets were taken at the IFD=2904 cm^{-1} , the vibrational resonant peak of silicone oil. By moving the nano stage to perform the raster scan, producing the images pixel by pixel. It is not possible to scan the laser with the galvo mirror in heterodyne epi-detection as it would change the overlap of signal and reference fields. How the sample was mounted is shown in Fig. 4.3, the coverslip is below the microscope slide making contact via immersion oil with the 60x 1.27NA water immersion objective below. The oil droplet and agarose can be seen above the coverslip. The z direction is defined as the epi-direction, $+z(-z)$ going up(down) through the objective, and the xy plane is defined as the flat coverslip surface. A sketch of an oil droplet in both the xy and xz plane is shown in Fig. 4.3. It is marked on the sample sketch where exactly the xz and xy scans have been performed, the cyan line through the centre of the xy plane shows the location

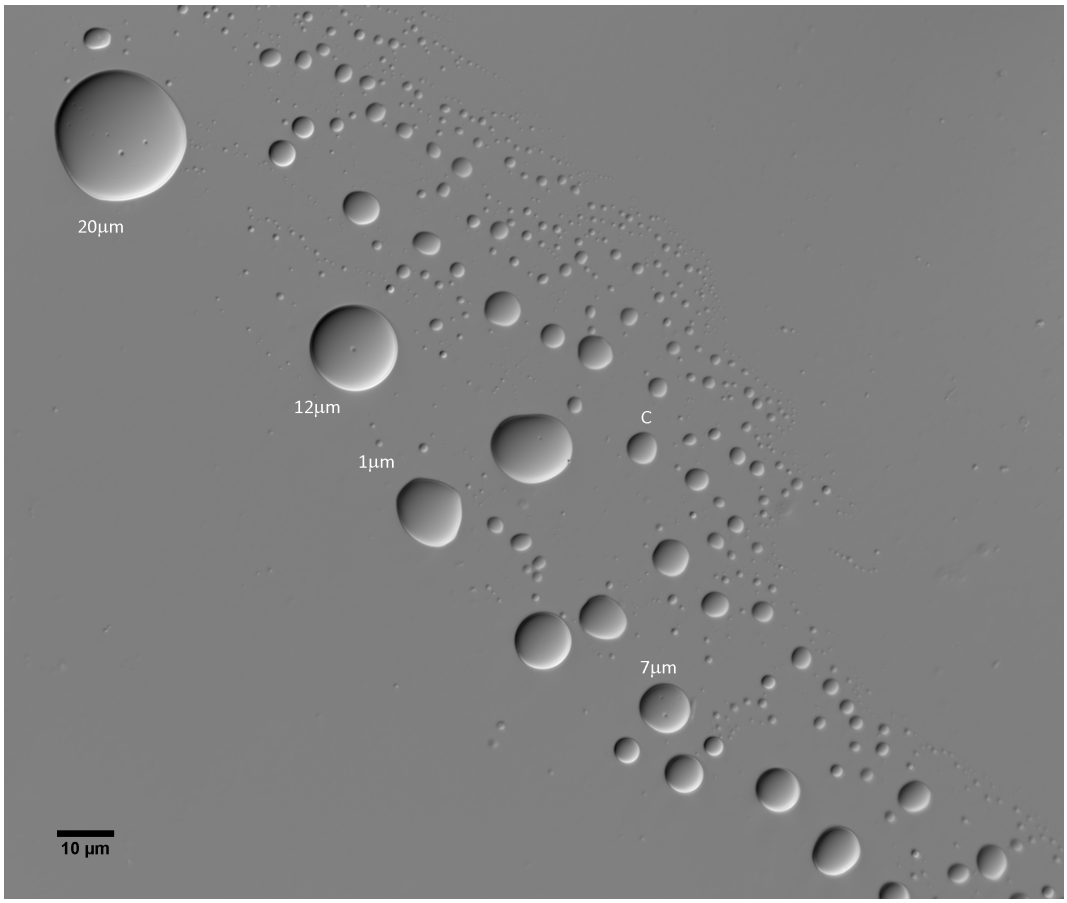

Figure 4.2: DIC I_C image of silicone oil droplets supported on a glass cover-slip, fixed in an 0.25% agarose and water environment (agarose/water is above the plane shown, below is the glass cover-slip). 60x 1.27NA water immersion objective, rotating the polariser $\pm 15\,^{\circ}$. Gray scale is from black to white (-0.1733 to 0.1744). A black scale bar is provided, with specific droplet diameters labelled in white.

where an xz scan was performed by moving through the focus, holding the y position constant and scanning along the x direction. The pink line on the sketch shows where the sample was scanned in the xy direction keeping the focus constant at the GO interface, the red line is the same xy scan but at the OW interface. The orange line indicates where the fCARS and SRS spectra were obtained from by keeping both the focus and y position constant, and scanning the pump delay to select a range of IFDs, the resultant 2D image was then averaged along the x direction to obtain the spectra.
The setup is capable of obtaining transmission, fCARS, and SRS simultaneously; eHCARS was measured separately, see Sec. 3.2.4. Images were constructed by scanning a $25\,\mu\text{m}\times25\,\mu\text{m}$ range (in 232×232 pixels), 1 ms per pixel, in the xy plane and a $25\,\mu\text{m}\times15\,\mu\text{m}$ range (in 232×1501 pixels), 1 ms per pixel, in the xz plane. The xz images in Fig. 4.3 have been extruded and cropped in the z direction so that the pixel distance in the z direction is half the x direction pixel distance. SRS and fCARS spectra was obtained by scanning the IFD (changing the delay of the pump pulse to the Stokes pulse in the CRS excitation, see Sec. 3.2.4) in the centre of the oil droplet over a spectral range of $500\,\text{cm}^{-1}$ (in 501 steps) centred at $2904\,\text{cm}^{-1}$. A scale box is shown in the transmission xz and xy images in Fig. 4.3; note, 2 pixels in the z direction, as scaled, corresponds to the same distance in 1 pixel in the x or y direction (scaled distance is shown in the transmission image for both xy and xz as a scaled box). For the fCARS/SRS/transmission/eHCARS images and spectra, 1ms dwell time, with a $P_P = 8.941\,\text{mW}$ and $P_S = 7.699\,\text{mW}$ ($P_S = 16.28\,\text{mW}$ for eHCARS). Spectra was taken in $500\times1\,\text{cm}^{-1}$ IFD steps.

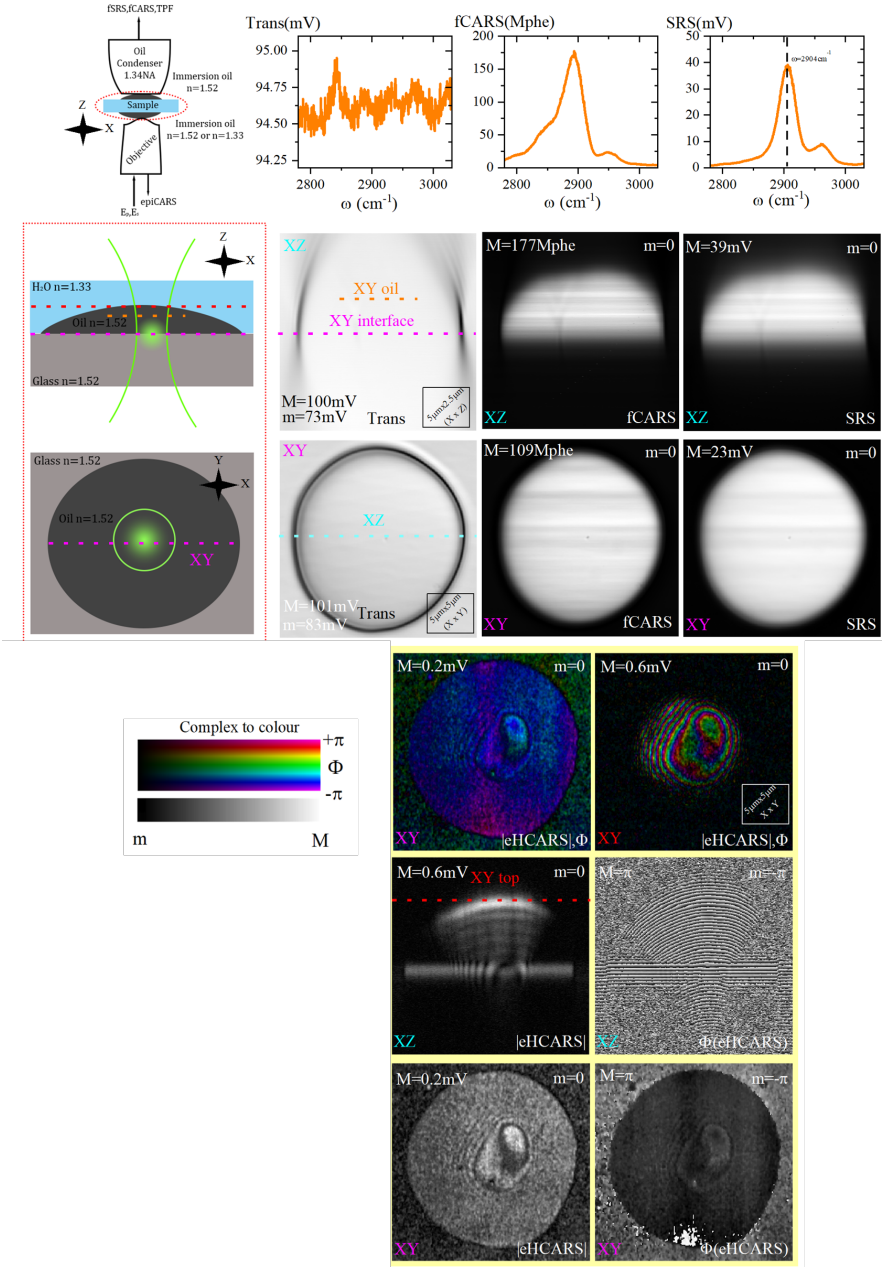

Figure 4.3: EHCARS, SRS, and fCARS of a silicone oil droplet in 0.025% agarose and water at 2904 cm^{-1}, using 60x 1.27NA water immersion objective with correction collar optimised, 1.5x tube-lens, and 1.34NA oil condenser. Top spectra in orange is a delay scan taken in the middle of the oil droplet, detuning the overlap of pump and Stokes beams to obtain an IFD spectrum in transmission, fCARS and SRS. Across the middle are images in forward detection; transmission, SRS, and fCARS of the oil droplet. Below, in the yellow box, is the epi-detected signal in the horizontal polarisation component. The image labelled |eHCARS| is the eHCARS amplitude and Φ is the eHCARS phase. The Φ|eHCARS|,Φ image shows the amplitude and phase encoded into a value-hue plot, where the amplitude is the value and the phase is the hue. A sketch is included illustrating the sample geometry and planes of an XZ and XY scan. The sketch illustrates the sample geometry of the oil droplet and the planes represented by XY and XZ. A 2D box is shown in the transmission images which denotes the scale in 2D for the XY and XZ measurement. M and m are the max and min greyscale values of their corresponding image.

The forward detected SRS IFD spectrum, in Fig. 4.3, only contains the resonant contribution to the signal, which is proportional to the $\mathrm{Im}\{\chi^{(3)}_{oil}\}$. The forward detected CARS on the other hand has both resonant and non-resonant contributions to the signal. Interference between the contributions cause a broadened and slightly distorted (dispersive) line shape in the fCARS IFD spectrum compared to the SRS. The forward SRS, CARS and transmission provide good image contrast in the XY plane. In forward detection, with a dominant resonance and a surface parallel to the detection direction (edge of the circle), it is possible to resolve the oil droplets diameter of $\approx$20 μm in each detection type. In transmission the droplets perimeter is a black ring, due to beam refraction and diffraction reducing the transmission at the edges. Whereas in both SRS and fCARS, being chemically specific, the contrast is provided by the resonance in the oil dominating the signal from the water/agarose. In the forward detected xz images it is more difficult to estimate the height of the oil droplet and locate the top interface. This is due to the axial point spread function causing a distribution of the interface signal from the forward techniques. In the xz transmission image it is impossible to resolve the top of the oil droplet as there is very little light being reflected/refracted to give contrast. However, it is possible to estimate that the interface should be at the z position where there forward signal is minimised at the perimeter of the droplet (where the oil makes contact with the glass). Both the SRS and fCARS xz images reveal the hemisphere shape of the oil droplet, but slightly distorted compared to eHCARS. The epi-detection allows for better resolving of interfaces perpendicular to the imaging plane.
In contrast to forward detected CRS, in eHCARS the bulk background is separated from the interface signal by detecting in epi-detection, and incoherent background is removed by interferometric detection of the CARS amplitude and phase. In eHCARS both the pump and Stokes beams are linearly polarised along the x-axis in the sample, and both co and cross polarised signal is detected. In Fig. 4.3, only the co-polarised (horizontal) eHCARS amplitude and phase components are shown as this was the dominant contribution with no detectable cross component. In the xz eHCARS amplitude and phase images we see that epi-detected CARS signal can only arise from a backward reflection of CARS signal generated in the forward direction, or a CARS signal generated in the backward direction. A reflected signal arises from a step in the $\chi^{(1)}$ (change in refractive index) and a backwards generated signal arises from a step in the $\chi(3)$. There is a strong signal resulting from a step in the $\chi(3)$ coming from the GO interface, and a combination of both reflected and generated CARS signal coming from the OW interface. The phase of the eHCARS signal from the top interface gives and insight to the curvature of the OW interface. A change in the phase along the plane perpendicular to the epi-direction corresponds to a change in the height of the interface position in a homogeneous medium.

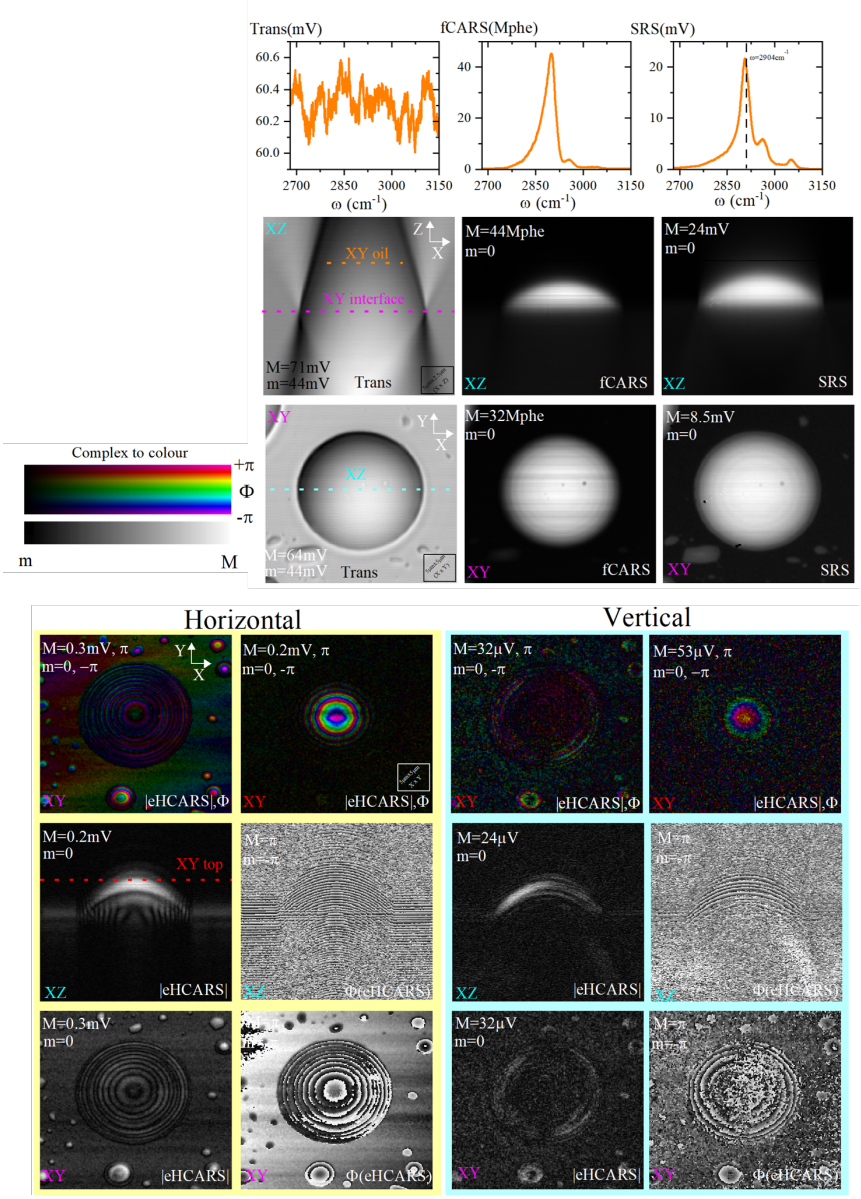

Figure 4.4: EHCARS, SRS, and fCARS of a silicone oil droplet in 0.025% agarose and water at 2904 cm^{-1}, using 100x 1.45NA oil immersion objective with correction collar optimised, 1.5x tube-lens, and 1.34NA oil condenser. Top spectra in orange is a delay scan taken in the middle of the oil droplet, detuning the overlap of pump and Stokes beams to obtain an IFD spectrum in transmission, fCARS and SRS. Across the middle are images in forward detection; transmission, SRS, and fCARS of the oil droplet. Below, in the yellow box, is the epi-detected signal in the horizontal polarisation component, and in blue the vertical component. The image labelled |eHCARS| is the eHCARS amplitude and Φ is the eHCARS phase. The Φ|eHCARS|,Φ image shows the amplitude and phase encoded into a value-hue plot, where the amplitude is the value and the phase is the hue. Lines are sketched on the transmission images illustrating the sample geometry and planes of an XZ and XY scan. The sketch illustrates what is meant by the XY and XZ planes. A 2D box is shown in the transmission images which denotes the scale in 2D for the XY and XZ measurement. M and m are the max and min greyscale values of their corresponding image.

The measurements show in Fig. 4.3 were repeated with the 100x 1.45NA objective, shown in Fig. 4.4. Here we can resolve a cross polarised component, orthogonal to the excitation fields. Polarisation mixing can happen after the non-normal reflection of either the signal or excitation fields at an interface. In Fig. 4.4, the main cross-polarised contribution arises from the curved OW interface, suggesting total internal reflection due to the high angle of incidence from the high NA objective. The higher NA objective has larger collection angles therefore detects more epi signal from curved surfaces. By comparing the XZ traces taken with both objectives, it is evident that the eHCARS signal along the curved interface is detected for larger angles with the 1.45NA objective over the 1.27NA objective.

Both Fig. 4.3 and Fig. 4.4 reveal that there is some contribution to the eHCARS signal that is not strictly localised to the interfaces, namely cone shaped signal originating from the centre of the droplet and signal below the interface. There is also what seems to be interference fringes at both the OW and GO interfaces suggesting multiple signal generation pathways. Looking at the eHCARS signal in more detail, the GO interface is index matched, implying no change in $\chi^{(1)}$, but there is a change in the $\chi^{(3)}$. The GW and OW interfaces are index mismatched, hence there is a reflection provided by the step in $\chi^{(1)}$ as well as a $\chi^{(3)}$ contribution. The GW interface is mostly dominated by the $\chi^{(1)}$ response as the $\chi^{(3)}$ step is negligible. The $\chi^{(2)}$ contribution should be zero for these materials that have inversion symmetry. Non-k conserving parts contribute to the epi-detected signal which scale with the wavelength. The CARS signal scales by the third power of the incident fields, E^3, and the amplitude of the susceptibility $\chi^{(3)}$.
Considering the three different interfaces, noting that the OW interface is curved, there are three possible epi-CARS signal generation pathways, see Fig. 4.5. The first signal shown in Fig. 4.5a, is when the focus is below the GO interface in the glass, creating a CARS signal from the bulk glass material. The CARS signal then propagates with minimal reflection or refraction from the glass, $\chi^{(1)}_{\text{Glass}} = \chi^{(1)}_{\text{oil}}$, into the oil droplet. The propagated signal is then reflected by the curved OW surface and re-focused in epi-direction with an estimated (order of magnitude check assuming planar surfaces) reflection coefficient of,

$$\frac{n_o - n_w}{n_o + n_w} \times 100 = \frac{1.52 - 1.33}{1.52 + 1.33} \times 100 \approx 7\% \tag{4.1}$$

on to the same point the CARS signal was generated. In general, the signal might be reflected in multiple directions off the OW interface, but only detected at it's generation point due to the nature of the interferometric detection where the epi-CARS signal interferes with the reference beam at a specifically defined point in space and time. In other words, since the signal is detected as the product of the CARS field with the reference field, this represents a confocal detection. For the reflected CARS signal to be detected (overlapping the epi-refocussing off the OW interface) the focus must be at the centre of the curvature of the oil droplet. The second signal generation, shown in Fig. 4.5b, arises at the GO interface, where there is a step in the $\chi^{(3)}$ producing epi-CARS with no $\chi^{(1)}$ contribution at this interface. Lastly, shown in Fig. 4.5c, is both an epi-CARS signal generated by a step in $\chi^{(3)}$ between oil and water, and the reflection of CARS signal generated in the oil by the step in $\chi^{(1)}$.

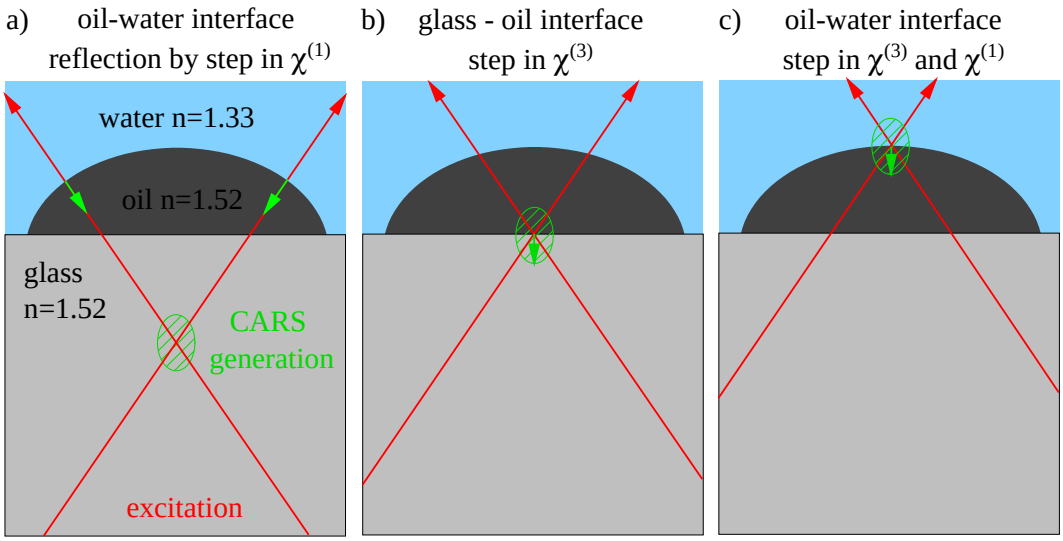

Figure 4.5: Signal generation pathways

v

4.2 eHCARS: different size oil droplets

The aim of the measurements discussed in this section was to determine the droplet size dependence of the eHCARS signal, to avoid complexity, the air very small air pockets that can be seen inside the droplets in Fig. 4.2 were avoided. Two dimensional eHCARS measurements were done on various sizes of oil droplets, in the sample region shown in Fig. 4.2, to investigate the signal generation pathways and see how they contribute to the eHCARS signal. The 60x 1.27NA objective and 1.5x tube lens was used, with the sample being scanned for 1ms per pixel with a pixel size of 0.11 μm in x for each droplet image, and 10 nm per in z. The various curvatures of the OW interface should have a strong influence, according to Fig. 4.5 (a) and (b) signal generation pathways, on the detected signal. Measurements were taken at an IFD of 2904 cm^{-1} resonant peak of silicone oil by moving the nano stage in the xz plane in the centre of the droplet (as was done in the xz images shown in Fig. 4.3). Qualitatively, the signal generation pathways mentioned in Fig. 4.5 can be seen clearly in the amplitude of all three smaller droplets in Fig. 4.6 and in the largest droplet shown in Fig. 4.7.

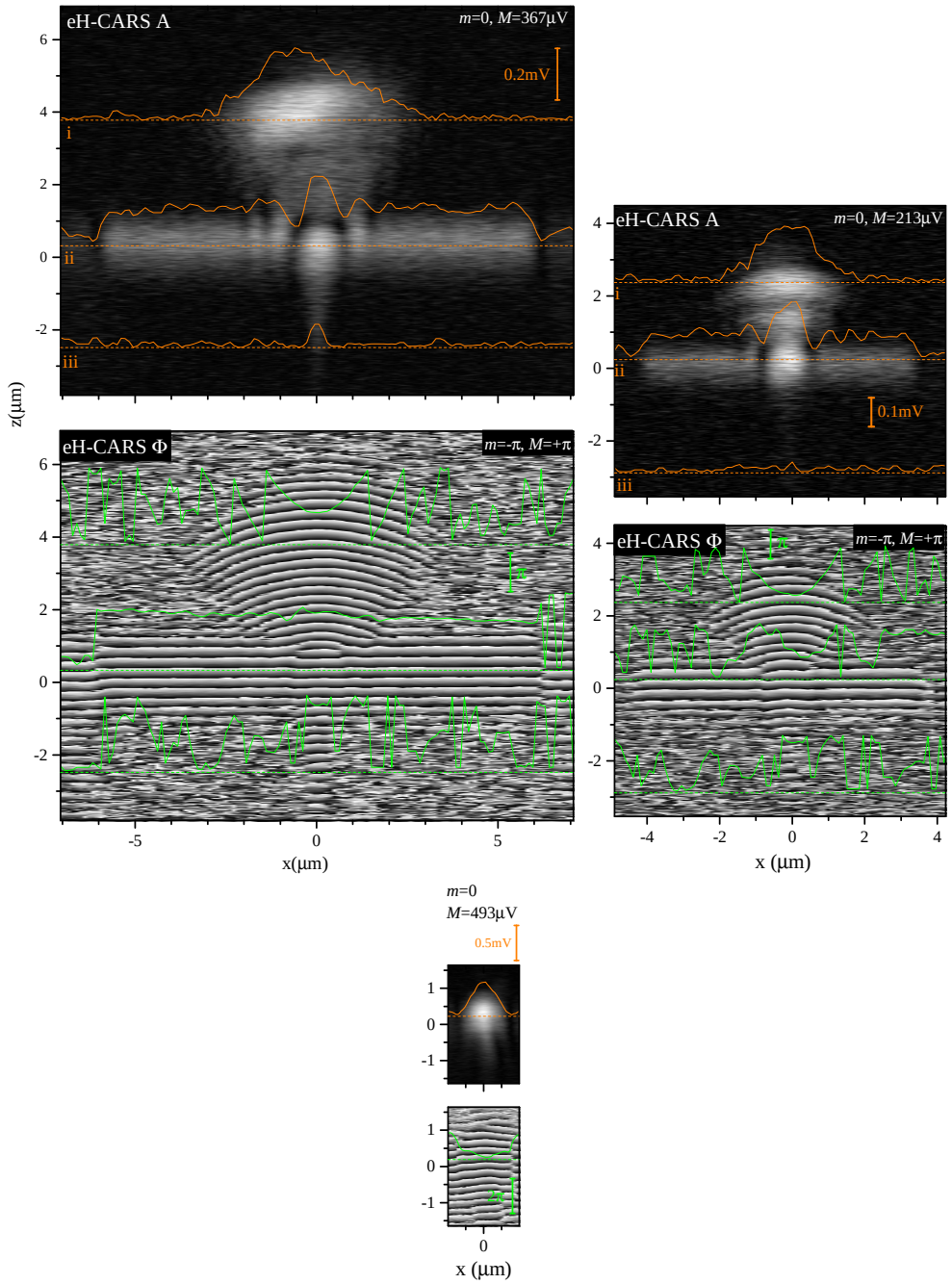

Figure 4.6: eHCARS amplitude and phase in the xz plane from different sized oil droplets on a glass interface surrounded by 0.025% agarose and water. Using a 60x 1.27NA objective and 1 ms dwell time. The 12 μm (left), 5 μm (right), and 1 μm (bottom) diameter droplets imaged are labelled in Fig. 4.2. Maxiumim (M) and minimum (m) greyscale values are shown for both the amplitude and phase images. Data from cuts along the x-axis have been selected from three (i, ii, iii) specific regions, overlayed with their respective dashed line representing the zero value and where the cut was made. The vertical scale is shown by a scale bar of corresponding colour.

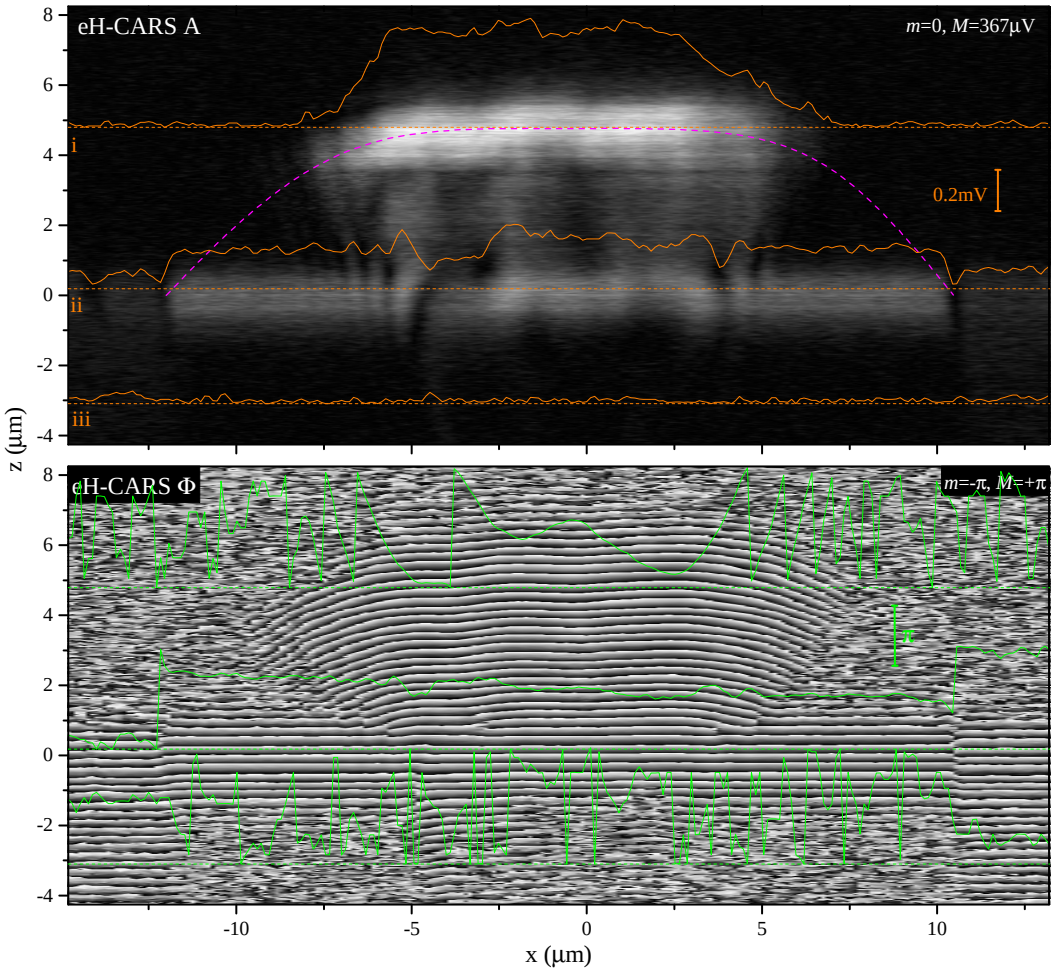

Figure 4.7: eHCARS amplitude and phase image along the xz plane of the 20 μm diameter oil droplet, labelled in Fig. 4.2. See Fig. 4.6 for description.

Signal generation pathway (B), Fig. 4.5b, can be seen along the diameter of the oil droplets GO interface for all oil different sized droplets. eHCARS signal as a result of the step in $\chi^{(3)}$ from glass to oil is relatively constant for each droplet size, $\approx$0.15 mV in amplitude (under the excitation and detection conditions of the experiment previously described) at the interface. The top OW interface has contributions from both a step in $\chi^{(1)}$ and $\chi^{(3)}$. The reflection of the CARS signal off the OW interface at x=0 μm, in the centre of the curvature of the oil droplet, can be seen to extend from the top interface down below the glass interface at z=0 μm. The *iii* cut taken from below the interface shows clearly a spike in the signal near x=0 μm as is expected from pathway (a) for both the 12 μm and 7 μm droplets. The 1 μm droplet's OW interface and GO interface are much closer together, with the OW interface being more curved than for the larger droplets. The increased amount of reflection by the curved OW interface provides a larger eHCARS signal, owing to the increased amount of CARS reflection into the same centre of the droplet; all three signal generation pathways are overlapping within the spacial resolution of the eHCARS image. In the larger droplets, it is possible to see that the CARS signal generated inside the droplet is reflected off the OW interface and interferes with the GO interface signal both constructively and destructively. There are fringes extending along the x axis of the GO interface, which suggest an interference. The

interferometric detection by overlapping the epi-CARS signal with the reference in time and space can only result from epi-CARS sources that are perfectly overlapped with the reference; meaning that the interfering signal must be of the same origin as the GO interface signal.

Symmetry of the smaller droplets provides a more evident (a) signal generation pathway, focusing the CARS signal below the interface. The phase curvature of the OW interface, cut *i*, can be used to determine the smoothness of the oil droplet hemisphere. For the smaller droplets, shown in Fig. 4.6, the curvature seen in the *i* cut phase is smooth (one dip), suggesting the droplets are spherically symmetric. However, the *i* phase cut along the OW interface of the 20 μm droplet, shown in Fig. 4.7, has a non-constant phase curvature. The larger droplet has less surface tension, so has not formed a smooth hemisphere. The phase shows two dips along the OW interface instead of one as is seen for a spherically symmetric oil droplet. Looking at the *ii* cut it is possible to see approximately two epi-reflected fCARS signals (two peaks) within the GO interface signal, instead of the one peak seen in the smaller droplets. There are interference fringes along the GO interface, which can be attributed to the variation in the refocussing of the epi-reflected fCARS signal from the variance in the OW surface shape. Due to the less concave OW surface, the epi-reflected fCARS signal propagates less below the GO interface, *iii* cut barely shows any reflected signal for the 20 μm droplet.

There is a phase step, related to the phase of the complex $\chi^{(3)}$, of $\approx \pi/2$ between the eHCARS signal at the GO and GW interfaces. This arises from the fact that CARS signal in the oil is dominated by the resonant response, giving a large $\mathrm{Im}\{\chi^{(3)}\}$, whilst the GW is mostly dominated by a non-resonant response resulting in mostly $\mathrm{Re}\{\chi^{(3)}\}$. The relative phase between the real and imaginary responses then are expected to be $\approx \pi/2$, as measured.

4.3 eHCARS: Spectral dependence of the interface signal

Because of the resonant nature of the eHCARS signal from the droplets, a spectral dependence was performed to investigate the spectral behaviour of the complex signal. It is expected that the amplitude of the eHCARS signal from the GO interface follows a dependence similar to the intensity of the SRS spectrum measured in Fig. 4.3, since they are both dominated by resonant contribution by the $\mathrm{Im}\{\chi^{(3)}_{oil}\}$. The GW and OW contribution is expected to increase as the spectra approaches the OH stretch at 3200 cm^{-1}. To calculate the spectral dependence of the interfaces, two dimensional xz eHCARS measurements of a single, $\approx$15 μm diameter, oil droplet were repeated for a range of IFD frequencies from 2800 cm^{-1} to 3100 cm^{-1}, in steps of 20 cm^{-1}. The 60x, 1.27NA, water immersion objective and 1.5x tube lens were used. The images were created by raster scanning using the LP200nanostage. The sample was scanned for 1ms per pixel with a pixel size in x of 0.11 μm, and 10 nm per pixel in z. The horizontal (co-polarised) component of the eHCARS amplitude and phase (encoded into Value-hue similar to Fig. 4.3) measurements at 2800 cm^{-1}, 2900 cm^{-1}, and 2940 cm^{-1} are shown at the bottom of Fig. 4.9. A small range of pixels along the x direction were averaged for each interface type and are shown

for three different IFD's in Fig. 4.9; GO along the top, GW middle and OW at the bottom. The z cuts are plotted above the eHCARS xz images, their origin is labelled by the corresponding coloured dashed line. The OW z cuts were averaged over 5 z positions (5 columns of pixels in the image average to 1) where the curvature of the top interface was negligible; if averaging over too large of an x range, there would be an axial broadening to the OW interface peak by the curvature. The GO and GW z cuts were averaged over 10 x positions, centred at the corresponding dashed lines, making sure not to contain any contribution from neighbouring interfaces. The amplitude of the cuts were then noise corrected by

$$A'' = \sqrt{|A'^2 - \sigma^2|}.\text{sign}(A'^2 - \sigma^2) \tag{4.2}$$

where A'' is the corrected amplitude, A' is the averaged z cut, and σ is the noise.

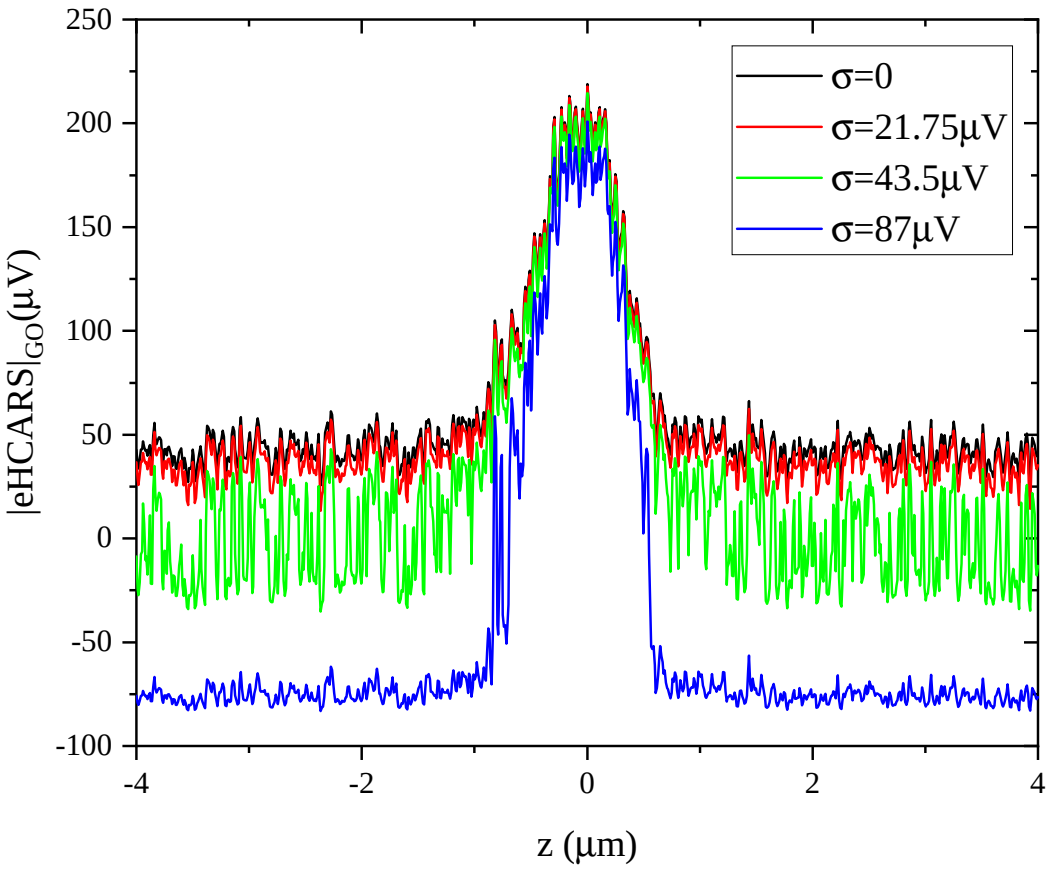

Figure 4.8: Amplitude noise correction to an eHCARS amplitude signal from a GO interface for various noise values.

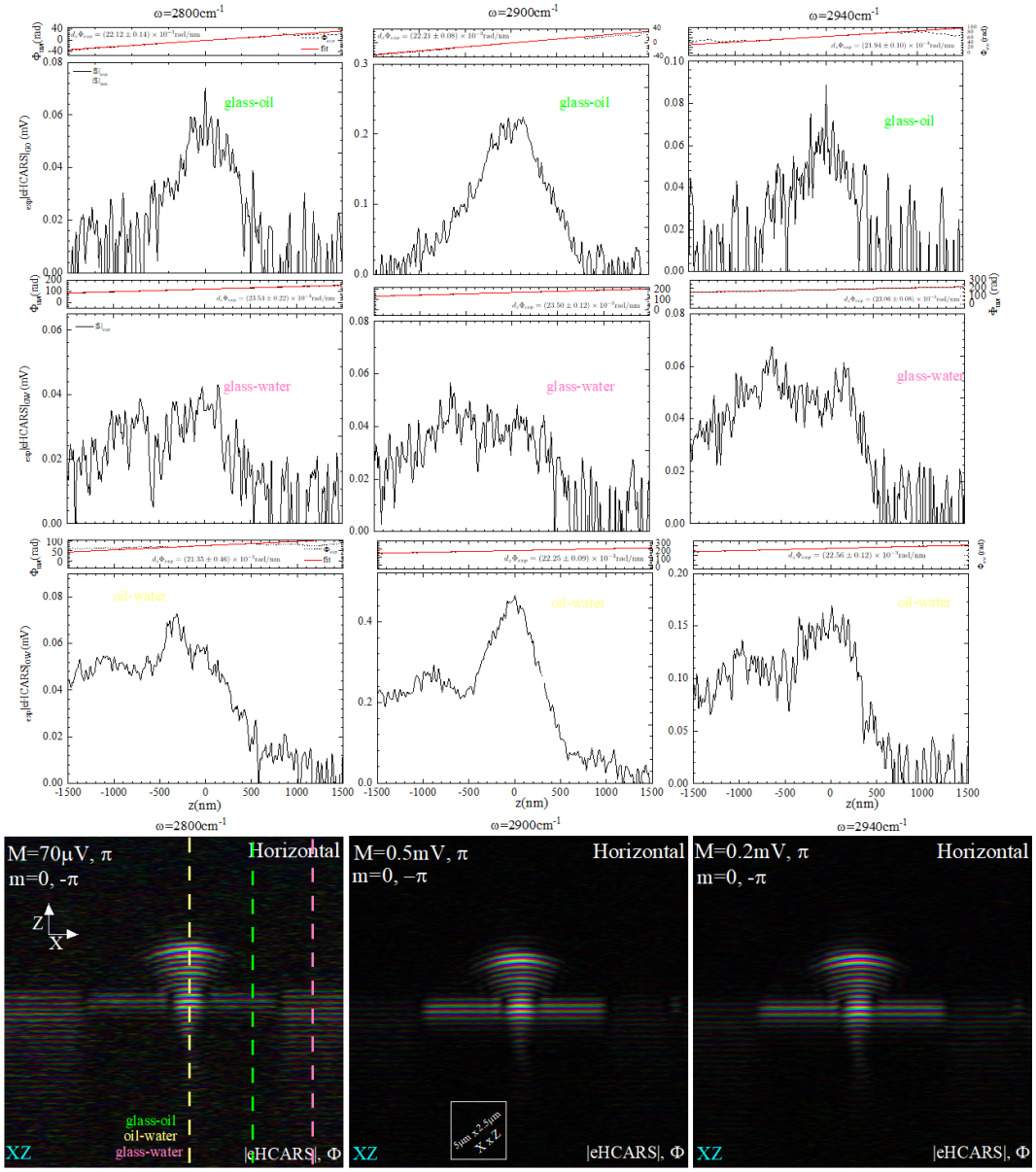

Figure 4.9: Top, middle, bottom row of z cuts: eHCARS amplitude z cut through the GO, GW and OW interfaces measured at 2800 cm^{-1}, 2900 cm^{-1}, and 2940 cm^{-1}. Above each eHCARS amplitude z cut is the corresponding unwrapped phase and calculated slope across the interfaces. Below the z cuts are the xz encoded amplitude and phase eHCARS images indicating where the cuts were taken from for each interface type (Value-hue scale similar to Fig. 4.3).

From both the xz images and z cuts it is possible to see that there is a spectral dependence in the GO interface signal. At resonance, 2900 cm^{-1}, the GO signal is ≈4x larger than the off resonant cases. The xz images display very similar signal generation pathways, to the previously reported xz images. Each interface response has a typical full width half maximum of ≈1 μm, which relates to the z sectioning of the eHCARS technique, from the non-linearity of the CARS generation and the confocal selection. The axial width of the interfaces is also related to the collection efficiency of the objective, higher NA objectives are capable of detecting more non-normal incidence epi-signal. For the GO, the width is given only by the region where

epi-CARS is generated as there is no step in the $\chi^{(1)}$. The axial width of the signal in the GW z cuts are much wider then the GO z cuts, extending 1.5 μm+ into the glass, and is a result of the epi-reflection of fCARS generated in the glass due to a step in $\chi^{(1)}$. The unwrapped phase is plotted above the corresponding measured amplitude in each trace, Fig. 4.9. The unwrapped phase is then fitted with a linear function to extract the phase slope, giving a typical value of 22 rad/nm. The phase slope can be used to calculate height differences and provides a topographical sensitivity.

In this chapter the

Chapter 5

LFE eHcCARS

In this chapter the local field enhancement (LFE) provided by metallic gold nanoparticles (NPs) to the CARS signal, E_{CARS}, generated in the vicinity is explored, specifically in eHCARS. The collective oscillations of conduction band free electrons, driven by an incident electro magnetic field (E-field) and restored by the induced lattice charge, has a specific resonant frequency determined by the NPs geometry and is called the local surface plasmon resonance (LSPR), see Sec. 2.2.1. For LFE-CARS measurements the LSPR of a NP is chosen such that the resonance overlaps with the frequency of the emitted CARS field. The driven polarisation on the NP generates a confined, enhanced field on the surface and near the NP, which is amplified compared to the fields outside the NP. Objects near or in contact with the surface of the NP, within the enhanced field, will also have their CARS signal enhanced. Surface enhanced Raman scattering (SERS) has opened the possibilities of single bio-molecule detection [71, 72] with numerous possible bio-applications[110]. Typically, values in the range of x10 to x100 enhancement to the signal intensity are observed experimentally [74, 111], with SE-CARS experiments having x10 the enhancement that would be seen in SERS experiments [112]. Larger (>100 nm) NPs are traditionally used, they are more photo-stable, and provide larger enhancements but allow for less spatial resolution in the detection compared to smaller NP's. Specifically, gold nanorods (NRs) were chosen for LFE-CARS because of the higher optical cross section (compared to nano-spheres) of their longitudinal mode, and field focussing at their tips, providing greater enhancement [113]. Gold is also considered to be biologically inert, and widely used for bio-application [87, 114], having no effect on the surrounding biological environment. Although more recently there might be evidence to suggest that gold NPs contribute to biochemical changes in human cells [115].

In practice utilising the enhancement to the optical fields by small NPs is very difficult, especially in CARS. This is because metallic NPs generate their own multi-photon fluorescence and four-wave mixing (FWM) background, and are relatively sensitive to photodamage by strong E-fields [116, 117]. eHCARS is a dual polarisation heterodyne resonant detection, therefore the fluorescent background signal, usually associated with NRs, will be separated. The instantaneous FWM background is separated by appropriate time-gating of the reference pulse. Additionally to providing an enhancement of the signal, NRs are a sub-diffraction limited volume, allowing for the chemically specific sensing of objects down to the order of the NRs size (20 nm to 30 nm). NRs are small enough to be internalised by cells and traffic

inside. The eventual goal, beyond the scope of this work, is to utilise the enhancement from NR's to detect specific nanoscale lipid and protein components, such as nanodomains and lipid rafts, in lipid bilayers.

In this section SE-eHCARS measurements of uncoated bare gold nanorods (BNRs), silica coated gold nanorods (SNRs) and an array of gold rod dimers produced by focused ion beam lithography (FIB dimers) are shown. The aim was to optimise the experimental technique and nanoparticle selection such that a stable local field enhancement could be exploited for repeated eHCARS measurements. Where possible single particle extinction spectroscopy was performed to characterise the nanoparticles shape before performing the eHCARS measurement.

5.1 Bare gold Nanorods

The bare gold NRs (bNRs), uncoated (no shell) gold rods with CTAB, were purchased from Nanopartz have a longitudinal LSPR of 605 nm and transverse LSPR of 518 nm in water, with an aspect ratio (AR) of 2.3 (L×W=57 nm×25 nm). The aspect ratio of the bNR can be tuned to give a specific longitudinal LSPR λ over a large range during the synthesis, from 550 nm upwards. The transverse peak remains at between 500 nm and 530 nm for different aspect ratios of bNRs. Specifically, the AR=2.3 bNRs were chosen as their LSPR in oil would be shifted, compared to in water, by ≈+50 nm. This places the longitudinal LSPR of the bNR close to the wavelength of the CARS field, when tuned to an IFD (ω) range from 2800 cm^{-1} to 3100 cm^{-1}. Silicone oil was used as a proof of principle system as it has a strong resonance at 2904 cm^{-1}. For 2800 cm^{-1}, λ_{CARS}=666.88 nm, and at 3100 cm^{-1}, λ_{CARS}=653.80 nm, see Fig. 3.13 for pump and Stokes wavelength calibration. λ_{CARS} was chosen to overlap with the LSPR of the bNR to maximise the enhancement of the generated signal and to reduce heating, and reshaping, due to overlap with λ_p and λ_s.

bNRs with LSPR of 600 nm were covalently bound by sedimentation to a hydrogen peroxide cleaned glass coverslip functionalised with 3MT. The coverslip and slide was then squeezed together, with silicone oil between, to push any dielectric debris in the oil, or on the slide interface, closer axially to the bNRs on the coverslip. Squeezing the sample pushes debris closer to the same focus as the rods, making them easier to detect and distinguish, as well as minimising out of focus shadowing when observing the sample in bright field transmission imaging. See Sec. 3.1.3 for sample preparation details. The resultant sample provides a flat glass substrate with covalently bound bNRs immersed in silicone oil, see Fig. 3.8. The bNRs have to be fixed, by covalent binding, to the glass, ensuring the strong excitation fields do not optically trap and move the bNR during the raster scan. Covalently binding also prevents any diffusion of the bNRs over time.

5.1.1 Extinction characterisation

Characterisation of the bNRs geometrical shape can be performed by either wide-field extinction imaging or single particle extinction spectroscopy in our setup, see

Sec. 3.2.3, utilising a technique described in detail by Payne *et al* [106, 107, 108]. In this case, wide-field extinction is used as a tool for visualising the polarisation behaviour before measuring the extinction spectrum for a single particle, and then eHCARS. This check ensures that the particles being selected for imaging exhibit a strong polarisation behaviour, confirming that the object of interest is a rod. It is well known that colloid solutions of NRs have an aspect ratio heterogeneity, with some being close to spherical.

Fig. 5.2 shows a series of extinction images, $\Delta_{\pm}$, taken at linear illumination polarisation angles (θ) 0°, 30°, 60°, 90°, 120°, and 150°, of the bNRs in silicone oil. The $\Delta_{\pm}$ image contains a bright Δ_{+} and dark Δ_{-}, corresponding to the shifted reference, see Sec. 3.2.3. Particle 1, 2 and 3 are labelled, and were selected due to their strong θ dependence and spacial separation from neighbouring bNRs for single particle extinction spectroscopy. What is meant by this is that the intensity of the (bright) Δ_{+} spot is modulated whilst rotating through θ (the inverse occurs to the Δ_{-}). The absolute value of θ when $\Delta+$ is maximised corresponds to the relative orientation of the bNRs longitudinal extinction cross section, σ_{-}, in space, see Fig. 5.1.

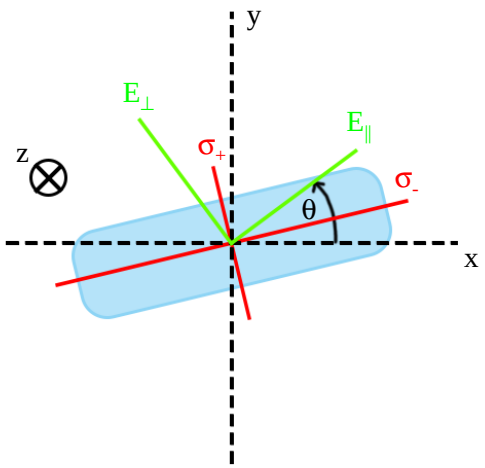

Figure 5.1: Sketch of the bNR with longitudinal(transverse) extinction cross section labelled with σ_{-} (σ_{+}). Orthoganal linear polarisations in the xy plane are shown. θ is the angle of rotation relative to the x axis of the linear polarisation.

Visually in the $\Delta_{\pm}$ image it is possible to see that the maximisation (minimisation) of Δ_{+}, varies between the six particles labelled, corresponding to a different orientation in space. Here we predominantly visualise the σ_{-}, (extinction of the long axis), being maximised when the polarisation angle, θ, is parallel to the orientation of this mode. The minimisation of the σ_{-} occurs when θ is rotated such that the linear polarisation is orthogonal to the σ_{-} mode, parallel to the transverse extinction mode, σ_{+}. It is measured in later spectroscopy measurements that the σ_{-} is typically x10 larger than the σ_{+}. For this reason, we visualise a coupling to the σ_{+} as a minimisation of the extinction (when θ is aligned with σ_{+}). The bNR labelled * doesn't have a strong dependence of it's Δ_{+} when changing θ, suggesting that it is more spherically shaped than the other six bNRs labelled.

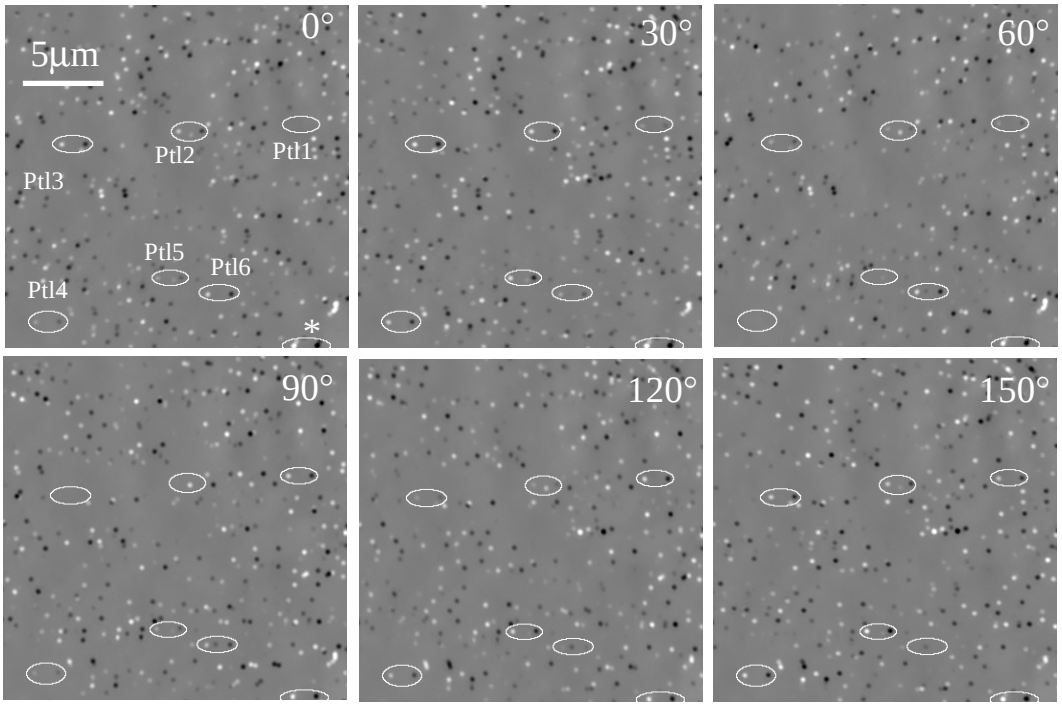

Figure 5.2: Wide-field extinction image, using 650 nm filter in the illumination, $\Delta_{\pm}$, of bNRs on a glass substrate using the 100x 1.45NA objective, x128averages, N=10 repeats, S=1.6 μm. Gray scale white(black) maximum(minimum) is 0.15(-0.15). A 5μm scale bar is shown, and the polarisation angle is noted in the top right of each image. Particles 1, 2, and 3 are indicated, they were selected for single particle extinction spectroscopy in Fig. 5.3.

As mentioned, from Fig. 5.2, particles 1, 2, and 3 were chosen for a more quantitative analysis performed with the spectroscopic single particle extinction technique. Instead of detecting the transmitted light in a camera to produce a wide-field image of many bNRs, the transmission from a single bNR is sent to a spectrometer. A shifted reference is then used to produce the normalised transmission (same as for wide-field extinction), from there, the extinction cross-section as a function of the illumination wavelength, σ, can be calculated, see Sec. 3.2.3. Spectroscopy results are shown for particles 1, 2 and 3 in Fig. 5.3, with the σ_+ and σ_- values plotted as a function of θ alongside. The location where the values for σ_+ and σ_- were obtained is shown in the spectrum by a colour coded, vertical, dashed line. σ_+ and σ_- values were determined spectrally with the knowledge that there should be two σ peaks corresponding to along and across the rods, with the largest σ arising from the longitudinal mode. Below the spectroscopy results in Fig. 5.2 the $\Delta_{\pm}$ of the corresponding bNRs are shown for each θ, S=1.6 μm between Δ_+ and Δ_-. The σ as a function of θ at both longitudinal (σ_-) and transverse (σ_+) modes was obtained from the spectrum of each particle and fitted using

$$\sigma(\theta) = \sigma_A(1 + \alpha\cos(2(\theta - \theta_0))) \tag{5.1}$$

where σ_{A} is the average σ over all θ, α is the amplitude of the polarisation dependence, and θ_0 is an angular offset. $\sigma(\theta)$ with an $\alpha \to 0$ have a small θ dependence, expected for a spherical shape.

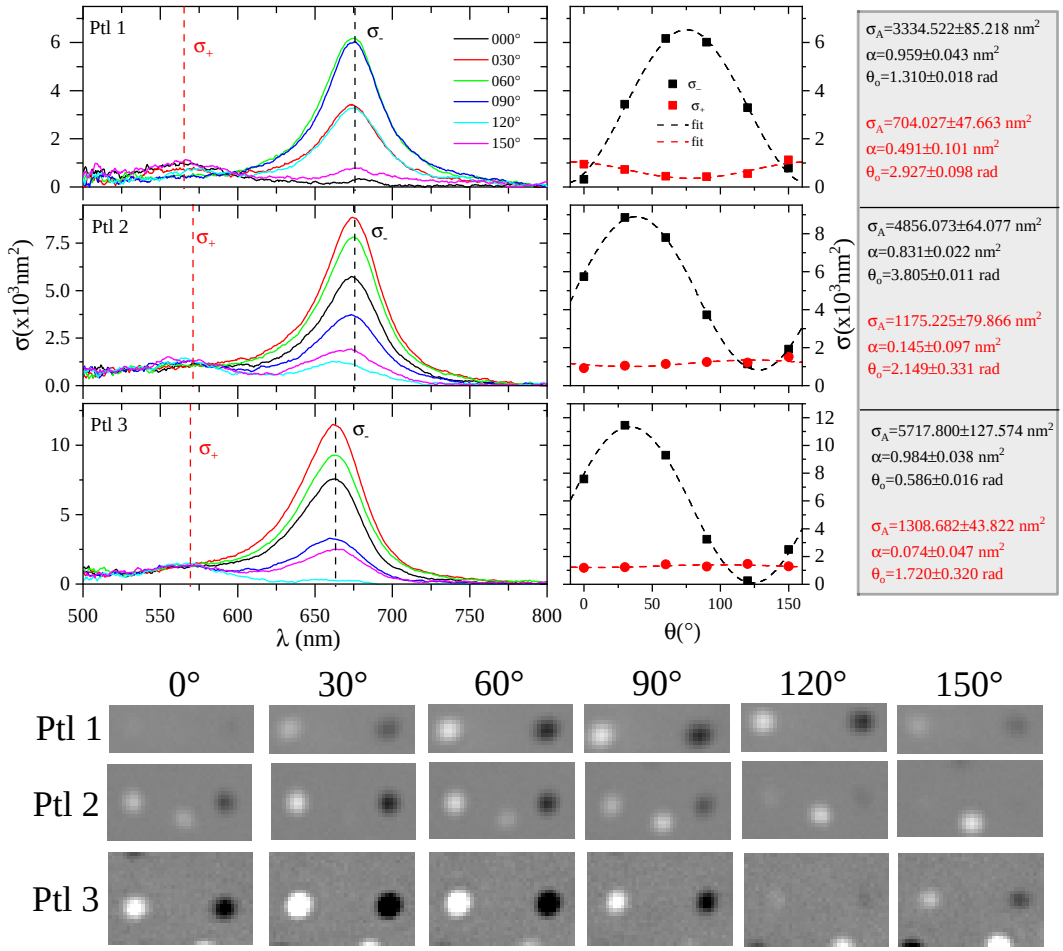

Figure 5.3: Top: Single particle extinction spectrum. 200 acquisitions, 11 ms exposure, 100lines/mm grating, and input slip opening of 80 μm. 2×5 (spectrum×position) binning of the Andor CCD was used. Bottom: Wide-field polarisation angle θ resolved extinction images ($\Delta_{\pm}$) of three different bNR's that were subsequently measured with eHCARS. Shift S=1.6 μm between Δ_+ Δ_-, x128 averages repeated 10 times at each position, using 20 ms exposure, were recorded by the sCMOS PCO throught the 100x 1.45NA objective. The grey scale white(black) maximum(minimum) is 0.15(-0.15).

Looking at the single particle extinction spectrum for particle 1 in Fig. 5.3, it shows a strong rod-like behaviour in the σ_- peak at 670 nm, with α=0.959, and $\sigma_{+,A}$=3334.5 nm^2. We see a peak σ_- at θ=74.5 °, correlating with the maximum $\Delta+$ observed between the 60°and 90°measurement in the $\Delta_{\pm}$ images below. There is a small peak in the spectum at 555 nm corresponding to the transverse extinction cross-section, σ_+, with α=0.49 and σ_A=704.1 nm^2. It's expected that the σ_+ has a reduced polarisation dependence, smaller α, and a lower overall σ_A. This is because more energy is required to induce a polarisation along the smaller axis as the induced polarisation along that axis will be smaller. Similarly Particle 2 and 3 both show a strong rod-like behaviour in their σ_- peaks, with α=0.83 and α=0.98 respectively. By comparing the $\sigma(\theta)$ for σ_- with the $\Delta_{\pm}$ images, it is possible to deduce that particle 2 and 3 is maximised at 33°and 37°respectively.

5.1.2 eHCARS of bare gold nanorods

eHCARS meaurements, were performed on the bNRs discussed in Sec. 5.1.1 to study the enhancement to the CARS signal in their vicinity. The IFD was tuned to ω=2904 cm^{-1}, by setting λ_P=820 nm and λ_S=1076.29 nm providing a λ_{CARS} =662.29 nm, as shown in Fig. 3.13. From the extinction measurements in Fig. 5.3, we can see that there is a good overlap of the LSPR wavelength of the longitudinal mode with the CARS wavelength. For the greatest enhancement effect, the CARS field E_{CARS} polarisation should be aligned with the long axis of the rod. It is possible to do so using a $\lambda/2$ plate, mounted into the objective waveplate, to rotate the polarisation of the excitation to the orientation of the rod. However, in practice this is very difficult to do as the exact orientation in space of the rod must be known. It is possible to scan the rod with eHCARS whilst rotating the $\lambda/2$ plate to find the peak signal, but in practice this causes the rod to be exposed to the laser intensity for a duration before continuing with the desired measurement. Ideally, the lasers dwell time on the particle should be minimised to prevent damage. What is done instead, is a $\lambda/4$ polariser is inserted into the objective waveplate, to provide circularly polarised light. Doing so means that the E_{CARS} is coupling to both axis of the rod simultaneously, so there is no polarisation alignment necessary.

Inserting a $\lambda/4$ into the objective waveplate means that the polarisation is not only altered in excitation, but also in the epi-detection; the signal is detected through the same objective used in excitation. The E_P, E_S and E_{ref} are all polarised in the horizontal direction (H). Horizontally polarised light is passed through the objective, becoming circularly polarised when incident on the sample. It is expected that circularly polarised light reflecting of a perfect planar surface will flip helicity. The CARS process forms a perfect interface in bulk medium, there are no further symmetries broken therefore we expect the CARS signal to have this polarisation behaviour. For the reason mentioned, the glass-oil interface signal the incident circularly polarised light generates a CARS signal that has a reversed helicity compared to the excitation. The reversed helicity signal then passes through the $\lambda/4$ in epi-detection producing a vertically (V) polarised signal. The $\lambda/4$ plate is adjusted in the eHCARS measurements to follow by maximising the interface signal in the vertical polarisation. When a NR is placed on the glass-oil interface the circularly polarised light excites the dominant longitudinal mode of the rod generating linearly polarised light, matched to the orientation of the long axis of the rod (co-rod polarisation). This co-rod polarised light is then converted back into a circular polarisation in epi-detection through the $\lambda/4$. The signal finally interferes with the 45 °linearly polarised reference and detected with an equal contribution to both H and V components. Therefore from a rod generating perfect linearly polarised signal, there should be an equal signal seen in both H and V components. As stated above, if light is reflected by the sample and remains circularly polarised, it will only be detected in the vertical polarisation component in this set up. It is expected that the signal from spherical NPs will be detected only in the vertical polarisation component, as they are not introducing any preferential axis in the LSPR, and thus do not break the symmetry of the incident polarisation.

The eHCARS setup detects the CARS field in amplitude and phase, hence as a complex quantity. Therefore the enhancement to the silicone oil signal by the rod, S_{ce}, is calculated by normalising the complex signal at the rod, S_{nr}, with the

complex signal in the oil nearby, S_{o}, as follows

$$\text{Vertical component: } S_{\mathrm{ce,V}} = \frac{|S_{\mathrm{nr,V}} - S_{\mathrm{o,V}}|}{|S_{\mathrm{o}}|} \tag{5.2}$$

$$\text{Horizontal component: } S_{\mathrm{ce,H}} = \frac{|S_{\mathrm{nr,H}}|}{|S_{\mathrm{o,V}}|} \tag{5.3}$$

The $\mathrm{Re}\{S_{\mathrm{o}}\}$ and $\mathrm{Im}\{S_{\mathrm{o}}\}$ parts of S_{o} are obtained at a region spatially separated but as close as possible to the spatial location (taking into account the PSF in the setup) NR in the same measurement. These values are then used as an offset and subtracted from the signal at the NR (see nominator in Eq. 5.2). The denominator in Eq. 5.2 uses the vertical component of the $|S_{\mathrm{o}}|$ (amplitude), as all interface signal is measured in the vertical component. Here it should be noted that the normalisation to the CARS from silicone oil measured outside the NR is done so over the entire PSF, whilst the enhancement is generated from a region much smaller than the PSF. This means that the values for S_{sc} in this way are an under estimation of the actual local-field enhancement on the surface of the NR. For this reason the enhancement is quoted in units of silicone oil in the measurements shown.

EHCARS measurements taken in the xy plane, at the glass-oil interface, showing the enhancement from bNRs are shown in Fig. 5.4. Here are four repeated measurements of the same bNR, taken sequentially using a laser power entering the objective equating to $\mathrm{P_P P_S}^{1/2}$=0.55mW$^{3/2}$. A 2 μm×2 μm xy raster scan was performed in 81x81 pixels with an IFD of ω=2904cm^{-1}. In the right column in Fig. 5.4 the eHCARS amplitude, |S|, and phase ϕ images, normalised to the silicone oil signal by Eq. 5.2 and Eq. 5.3, are shown, for a 1 μm×1 μm region of the total scan size. Both the horizontal (H) and vertical (V) components of the detected polarisation is shown. Corresponding to the xy images in the same row, on the right, are y cuts taken through the centre of the bNR's signal; along the fast scanning axis of the raster scan to minimise noise due to drift. The y cut location is marked with a dotted red line in the amplitude images. The cuts show the amplitude of the signal normalised to the silicone oil signal outside the rod (|eHCARS|). For the normalisation, the silicon oil amplitude spatially separated from the NR has been averaged over a spatial region to minimise noise. The amplitude of the signal from the silicone oil for the chosen power values is close to the noise level in this case, therefore careful averaging as described and extrapolation from Fig. 3.15 was required to optimise the normalisation.

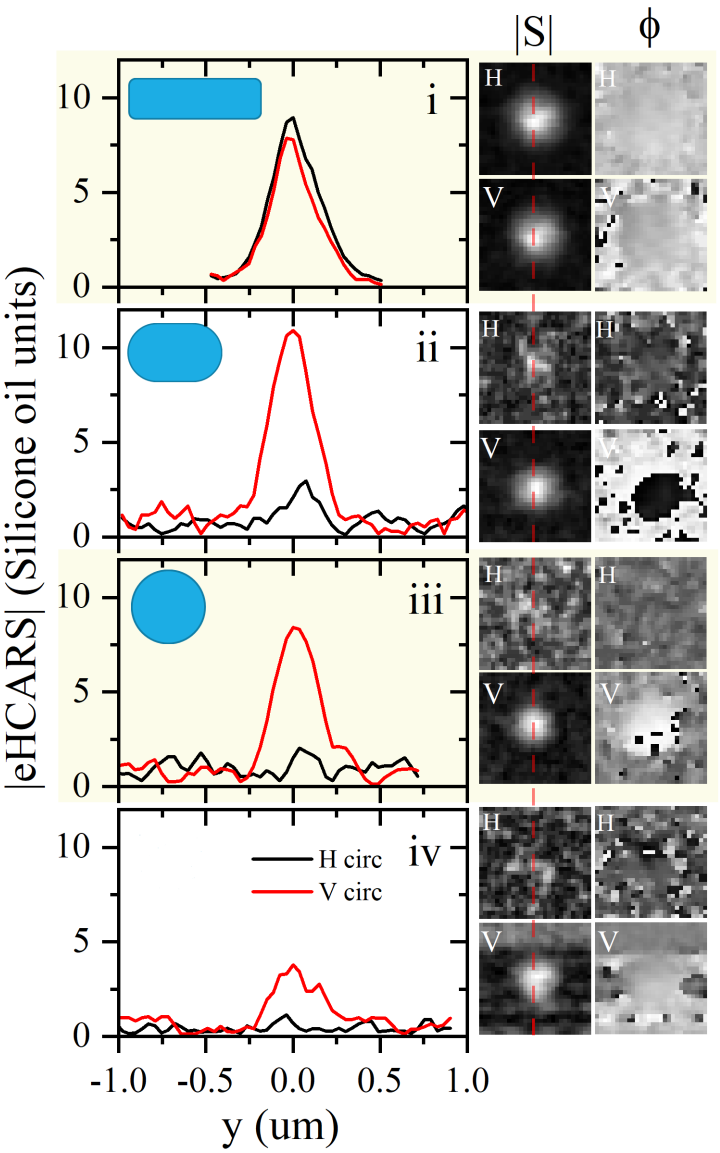

Figure 5.4: Four repetitions (*i* to *iv*) of a eHCARS measurements on a plane containing a bNR, with $P_P P_S^{1/2}$=0.55mW$^{3/2}$. 2 μm×2 μm rastercans with 1 ms dwell time over 80×80 pixels, at the glass-oil interface centred at the bNR. Right column: Amplitude ($|S|$) and phase (ϕ) in both H and V polarisation component images, cropped to 1 μm×1 μm from the measurement. Left column: EHCARS amplitude H and V polarisation y cuts through the centre of the bNRs, as indicated by a red dashed line in the images, normalised the the signal from the silicone. A blue block sketch indicates the hypothesised shape of the rod during the repetition, by the *iv* repetition the rod is assumed to be completely spherical as there is reduced enhancement and no horizontal component.

The first repetition, *i*, shows an ×8 enhancement of the silicone oil signal at the bNR in both the H and V components. The second repetition, *ii*, was measured instantly after *i*, and has a very different signal characteristic. Here there is a large enhancement seen in the V component of around ×13, but a much lower enhancement in the H component of ×3. By the *iii* repetition the bNR signal in the H component is nearly zero, and by the *iv* repetition the V component of the bNR enhancement has reduced significantly to ×3.5. There is a significant change to the

enhancement from the bNR with repeated measurements. The reduction in the H component of the signal suggests that the signal is becoming less linearly polarised, due to the detection through a $\lambda/4$. Combined with the overall reduction of the enhancement, this would imply that the excitation is reshaping the bNR to a more spherical shape. It is expected that the signal from a sphere in this detection scheme would be only seen in the vertical component. The hypothesised sketch of the reshaping of the bNR has been inserted to each y cut measurement in Fig. 5.4. The suggestion here that upon pulsed laser excitation, a rod reshape into a more spherical shape is consistent with Gonzalez *et al*'s observations with high resolution transmission electron microscopy [118]. Based on the signal characteristics discussed, it can be suggested that the bNR is progressively becoming more spherical after each scan.

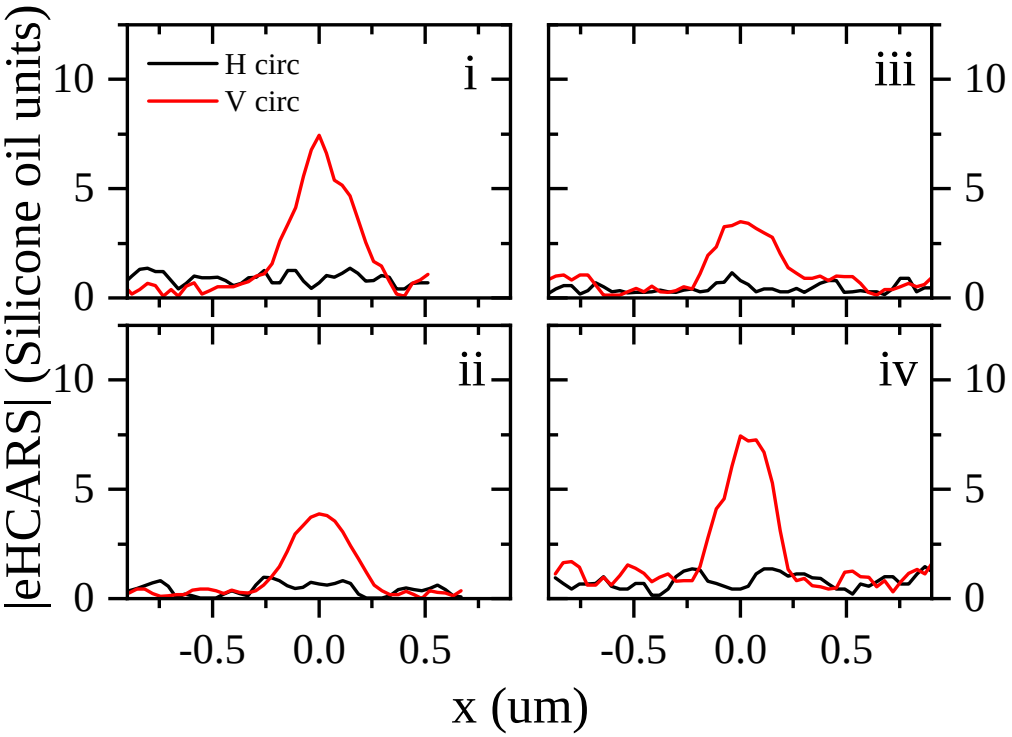

Figure 5.5: eHCARS measurements with $P_P P_S{}^{1/2}$=0.55mW$^{3/2}$ of four different bNRs labelled i to iv. Both eHCARS H and V polarisation y cuts through the centre of the bNRs are shown, normalised the the signal from the silicone (see Fig. 5.4 for clarification of the y cut).

The case for most measurements taken on the bNR was that even on the first scan there would be a considerable amount of reshaping to the bNR. Shown in Fig. 5.5, are |eHCARS| y cuts from four different bNRs, measured with the same parameters used in Fig. 5.4. These four bNRs were measured only once, and already have a reduced H component to the eHCARS signal at the rod, suggesting that they were reshaped instantly by the measurement.

The measurements shown in Fig. 5.4 and Fig. 5.5 were taken utilising an excitation power that had been determined to be a compromise between reshaping and signal strength, by performing a power dependent study as described in the following.

Initially, the power dependence of a bNR was taken in what will be called the 'high-power' regime of $P_P P_S{}^{1/2}$>5mW$^{3/2}$. Upon realisation that this was power was too high, the 'low power' regime of $P_P P_S{}^{1/2}$<1mW$^{3/2}$ was measured for a different bNR. To obtain the enhancement value at each selected power an xy scan was done at the glass-oil interface centred at the bNR, and y cuts were then taken from the 2D image. The peak value of the enhancement was then obtained from the y cuts. Single particle extinction spectroscopy was not possible to obtain post power dependence due to the destruction of gold nanorods or scorching of oil in the vicinity. The enhancement reported in Fig. 5.6 case was projected from the circular polarisation to the linear components parallel to the rod orientation using a Jones matrix formalism. The following equation was used

$$S_{\mathrm{co}} = \frac{S_{\mathrm{p}} + \sigma_{S_{\mathrm{p}}} + e^{i\phi} S_{\mathrm{m}} + e^{i\phi} \sigma_{S_{\mathrm{m}}}}{\sqrt{2}} \tag{5.4}$$

to calculate the co-rod component. S_{p} is the V circularly polarised signal, and S_{m} is the H polarised signal. $\sigma_{S_{\mathrm{p}}}$ and $\sigma_{S_{\mathrm{m}}}$ are the corresponding offsets and ϕ is the relative phase of the rod signal between the H and V polarisation components. The amplitude along the long axis of the rod, |co-rod|, is shown for both high and low-power regimes in Fig. 5.6. Below the amplitude enhancement is the two-photon fluorescence (TPF) measured from the rod simultaneously; collected in the forward PMT, see Sec. 3.2.4.

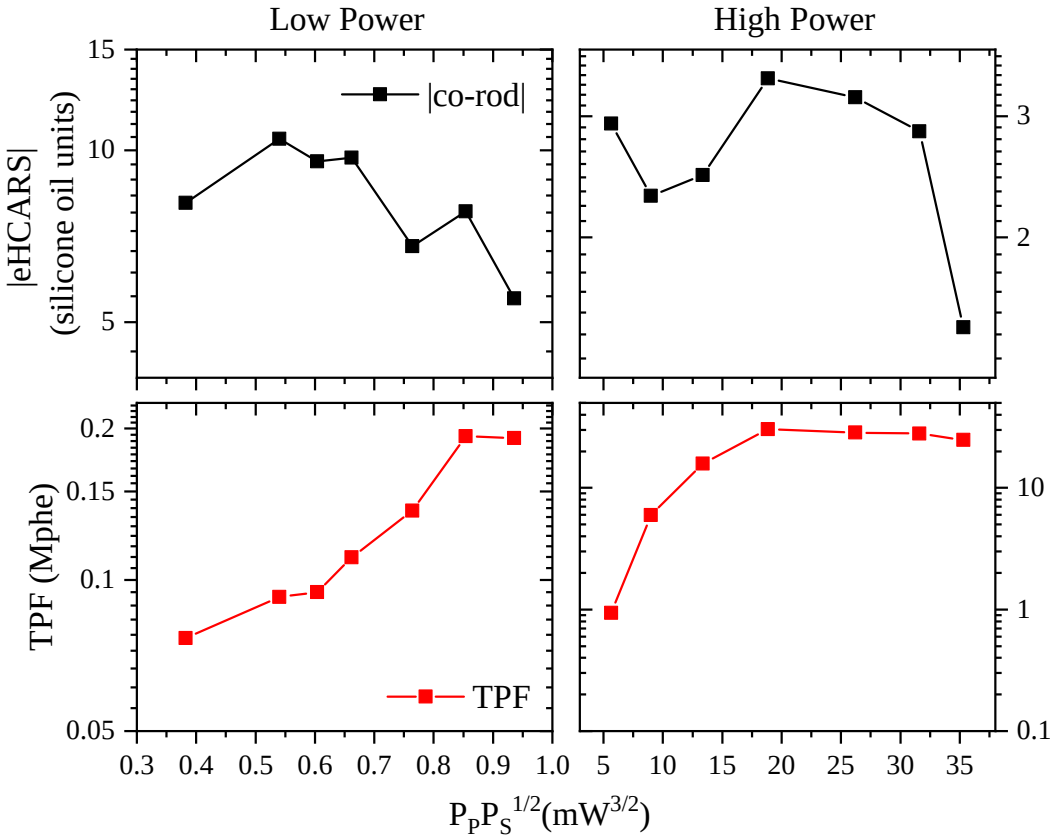

Figure 5.6: EHCARS amplitude (projected to the co-linearly polarisation along the bNR) and TPF power dependence of the signal from two bNRs. One bNR measured in the low power regime, and another in the high power regime. Measurements were performed in the same manner as Fig. 5.4, and the peak signal at the bNR is extracted from the 2D images, and plotted as a function of excitation power.

In the high-power regime, Fig. 5.6 right column, we see that the enhancement is already at a low value of around $\times 3$, suggesting that this particle has already been reshaped at these excitation powers. At $P_P P_S^{1/2}$=35mW$^{3/2}$ the eHCARS signal from the bNR disappears, but there remains TPF signal suggesting that there has been a total reshaping of the particle, but not total particle destruction as there is still some fluorescence and the PSF was reasonably shaped. In the lower power regime, Fig. 5.6 left column, there is a relatively stable $\times 10$ enhancement seen between $P_P P_S^{1/2}$=0.5 and 0.6mW$^{3/2}$. Above this power the enhancement of the longitudinal mode begins to fall, suggesting that there is some reshaping beginning to happen. A lower power seemed to yield a lower enhancement, this has no physical explanation other than the measurement at low power incorporating more of an error during the normalisation.

It should be noted that the low-power dependence on the bNR was performed on a rod that displayed a stable signal throughout the repetitions. At the lower-power regime the particle survived four exposures increasing in power before displaying considerable reshaping. The stable characteristics of this particle measured in the low-power dependence is not a reflection of the ensemble behaviour, with the majority of particles measured behaving in a similar manner to the measurements shown in Fig. 5.5. However, shown in Fig. 5.7, are four repetitions of an xy scan, with a

power of $P_P P_S^{1/2}$=0.55mWmW$^{3/2}$, showing a more stable behaviour; not indicative of the ensemble behaviour of the sample. The measurement shown is set up in exactly the same way as shown for previous xy data sets.

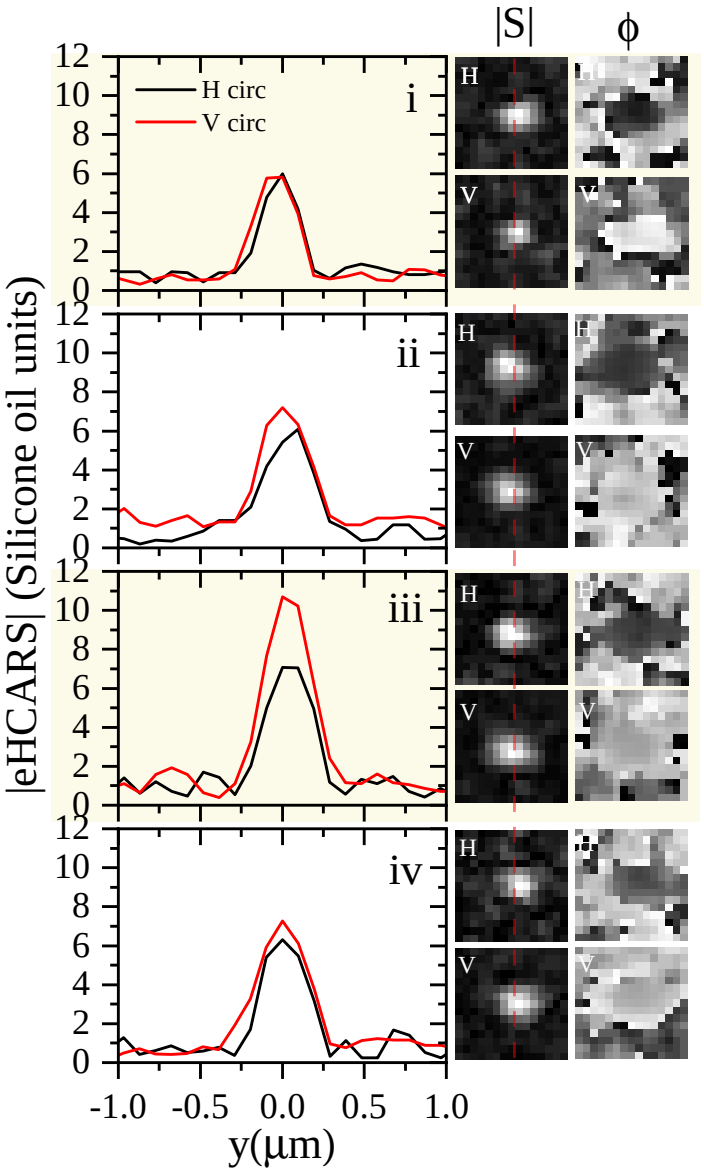

Figure 5.7: Four simultaneous repetitions (i to iv) eHCARS measurements of a bNR, with $P_P P_S^{1/2}$=0.55mW$^{3/2}$. 2 μm×2 μm rastercans with 1 ms dwell time over 80×80 pixels, at the glass-oil interface centred at the bNR. Right column: Amplitude ($|S|$) and phase (ϕ) in both H and V polarisation component images, cropped to 1 μm×1 μm from the measurement. Left column: EHCARS amplitude H and V polarisation y cuts through the centre of the bNR's, as indicated by a red dashed line in the images, normalised the the signal from the silicone.

The enhancement in this case is slightly lower, only ×6, in the H component throughout all repetitions. There is a significant spike in enhancement, to ×11, seen in the V component of the *iii* repetition, which could be explained by a temporary bulging in the centre of the rod. This would lead to a larger spherical shaped volume

in the middle of the structure. With the increased size of the spherical shape the free-electrons could be free to move in more directions at lower energies, leading to more un-polarised light emission. The intermediate 'bulging' along the long axis outward in the short axis after a irradiation with a femtosecond laser pulse has been observed by TEM images [118]. On the other hand, a more spherical shape could provide less enhancement both geometrically and from the LSPR, but with the blue shift in LSPR an increased enhancement could be seen, suggesting that the rod is transiently getting more elongated, but supporting a mode that is not perfectly linearly polarised.
The same measurement type used in the power dependence was used to obtain a coarse spectral dependence of the bNRs enhancement to the silicone oil, results are shown in Fig. 5.8. The IFD was tuned in steps of $25\,\mathrm{cm}^{-1}$ from $2850\,\mathrm{cm}^{-1}$ to $2950\,\mathrm{cm}^{-1}$. The overlap of the pump and Stokes was detuned to obtain the specific IFD, by spectral focussing, therefore the delay of the reference had to be optimised for each IFD.

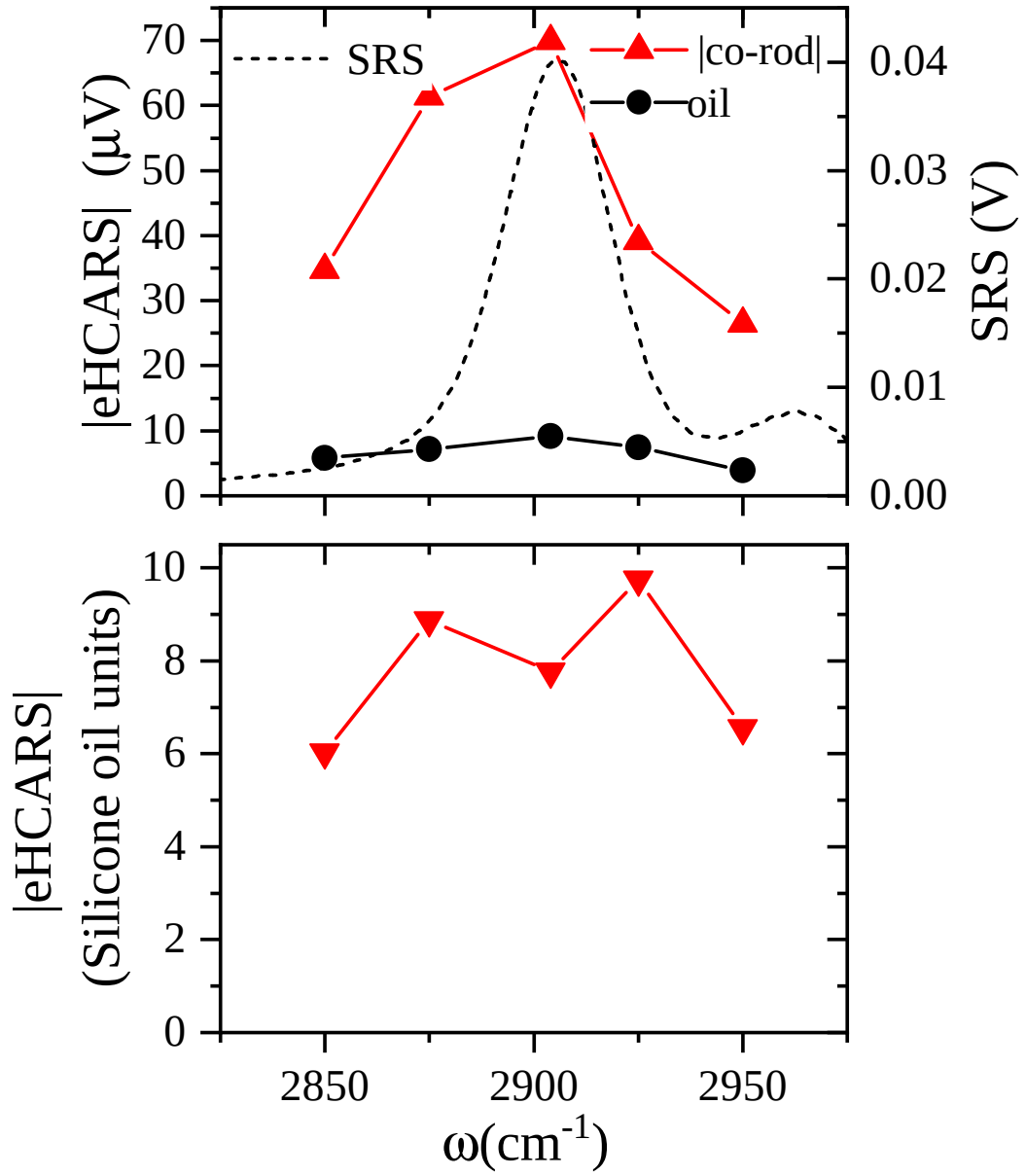

Figure 5.8: The eHCARS amplitude co-linearly polarised along the the rod, and glass-oil signal as a function of IFD is shown in the top plot, overlayed by an SRS's spectrum in the silicone oil to indicate the resonance. Below, the enhancement to the silicone oil eHCARS signal as a functin of IFD is shown, co-linearly polarised along the rod's long axis. Values obtained by performing the 2D imaging shown in Fig. 5.4

By changing the IFD the λ_{CARS} is changed, therefore the resonant condition between the E_{CARS} and the bNR changes. Moving from 2850 cm^{-1} to 2950 cm^{-1} there is a change of -4.36 nm in λ_{CARS} from 664.66 nm to 660.27 nm. Given that the full width half maximum of the σ_- peaks measured in extinction spectroscopy is approximately 50 nm, there should not be a considerable deviation from the resonant condition between E_{CARS} and the LSPR of the bNR. However, there is a significant spectral change in the silicone oil in this range being close to off resonance at 2850 cm^{-1}, see the SRS spectrum in Fig. 5.8. The enhancement measured as a function of the IFD changes slightly, Fig. 5.8 bottom, possibly indicating that

the resonant condition is matched best for a slight shorter wavelength (increased IFD). A change in enhancement is negligible compared with the change seen when repeating measurements on the same rod for the same IFD. The |eHCARS| signal as measured at the bNR and in the oil when changing the IFD is also shown in Fig. 5.8, illustrating the increased signal at the rod compared to the signal in the oil. The resonant behaviour of the |eHCARS| from the silicone oil is also observed in the enhanced silicone oil signal at the rod; matching the resonance at 2904 cm^{-1} in SRS.

5.2 Silica coated gold nanorods

The behaviour discussed in Sec. 5.1, likely due to bNR reshaping is not desired, since there is a reduction to the enhancement, with the signal changing over the course of the measurement, hence a lack of stability and reproducibility of the LFE effect. The ideal scenario is to have a nanostructure providing a stable enhancement during the timescale of a measurement session or longer. A possible solution is to use silica coated nanorods (sNRs) instead of the bare bNRs. The hypothesis is that by introducing a rigid shelling material the reshaping will be restricted by the shell, which keeps the elongated rod shape in place, as a mould, even if the gold is transiently melting. sNRs with a LSPR of 646 nm in water, L×W=71 nm×20 nm with 5 nm SiO_2 shell coated in an amine functional group were used. These sNRs are slightly larger then the bNRs previously measured, which contributes to a larger LFE, to compensate from having a finite distance to the rod surface, and thus a reduction of the enhancement felt by the silicon oil, which is kept 5 nm away from the rod.

The sNRs were covalently bound to a glass cover-slip using tosyl-chloride to functionalise the glass for attachment, they were then immersed in silicone oil, covered with a glass slide and squeezed. The sample structure is identical to that of the previously measured bNRs, see Sec. 3.1.3. To aid with studying the reshaping in more detail, wide-field extinction and extinction spectroscopy were performed before and after performing an eHCARS measurement. Three particles were chosen for eHCARS measurements.

5.2.1 Extinction before

The sNRs were firstly characterised in wide-field extinction, Fig. 5.9, and single-particle extinction spectroscopy, Fig. 5.10, using the same methods used and described in Sec. 5.1.1. For the sNR a 700 nm filter was used to probe the long axis of the sNR in the widefield extinction. From the extinction characterisation particle 2, 3 and 5 were selected for measurement with eHCARS, based on the criteria that they showed a strong polarisation dependence of the σ_- peak. Particles 1 and 4 weren't selected as they seemed to have multiple resonances close together, seen in Fig. 5.10, at the σ_- peak, suggesting they were a collection of more than one sNR close together. The LSPR is again red shifted in oil by +50 nm to 700 nm compared to the resonance in water. Compared to the bNRs, the sNRs chosen are slightly less resonant with the λ_{CARS}=662.29 nm, the LSPR is more red shifted. However, the λ_{CARS} still lies within the width of the σ_- peak, so a resonant condition is satisfied, but not optimised. The measurements shown below will be discussed in comparison

with the extinction measurements performed after carrying out an eHCARS measurement.

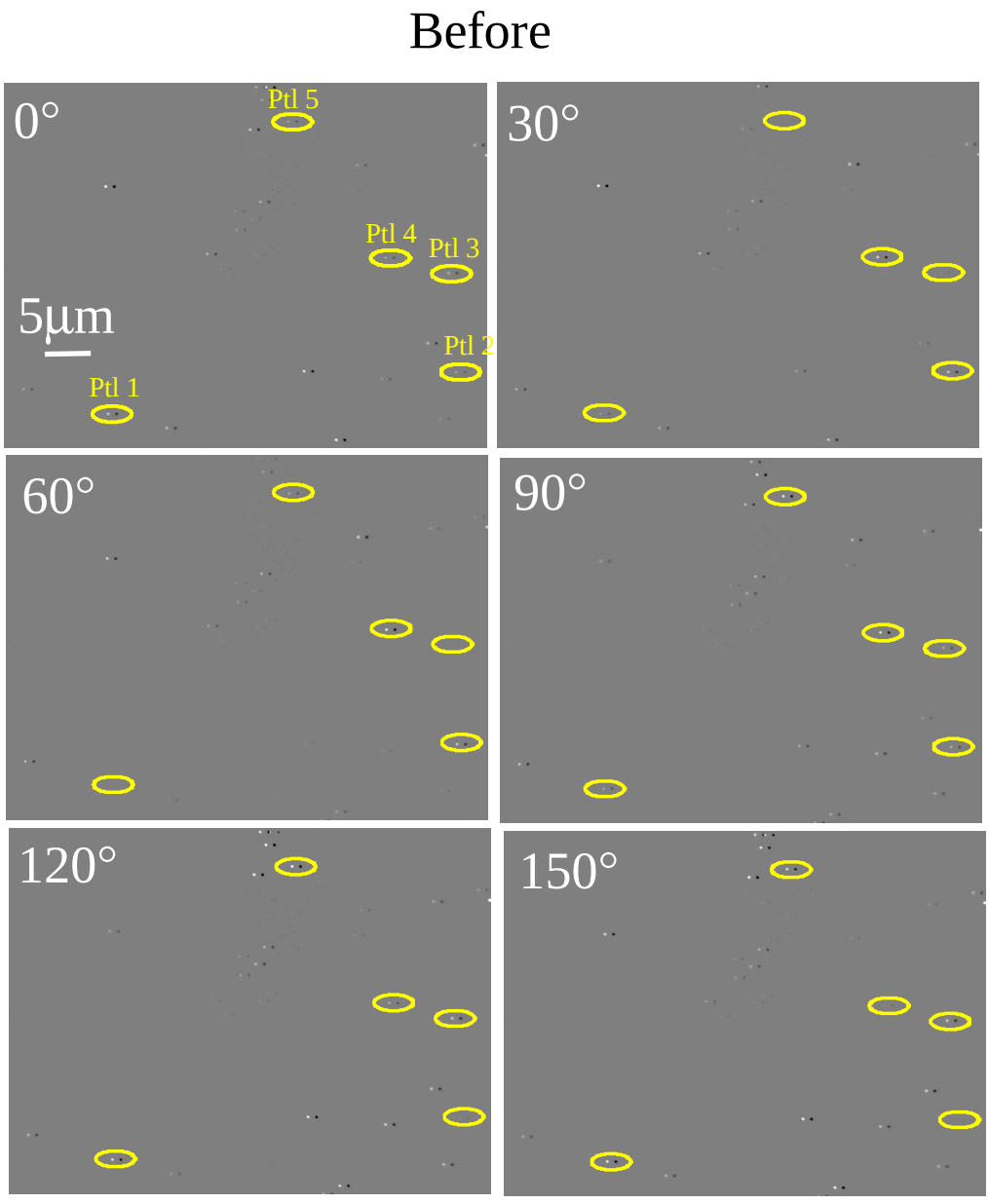

Figure 5.9: Wide-field polarisation angle θ resolved extinction images ($\Delta_{\pm}$) of a sNR covalently bound on to a glass coverslip immersed in silicone oil before eHCARS measurements. Shift S=1.6 μm between Δ_+ Δ_-, x128 averages repeated 10 times at each position, using 20 ms exposure, were recorded by the sCMOS PCO through the 100x 1.45NA objective. The grey scale white(black) maximum(minimum) is 0.15(-0.15)

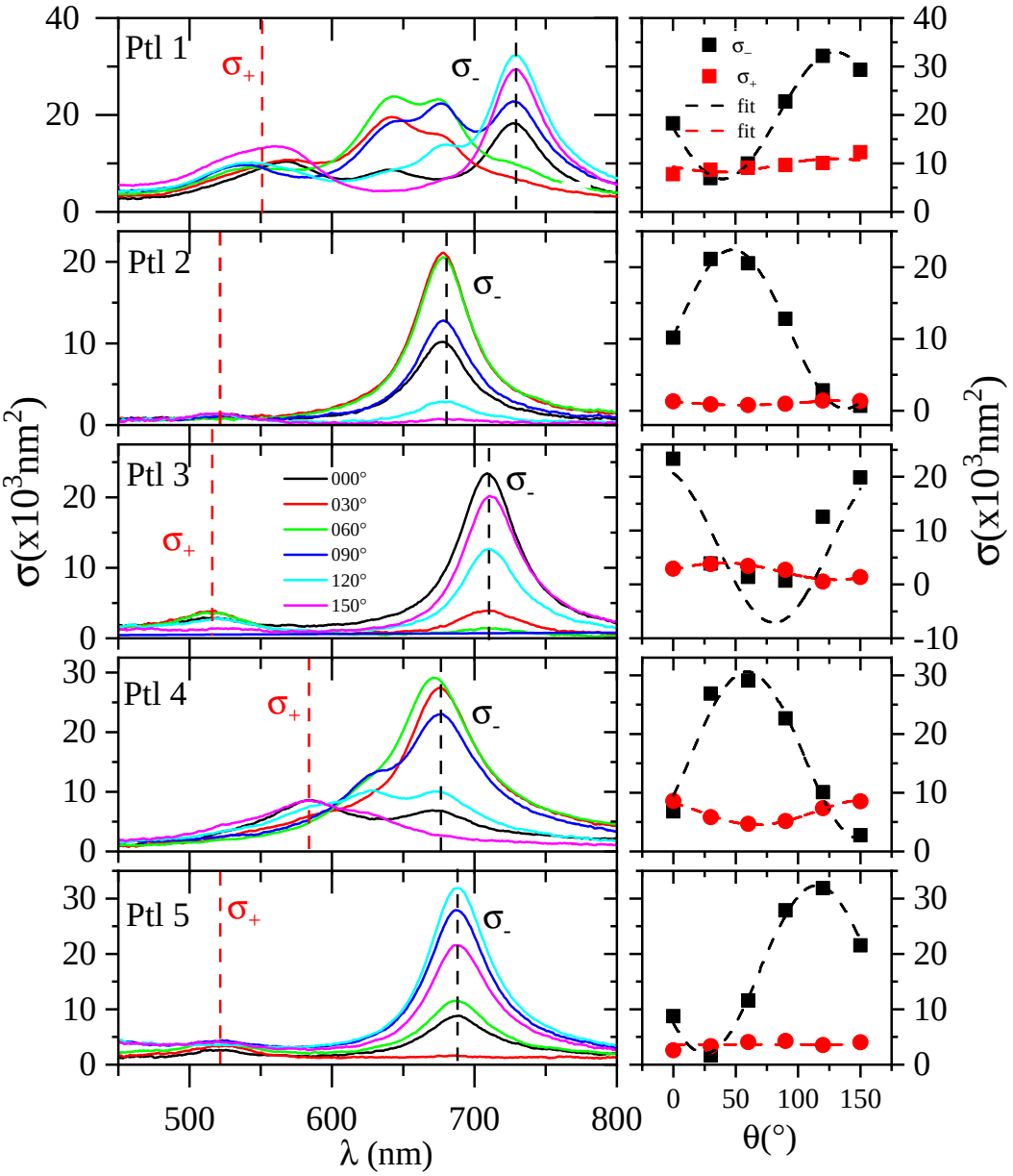

Figure 5.10: Single particle extinction spectrum of four different sNRs before eHCARS measurements, same particles indicated in Fig. 5.9. To the right of the spectrum is the corresponding $\sigma(\theta)$ of both the longitudinal and transverse peaks. The σ_- and σ_+ peaks are indicated with a black and red dashed line respectively. 200 acquisitions, 11 ms exposure, 100lines/mm grating, and input slip opening of 80 μm. 2×5 (spectrum×position) binning of the Andor CCD was used.

From the single particle extinction spectra, it's expected that particle 2 and 5 will provide a better enhance meant over particle 3, as the σ_- overlaps the λ_{CARS}=662.29 nm the best. In comparison with the single particle extinction spectroscopy of bNR, Fig. 5.3, we see that the sNRs σ is generally ×2-3 larger than σ bNR, due to their increased size. They also have an increased aspect ratio; therefore coupling more readily when θ is aligned along the long axis of the rod with resonant illumination. σ as a function of θ was again extracted from the spectrum at both the transverse

and longitudinal modes, plotted alongside the corresponding spectra in Fig. 5.10. $\sigma(\theta)$ was then fitted using Eq. 5.1, with fit parameters shown in Tab. 4.1

Peak	Ptl	α (nm^2)	Std Error	σ_A (nm^2)	Std Error	θ_0 (rad)	Std Error
σ-	1	0.66	0.02	19905.31	282.14	2.26	0.02
σ+	1	0.14	0.09	9600.78	596.29	-0.91	0.31
σ-	2	0.97	0.05	11359.77	342.43	3.98	0.02
σ+	2	0.3	0.05	1110.41	35.73	2.54	0.07
σ-	3	1.15	0.03	7139.33	3090.07	2.98	0.14
σ+	3	0.64	0.11	2451.39	181.24	3.84	0.08
σ-	4	0.87	0.11	16388.85	1085.7	35.59	0.06
σ+	4	0.32	0.03	6698.61	130.01	2.75	0.04
σ-	5	0.88	0.045	17209.09	465.35	2.01	0.02
σ+	5	0	0.13	3638.96	329.12	2.99	0

Table 5.1: Parameters of the $\sigma(\theta)$ fit in Fig. 5.10 using Eq. 5.1 for sNRs measured with single particle spectroscopy after eHCARS measurement.

5.2.2 eHCARS of silica coated gold nanorods

eHCARS measurements discussed in this section are performed using the exact same measurement setup discussed in Sec. 5.1.2 for the eHCARS measurements of bNRs. Here xy raster scans at the glass-oil interface, centred on a sNR were done to obtain y cuts through the signal of the sNR to reveal the enhancement to the oil signal. The images are offset according to Eq. 5.2 for the vertical component and Eq. 5.3 for the horizontal component so that the measurements are scaled to the signal in the silicone oil outside the sNR.

A power dependence of the |eHCARS| signal, projected into the co-linearly polarised component of the rods long axis, of two different sNRs is shown in Fig. 5.11. The sNRs were able to withstand much higher powers than the bNR before reshaping. bNRs were measured experimentally to have a damage (reshaping) threshold of $P_P P_S{}^{1/2}$>0.7$mW^{3/2}$, whilst for both sNRs show there is a relatively stable enhancement up to $P_P P_S{}^{1/2}$=30$mW^{3/2}$. Particle 3 shows a very stable enhancement of $\approx \times 10$ the silicone oil signal at the rod, with only a slight reduction to $<\times 10$ for the highest power tested. The TPF measured simultaneously increases with the increased power, also remaining stable. The power dependence of particle 3 is encouraging as there are no significant signs of reshaping.

However, the power dependence of the enhancement to the |eHCARS| signal in oil for particle 2 is measured to be decreasing up to $P_P P_S{}^{1/2}$=15$mW^{3/2}$. Beyond this power there is an increase in the enhancement followed by a sudden drop in the enhancement at $P_P P_S{}^{1/2}$=35$mW^{3/2}$. The decrease in enhancement from the co-linearly polarised |eHCARS| component of the rod can be attributed to the reshaping to a

more spherical shape as seen in the bNR. The slight increase at $P_P P_S^{1/2}$=30mW$^{3/2}$, followed by a sudden drop in enhancement at a higher power, could be explained by either a breaking of the silica shell or a non perfect shell coverage, together with gold melting at high power escaping the shell, causing the silicone oil to have a closer contact to the gold surface. The sNR then has a degree of freedom to allow the particle to reshape, hence the reduction in enhancement to follow. Further measurements with the likes of SEM would have to be conducted to investigate this behaviour.

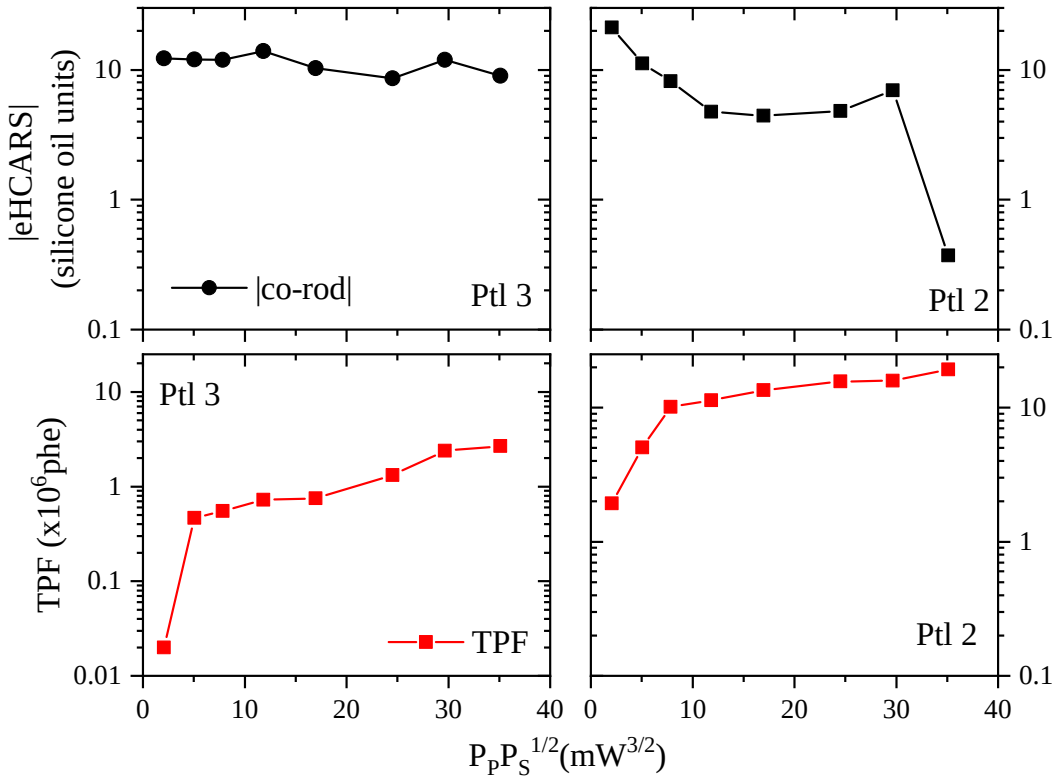

Figure 5.11: The eHCARS amplitude co-linearly polarised along the rod as a function of excitation power is shown in the top plots and below is the simultaneously obtained TPF. Two rods were imaged, particle 2 and 3. Values were obtained by performing the 2D imaging shown in Fig. 5.4, and extracting the peak signal at the sNR.

Particle 5 was repeatedly imaged in the xy plane using $P_P P_S^{1/2}$=12.5mW$^{3/2}$, utilising the same method used and described in Sec. 5.1.2. The power was chosen at this value due to the stable behaviour of the enhancement close to this power value seen in both particle 2 and 3, in Fig. 5.11. In contrast to the bNR repetition measurement in Fig. 5.5, the sNR has a larger enhancement in the first, i, measurement of $\times$20 the silicone oil signal outside the rod. In subsequent ii, iii, and iv eHCARS scans the enhancement to the silicone oil signal drops to $\times$15 but remains stable at this value. It is possible a similar behaviour was observed during the power dependence measurement on particle 3 in Fig. 5.11. To explain, in the power dependence measurement of particle 2 there was an initial high enhancement of the signal from the sNR, followed by a more stable enhancement regime after the particle had been scanned three times with the excitation field. Similarly particle 5 in Fig. 5.12 displays an initial enhancement that is reduced and stable after exposure

to the excitation field. It could be proposed that the support of the shell is stabilising the particles shape under excitation to such an extent that any defects in the lattice structure are annealed, hence the stable change in signal without evidence of particle reshaping. The slight reduction in the enhancement could be a result of the formation of point defects and tinned particles, by a mechanism proposed by Link *et al* [90] and modified by Gonzalez *et al* [118]. The shell here could be sufficiently holding the particle in the intermediate during it's reshaping from a rod to a sphere. Although move investigation would have to be carried out to confirm the reshaping dynamics, there is some evidence in the extinction after eHCARS measurement, which suggest that the particle is becoming slightly rounded but still remaining mostly rod shaped, see Fig. 5.14. There is still a strong polarisation dependence in the extinction, but it's slightly reduced, suggesting a less rod-like shape.

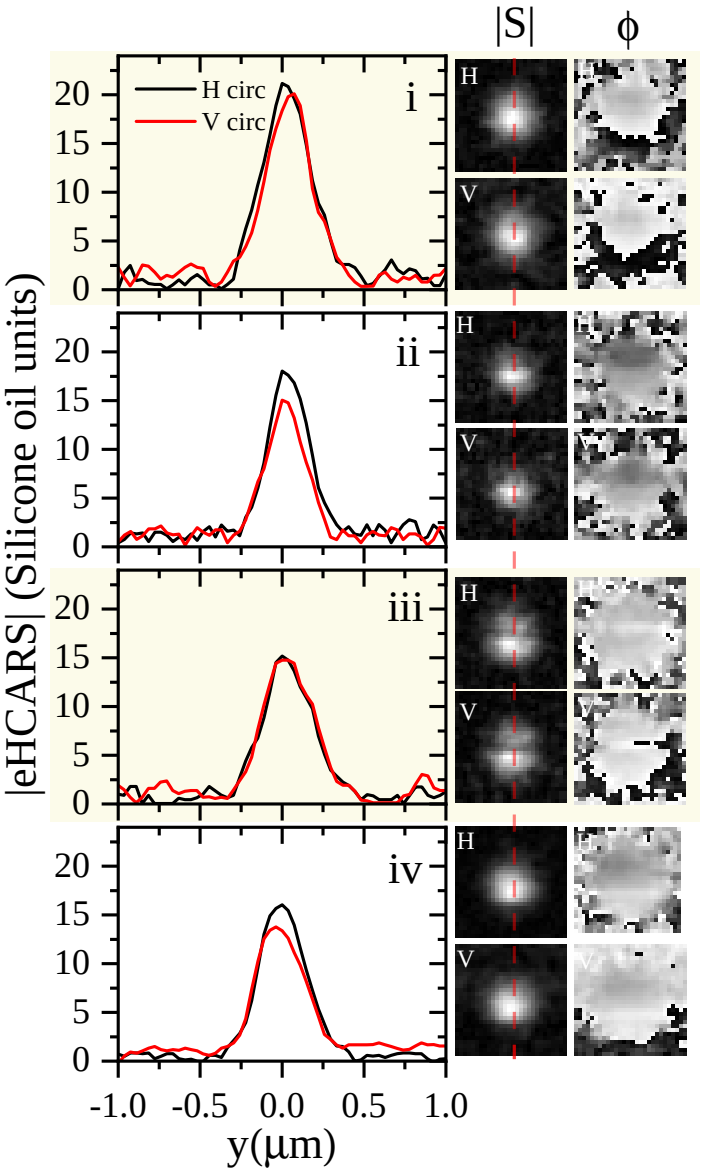

Figure 5.12: Four simultaneous repetitions (*i* to *iv*) eHCARS measurements of a sNR, with $P_P P_S^{1/2}$=12.5mWmW$^{3/2}$. 2 μm×2 μm rastercans with 1 ms dwell time over 80×80 pixels, at the glass-oil interface centred at the bNR. Right column: Amplitude ($|S|$) and phase (ϕ) in both H and V polarisation component images, cropped to 1 μm×1 μm from the measurement. Left column: eHCARS amplitude H and V polarisation y cuts through the centre of the bNRs, as indicated by a red dashed line in the images, normalised the the signal from the silicone.

5.2.3 Extinction after eHCARS

Below are extinction measurements of the sNRs taken after performing the eHCARS measurements in Sec. 5.2.2. Similar to Sec. 5.2.1, the wide field extinction in Fig. 5.13 and extinction spectroscopy in Fig. 5.14 is shown for 5 different structures after performing an eHCARS measurement. These are the same particles shown in Fig. 5.9.

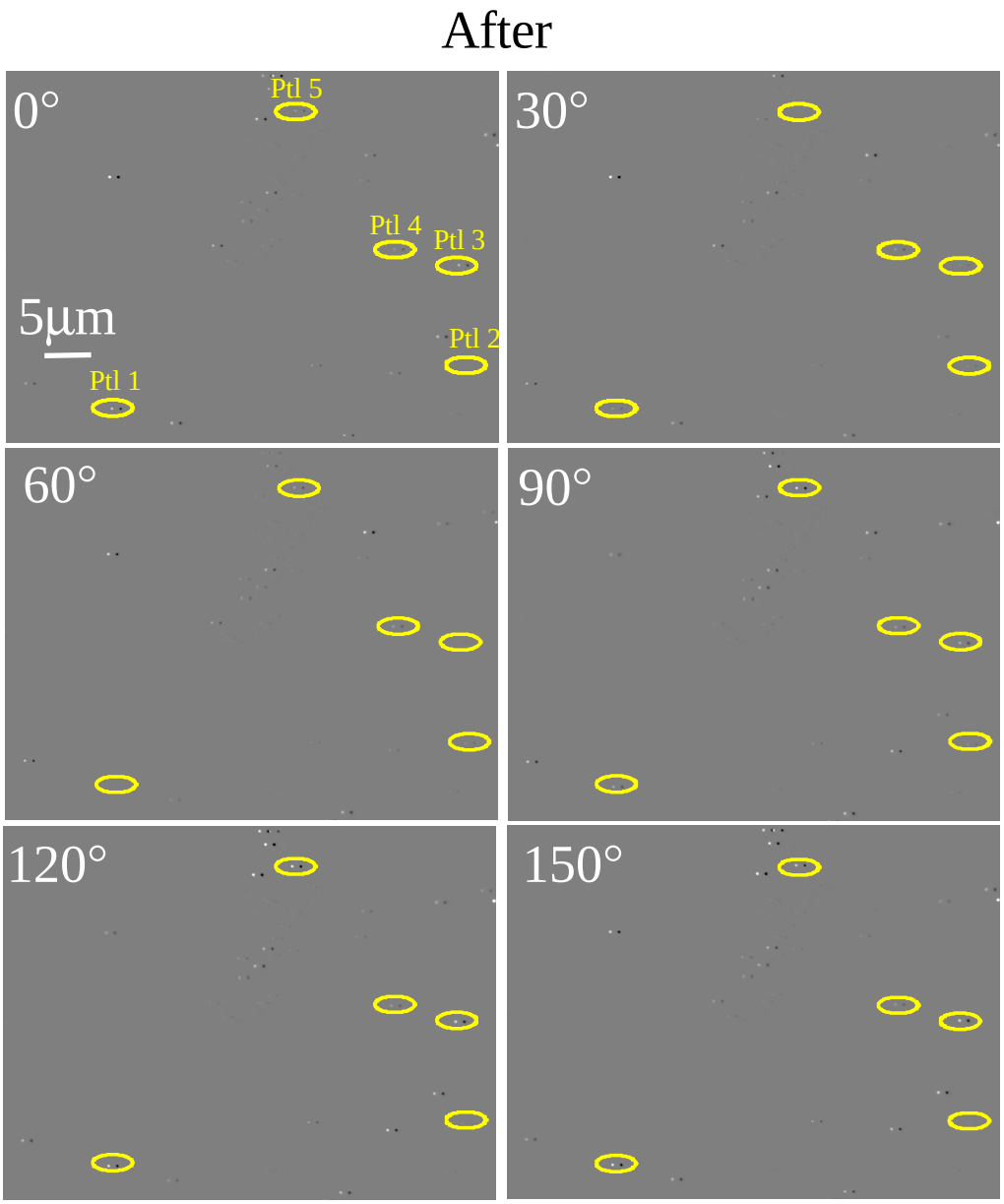

Figure 5.13: Wide-field polarisation angle θ resolved extinction images ($\Delta_{\pm}$) of a sNR after eHCARS measurements. Shift S=1.6 μm between Δ_+ Δ_-, x128 averages repeated 10 times at each position, using 20 ms exposure, were recorded by the sCMOS PCO thorough the 100x 1.45NA objective. The grey scale white(black) maximum(minimum) is 0.15(-0.15)

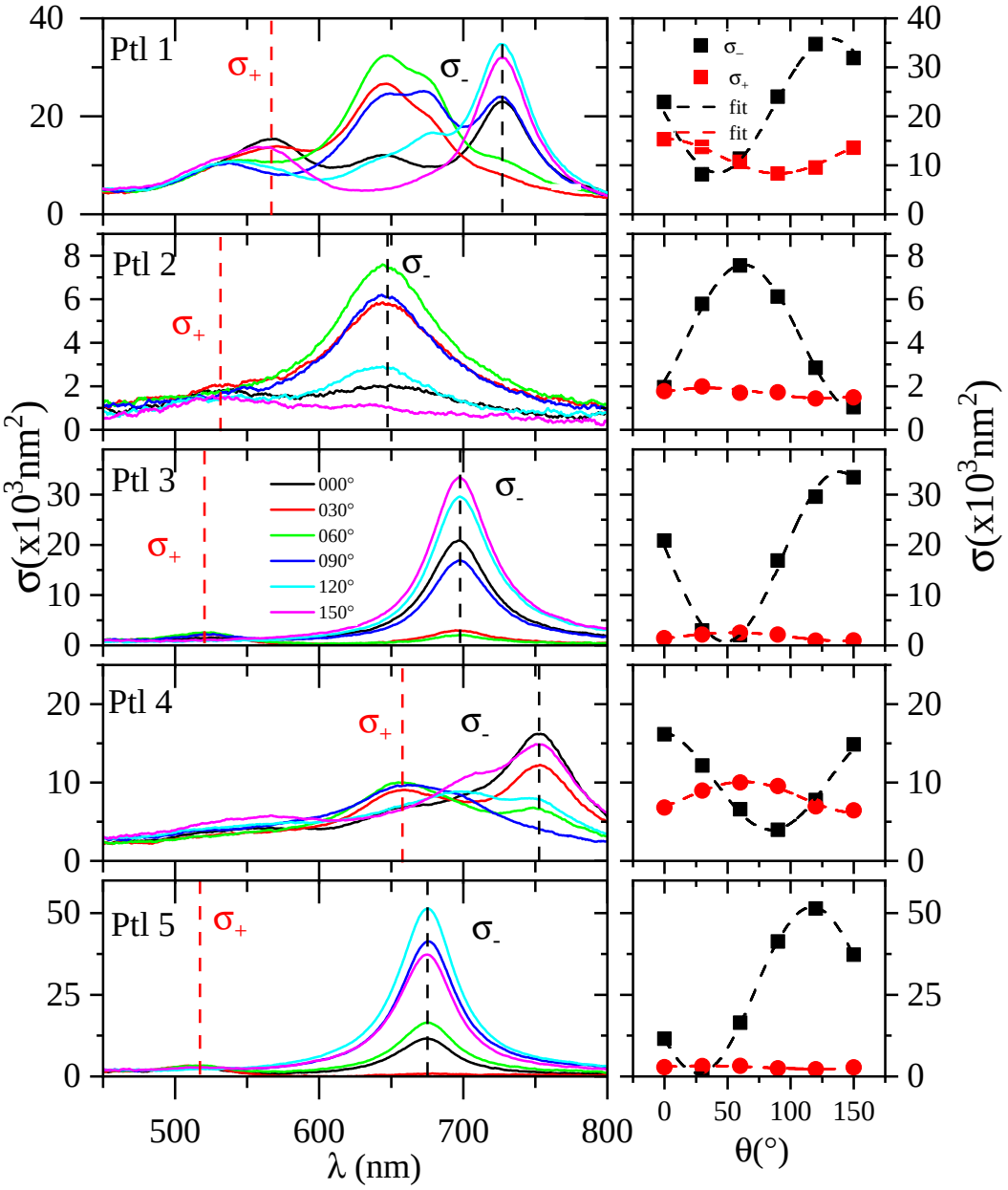

Figure 5.14: Single particle extinction spectrum of four different sNRs after eHCARS measurements. To the right of the spectrum is the corresponding $\sigma(\theta)$ of both the longitudinal and transverse peaks. The σ_- and σ_+ peaks are indicated with a black and red dashed line respectively. 200 acquisitions, 11 ms exposure, 100lines/mm grating, and input slip opening of 80 mum. 2×5 (spectrum×position) binning of the Andor CCD was used.

As previously mentioned, the single particle extinction spectroscopy measurements from the sNR objects labelled particle 1 and 4 contain additional contributions from an aggregation. There are multiple resonances in the σ corresponding to multiple rods with different orientation and LSPR close together. The extinction measurements of the aggregates are shown before and after because they were used for aligning the reference delay of the eHCARS signal; and for focussing on the correct z position in the sample. Setting up the experiment on an object that is similar, but not of interest, means the amount of exposures the particles of interest

experience is minimised. These objects used for alignment have also been exposed to the excitation fields and provide some insight into the reshaping dynamics present.

For a more quantitative comparison of the sNRs extinction after eHCARS, σ as a function of polarisation angle θ ($\sigma(\theta)$) for both the longitudinal and transverse mode was fitted with Eq. 5.1. The fitted curves are shown in Fig. 5.14 for each particle and the fit parameters in Tab. 4.2.

Peak	Ptl	α (nm^2)	Std Error	σ_A (nm^2)	Std Error	θ_0 (rad)	Std Error
σ-	1	0.6471	0.0218	19865.5	278.4014	2.2588	0.01532
σ+	1	0.2033	0.08601	10007.7	602.4013	2.9013	0.20944
σ-	2	0.9501	0.05258	4118.956	127.0729	7.0925	0.02298
σ+	2	0.0494	0.07012	981.007	48.60725	2.9703	0.70955
σ-	3	0.9588	0.29161	8120.709	1302.452	2.804	0.09928
σ+	3	0.4408	0.30337	2483.055	508.4414	3.6476	0.32853
σ-	4	0.6842	0.08876	4424.439	249.9817	1.0101	0.05839
σ+	4	0.7513	0.07482	12789.3	597.4992	1.0656	0.04397
σ-	5	0.8624	0.04713	14052.65	399.8049	1.9997	0.02333
σ+	5	0.2052	0.08864	3421.237	212.2101	1.7833	0.21377

Table 5.2: Parameters of the $\sigma(\theta)$ fit in Fig. 5.14 using Eq. 5.1 for sNRs measured with single particle spectroscopy after eHCARS measurement.

As the particle's polarisation dependence and LSPR is shape dependent, a change in the extinction is to be expected if the NRs undergo a reshaping during an eHCARS measurement. The difference in fit parameters from the $\sigma(\theta)$ fit performed before and after eHCARS was calculated. The difference was calculated for both the σ_- and σ_+ peaks. The change in central wavelength, $\delta\lambda$, was also determined for both σ_- and σ_+ resonances. $\delta\lambda$, and the change in $\sigma(\theta)$ fit parameters after eHCARS measurements are shown in Fig. 5.15.

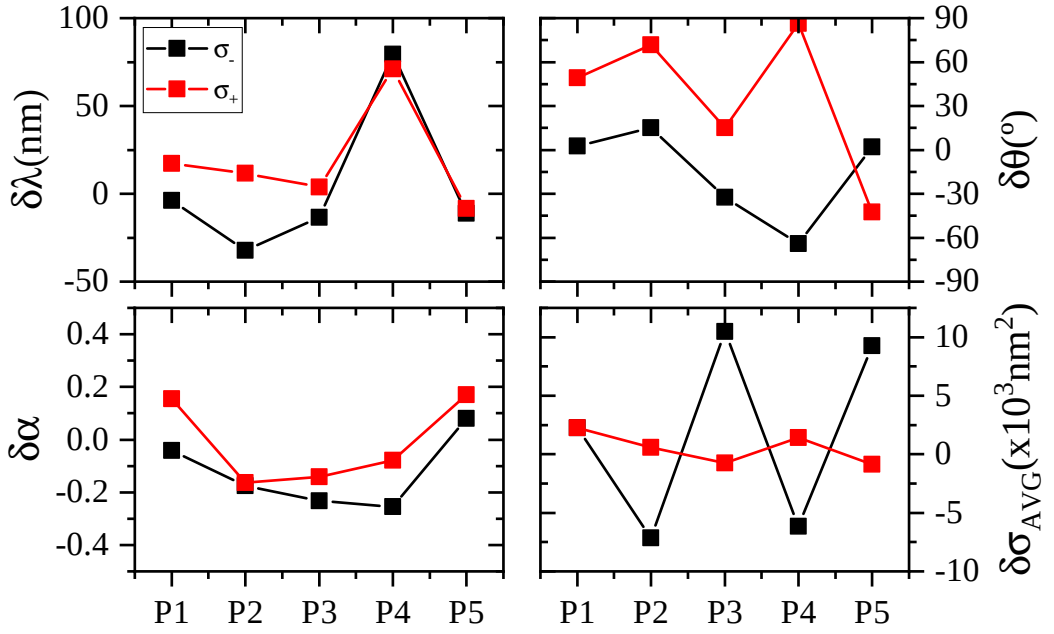

Figure 5.15: Change in the fit parameters to $\sigma(\theta)$ after performing eHCARS on particles 1 to 5. Difference in wavelength $\delta\lambda$, polarisation offset $\delta\theta_0$, polarisation amplitude $\delta\alpha$ and average extinction σ_{A} before and after eHCARS measurements.

With the exemption of the aggregate named particle 4, there is a blue $\delta\lambda$ shift in the σ_- resonance, and a red $\delta\lambda$ shift in the σ_+ after eHCARS. We see a reduction in the polarisation amplitude α for particles 1 to 4, but an increase in particle 5. The angle θ_0 (encoding the particle orientation in plane) is surprisingly also changed after eHCARS measurements, which is not consistent with the assumption that the particles were attached to the glass covalently and did not rotate during the measurement (no dramatic change in the eHCARS signal which would suggest the particle is moving). The change in polarisation dynamics, combined with the observation of a stable linearly polarised signal in eHCARS, could indicate that the elongated axis of the rod is being forced off axis within the silica shell. A change in α suggests that there is a change in shape during the measurement, but values are still typically >0.5 suggesting that the particles are most likely a reduced rod shape after eHCARS in this case and not completely spherical.

The change in the average σ_{A} after eHCARS varies from rod to rod. In general it is measured that there is a blue shift to the σ_- peak after eHCARS.

We see that for particle 3 and 5 there is a slightly improved overlap of the LSPR with the λ_{CARS} after eHCARS measurement. Particle 3 shifts from 710 nm to 697 nm and particle 5 shifts from 686 nm to 675 nm, thus improving the overlap with λ_{CARS}, which would improve the enhancement. Particle 3 and 5 also show an increased σ_{A} after eHCARS measurement, suggesting possibly that the longitudinal resonance is somehow being annealed. There is a reduction in the α for particle 3, and an increase in particle 5 (5 becoming more rod-like and 3 more spherical), but both seeing an increased σ_{A}. It is therefore possible that the λ_{CARS} scattering is driving the reshaping and annealing of the particles into a specific mode governed by the CARS resonant field; these particles reshaped improving their resonant mode, possibly becoming more rod-like in shape. It has been measured by Piotto *et al*

that the excitation fields fluency and pulse duration is crucial in the reshaping of gold NPs [119]. The high power exposure measurement on particle 2 has resulted in a reduction in the extinction amplitude and a significant broadening of the LSPR. The broadening, a blue shift in LSPR and significant reduction in the enhancement observed at higher power would suggest that this particle has under gone significant reshaping into a more rounded shape.

5.3 FIB sample

The LSPR along the longitudinal mode of a NR is dependent on the geometrical aspect ratio, meaning NRs can be tuned during synthesis to provide the desired resonances. NRs can also be assembled into various multiple rod systems, such as dimers or trimers. These systems have gained significant interest due to their additional amplification of the local field strength by the coupling of plasmons over single particles. Dimer systems have been explored in both SERS [120, 121] and SECARS [122, 123] experiments, with the majority focusing on the enhancement at specific junctions between coupled nanoparticle systems exploiting the further enhancement to a single particle system [124, 125, 126]. Nanorod dimers are a promising structure owing to their high aspect ratio and plasmon modes. It has been determined for side-by-side nanorod dimers, which were investigated in this work, (see Fig. 5.17 for illustration) there is an increase in the enhancement when reducing the separation and aspect ratio of the individual rods. Four possible dimer modes are listed in Fig. 5.17, with a snapshot of the induced polarisation indicated by positive and negative symbols. There is an antenna mode, Fig. 5.17 1., is vertically across the dimer gap, an anti-bonding mode, Fig. 5.17 2., aligned horizontally along the dimer gap, and bonding modes Fig. 5.17 3. and 4, the higher order bonding mode becomes present in larger antennas [127, 128]. In this case for enhancement of CARS measurements it is possible to have a dimer system that is both resonant with λ_{CARS}=662.29 nm and λ_{P}=820 nm, additionally contributing to the overall enhancement of the CARS signal.

The enhancement to the eHCARS signal in the vicinity of varying length dimer assemblies was investigated. The dimer structures that were studied are milled via focused ion beam lithography (FIB), by Hecht *et al* [129], from a single monocrystalline gold film. The FIB sample consists of multiple 50 nm gold flakes that have various milled dimer arrays. The specific array characterised with extinction spectroscopy and eHCARS, to follow, consisted of 14 dimers with separation of 27 nm, increasing in length from 45 nm to a more rod-like shape of length 180 nm, (D1 to D14) see Fig. 5.16. Dimers produced in this way are limited to a minimum separation of 20 nm; a reduction of the separation would yield a greater enhancement, (dimers investigated here have 27 nm separation). The gold flake is placed on top of a glass hole and submersed in silicone oil. The glass-oil region was used for calibration and for retrieving a the glass-oil interface signal used in the calculation of the enhancement to the signal at the dimers in units of silicone oil (Eq. 5.2 and Eq. 5.3). The eHCARS signal from the glass-oil interface outside the flake was used in the normalisation to avoid contributions from any debris there might be present near the dimers, remaining from the fabrication process.

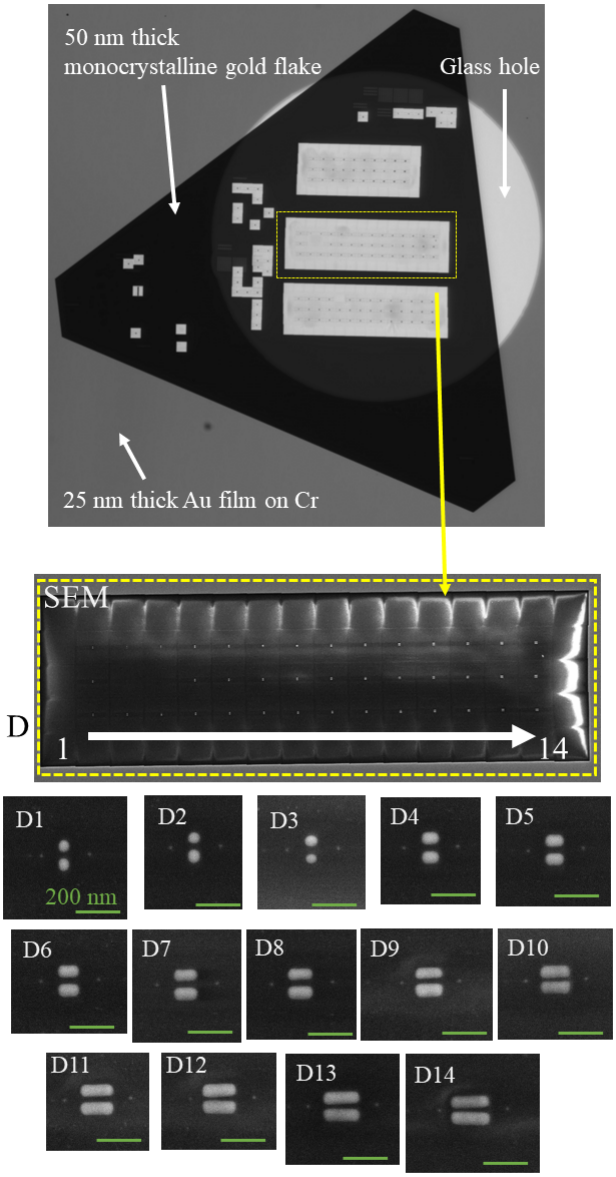

Figure 5.16: On top is a transmission image of the entire gold flake, the array that was imaged is outlined with a dotted yellow rectangle. Below are SEM images, performed by Hecht *et al*, of the entire array with dimers in row D labelled from 1 to 14. A higher resolution SEM image is shown below of all 14 dimers.

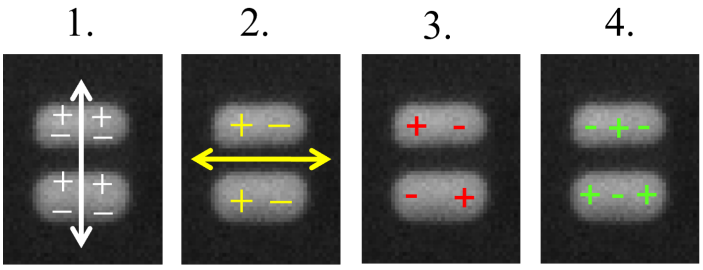

Figure 5.17: Sketch on an SEM image of a side-by-side nanorod dimer showing four possible plasmon modes. 1.) Antenna, 2.) Anti-bonding, 3.) Bonding, and 4.) Higher order bonding mode for large antennas.

5.3.1 FIB dimers extinction spectroscopy

The array of 14 dimers in row C were characterised with polarisation resolved extinction spectroscopy, utilising the same protocols previously discussed for the rbR and sNR, see Sec. 5.1.1. The results for all 14 dimers are shown in Fig. 5.18. From the polarisation resolved spectra, we see that in the smaller aspect ratio dimers there is one dominant extinction σ peak with a very slight polarisation dependence, at the shorter lengths. The extinction at shorter dimer lengths is dominated by the antenna mode (Fig. 5.17 1.). With increasing rod length there is an increased contribution from the bonding and anti-bonding modes, especially evident by Fig. 5.18 D5. The red shifted peak is a result of the bonding mode, Fig. 5.17 3, it's resonance will have a strong dependence on the rod length, shifting further into the red for longer length rods. Interestingly, by the rod length in D10 there is a slight modulation in the antenna mode peak, suggesting an additional resonance mode. This mode can be attributed to the higher order Fig. 5.17 4. mode with two nodes, present only for longer antennas, and will also be strongly size dependent (red shifts for longer length rods). Here it should be noted that these dimers were synthesised specifically such that the higher order mode would be resonant with λ_{CARS} for silicone oil resonances, whilst the bonding mode would be resonant with either the λ_{P} or λ_{S}. The antenna mode of these dimers would also be in overlap with λ_{CARS} when imaging the using the CH stretch bonds in lipids. It's likely D9, 10 or 11 will give the highest enhancement, they seem to provide the best overlap with both λ_{CARS} and λ_{P}, with D14 possibly having a red shifted peak overlapping with the λ_{S} outside the spectral range of the extinction measurement done. The antenna mode's σ doesn't change much, if it does so it's mostly due to the variation in size from synthesis. It should be noted that a background subtraction of the extinction spectroscopy was extremely difficult due to inhomogeneous contributions from gold debris remaining on the glass from the synthesis; hence, the negative extinction values and background signal in some cases that could not be removed.

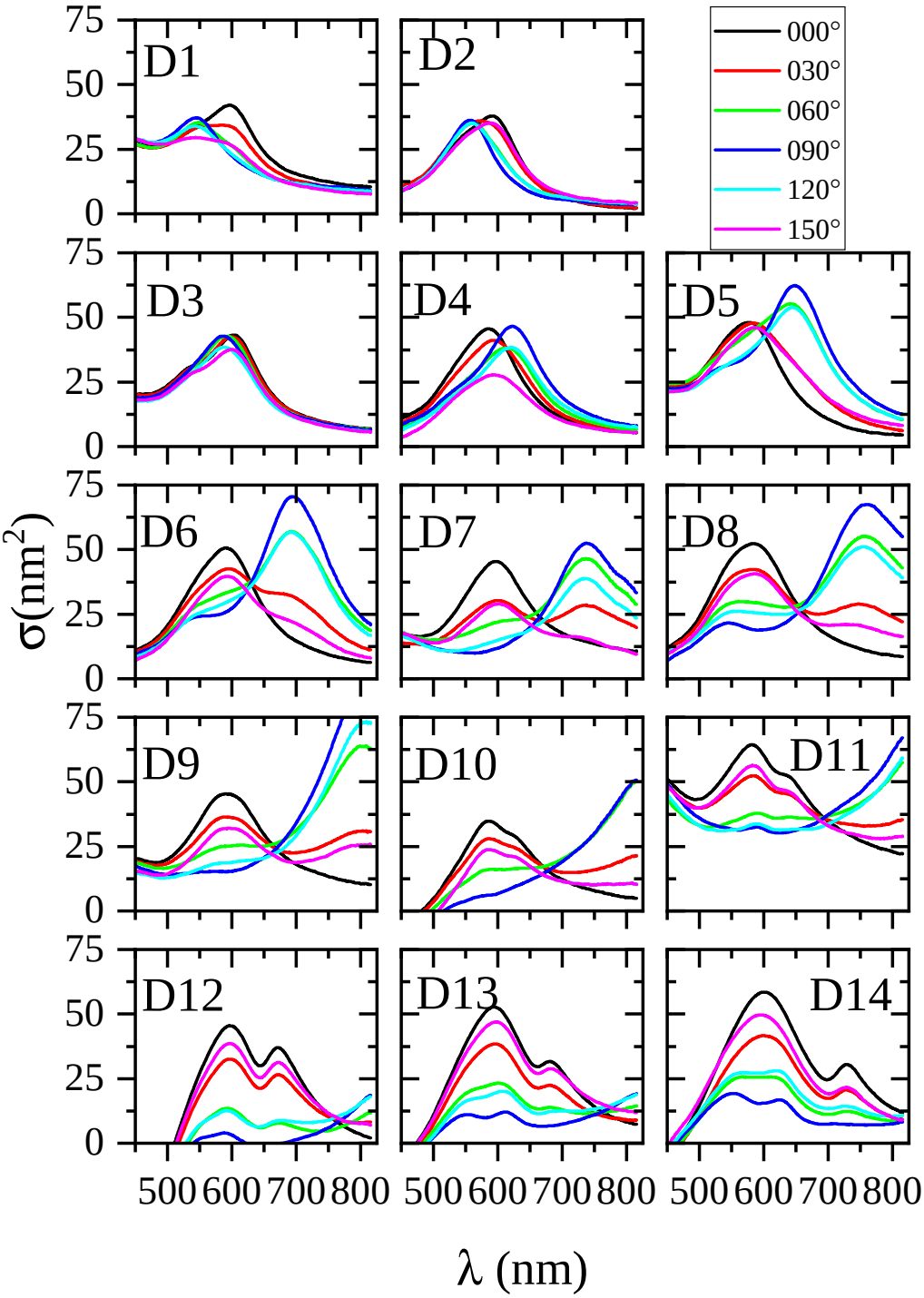

Figure 5.18: Single particle extinction spectrum of 14 dimers in the array with 27 nm separation and increasing length from 1 to 14. 200 acquisitions, 11 ms exposure, 100lines/mm grating, and input slip opening of 80 *mu*m. 2×5 (spectrum×position) binning of the Andor CCD was used. (see Sec. 5.1.1 for measurement details)

5.3.2 eHCARS FIB

Due to the increased robustness of the FIB dimers compared to colloidal gold nanoparticles it was possible to perform a full linear polarisation dependence of

all 14 dimers. Unlike in the eHCARS measurements performed on the bNR and sNR a servo controlled $\lambda/2$ plate was inserted into the objective waveplate, not $\lambda/4$. This meant that the linear excitation polarisation could be rotated to probe the FIB sample bonding and anti-bonding modes. Knowing that the sNRs provided a relatively stable eHCARS signal at $P_P P_S^{1/2}$=12.5mW$^{3/2}$, the same power was used in this case with the FIB dimers. Using the $\lambda/2$ would mean that the coupling between the resonance and excitation field is more intense, meaning that the excitation is stronger in this case than with the $\lambda/4$. However, it was expected that the larger dimers would be much more stable than the colloid rods, owing to their monocrystalline structure and more thermal mass.

2D xy scans were performed centred at each dimer at the z glass-oil interface place, with IFD=2904 cm^{-1} (resonant with the silicone oil peak). Scans were 2 μm wide and either 4 μm or 2 μm tall, using 0.037 mum/pixel. The 100x, 1.45NA, oil immersion objective was used, and the scanning was performed by moving the sample with the nanostage. Polarisation resolved eHCARS measurements are shown in Fig. 5.19 and Fig. 5.20. The left images are eHCARS(θ=50°) H and V component amplitude (|eHCARS|) and phase (ϕ) colour encoded into a value-hue plot, where the colour represents the phase and the intensity the amplitude of the signal. The rods are aligned vertically, each rod separated by 27 nm along the x axis to form the dimer. On the right is the |eHCARS| as a function of the angle of rotation of a linear polariser θ, |eHCARS|(θ), where θ=0°is linearly polarised with the x axis. θ corresponds to the angle of the $\lambda/2$ plate, therefore it should be noted that the linear polarisation is rotated by $2 \times \theta$. θ was rotated from -70 °to +60 °in steps of 10 °. |eHCARS|(θ) is obtained by making a cut through the centre of the 2D image, a line of pixels from each polarisation angle was then stitched together along the x-axis of the plot to generate a colour map, the |eHCARS| is scaled in the colour as shown by the scale bar. The 2D images shown are at θ=50 °, a pink line indicates the y cut location.

The polarisation resolved eHCARS measurements shown in Fig. 5.19 and Fig. 5.20 reveal a significant increase in the eHCARS signal at the dimers with increasing length (1 being the shortest and 14 the longest). The highest eHCARS signal was measured in D9, possibly owing to the fact that D9 is a special case where the bonding mode is red shifted to overlap the E_P and the higher order mode with two nodes is overlapped with E_{CARS} perfectly, see D9 in Fig. 5.18. There is an obvious polarisation dependence in the |eHCARS| H component, with a resonance at -40 °and +50 °(remembering that θ is half the angle of polarisation axis, 90,°orthogonal angle is θ=45 degree). The highest signal from the dimers is measured as the polarisation of the excitation is aligned across the the dimer, promoting the strongest coupling to the resonances. As the detection is in epi through the $\lambda/2$ plate, and the excitation is H polarised, the |eHCARS| V component tells us that there is a polarisation dependent source of either un-polarised or orthogonally generated eHCARS as a result of H polarised excitation. The modulation of the V component |eHCARS|(θ) signal is out of phase with the H component (when θ is rotated to give H max, V is minimised), apart from at the θ=0 °rotation where both the H and V component are minimised in some cases. There is more V component to the signal for longer rods, which is consistent with the fact that we expect to have signal arising from higher order modes with increased length. The red shift in LSPR allows for more

electron mobility on the surface, therefore there are more available modes, which in turn produce more signal at different polarisation angles due to the axial orientation of the modes.

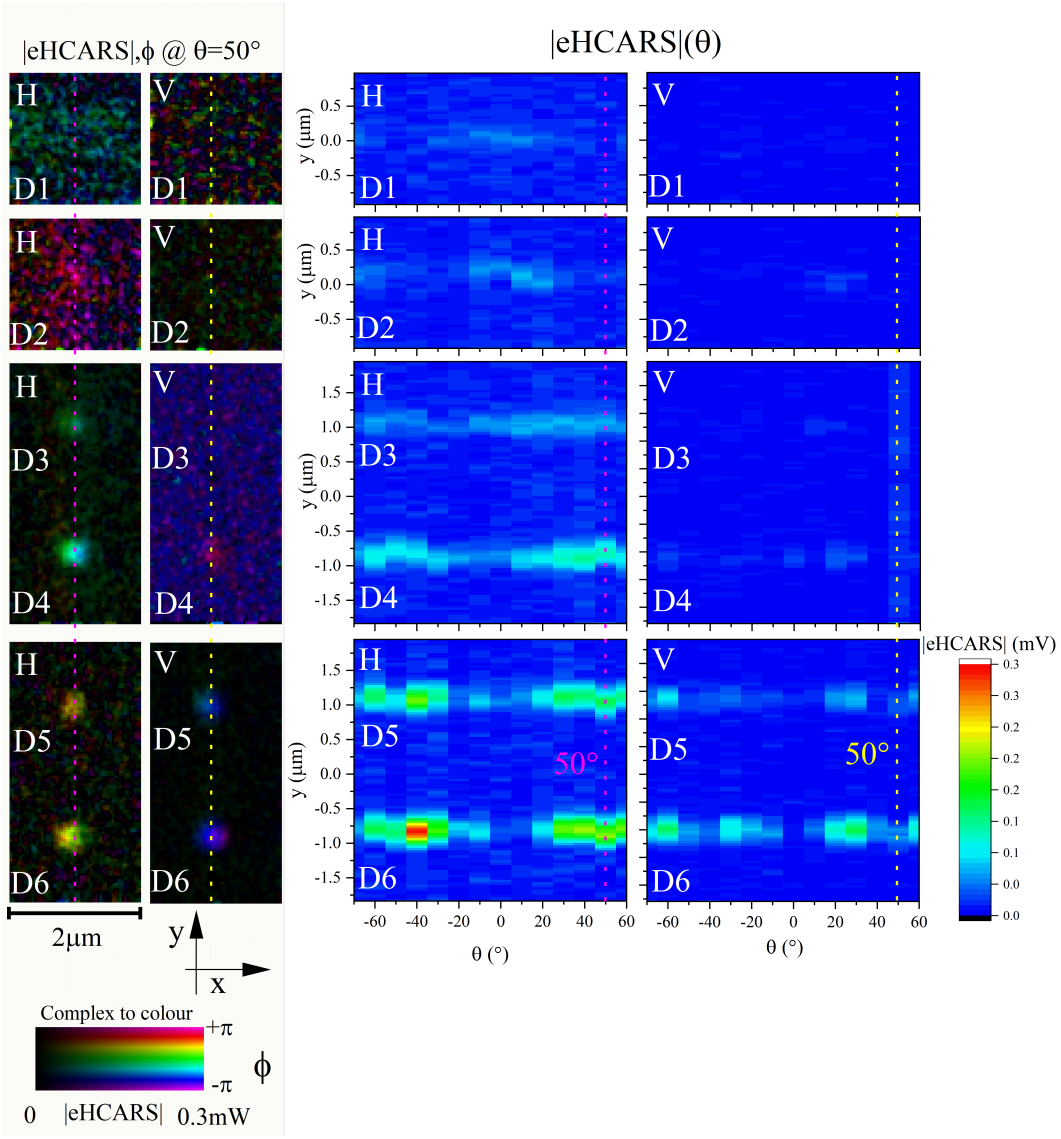

Figure 5.19: EHCARS measurements of FIB dimers 1 to 6. Left: 2D eHCARS H and V encoded amplitude and phase images, 2 μm wide, 0.037 mum/pixel, with polarisation θ=50 °, IFD=2904 cm^{-1}, and $P_P P_S^{1/2}$=12.5mW$^{3/2}$. A pink and yellow dashed line indicates the y cut obtained to construct the |eHCARS|(θ) colour maps of both H and V polarisation components. Right: |eHCARS| y cuts at polarisation angles from -70 °to +60 °for both H and V polarisation components.

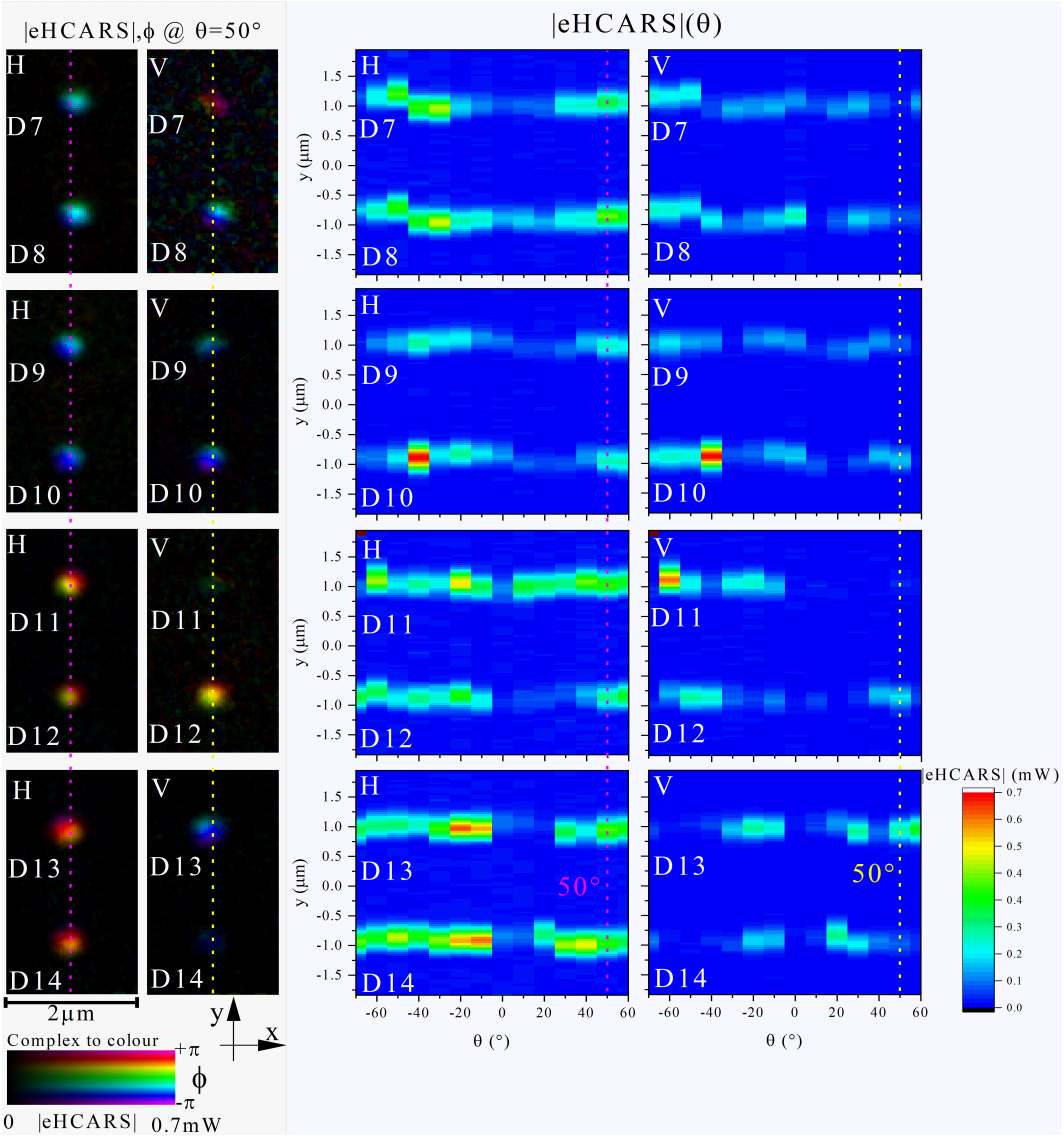

Figure 5.20: EHCARS measurements of FIB dimers 7 to 14. Left: 2D eHCARS H and V encoded amplitude and phase images, 2 μm wide, 0.037 mum/pixel, with polarisation θ=50 °, IFD=2904 cm^{-1}, and $P_P P_S^{1/2}$=12.5mW$^{3/2}$. A pink and yellow dashed line indicates the y cut obtained to construct the |eHCARS|(θ) colour maps of both H and V polarisation components. Right: |eHCARS| y cuts at polarisation angles from -70 °to +60 °for both H and V polarisation components.

The enhancement to the silicone oil signal at the dimer was calculated for each dimer at all polarisation angles using Eq. 5.3 and Eq. 5.2 to offset the silicone oil signal, labelled in Fig. 5.16, shown in Fig. 3.15. The enhancement, Fig. 5.21, was measured to be as high as ×100 the silicone oil signal from dimers with a length similar to D9. This could again be attributed to the improved overlap of the longitudinal mode with the E_P and the E_{CARS} simultaneously contributing to the enhancement. In general, the enhancement increases with increasing dimer length, The enhancement is consistently higher in the H component over the V component, as expected. In comparison to the bNRs and sNRs, there is a significantly larger and more stable enhancement measured from the dimers, which makes dimer samples

ideal for probing low concentrations of chemical substances near the dimer region in SE-CARS. The drawback of using the dimers for sensing nano-objects is that the sensitivity is limited by their separation, meaning that the object to be sensed has to fit within the dimer gap. There is obviously a trade off between stability and sensitivity when it comes to LFE with gold nanorods.

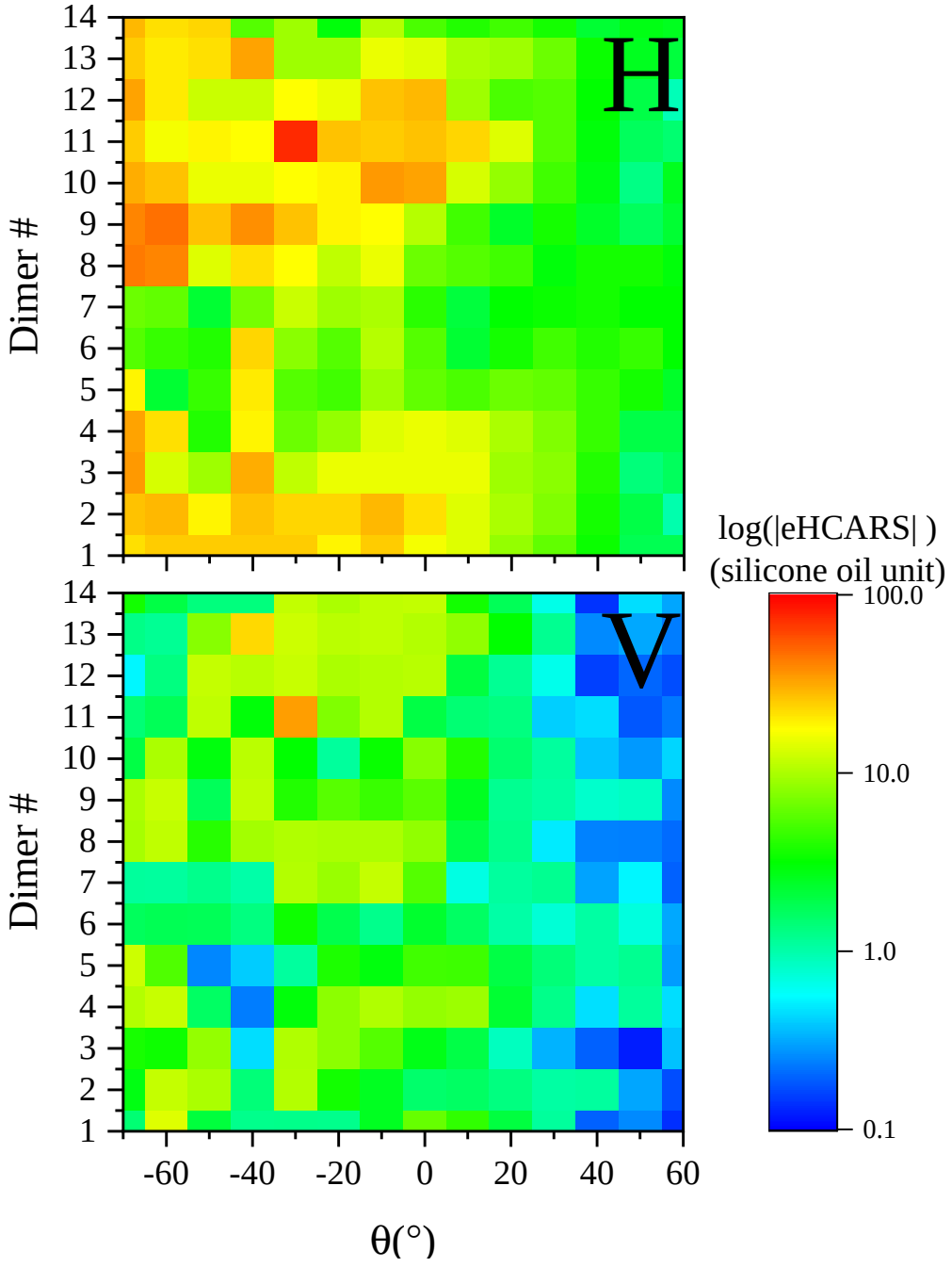

Figure 5.21: Enhancement to the silicone oil interface signal at each dimer in the array, scaled to units of glass-silicone oil signal. Each pixel in the colour map represents a θ and a dimer, the colour is the log(|eHCARS|) in silicone oil units.

Conclusion

In summary, a novel heterodyne epi-detected CARS technique was explored, as a stand-alone technique, and applied in the vicinity of plasmonic gold nanoparticles. In Chapter 4 Sec. 4.1, eHCARS measurements of silicone oil droplets supported on a glass substrate fixed in a low concentration of agar in water are shown.

In Chapter 5 Sec. 5.1 the first local field enhancement of eHCARS was attempted utilising bare gold nanorods (bNRs). Although providing a very promising x10 enhancement to the CARS signal in their vicinity, the bNRs were far too unstable under prolonged laser excitation to be utilised in future for the sensing of biological material. From the eHCARS dual-polarisation signal it was possible to deduce that the rods were reshaping during the measurement time, an observation of the reduced characteristic polarisation dependent rod like behaviour to a more special particle signal with reduced polarisation dependence and signal enhancement.

It is extremely important for this kind of biosensing that the nanoparticle of choice provides a stable and large local field enhancement to the CARS signal. After prolonged experimentation with bNRs, attempting imaging without reshaping unsuccessfully, it was suggested that silica coated gold nanorods (sNRs) might be a better alternative. In Chapter 5 Sec. 5.2 the local field enhancement to the CARS signal and stability of sNRs was explored. The hope was that the silica coating around the NRs would aid in confining the particles shape if there was reshaping occurring under laser exposure. It was observed that the sNRs have a significantly improved stability with repeated laser exposures, and also gave a x15 signal enhancement in the vicinity. Although far more stable than the bNRs, it was evident from the single particle extinction spectroscopy performed after laser exposure (compared with measurements before laser exposure) that the sNRs were still undergoing structural changes during the measurement. A reshaping mechanism where the middle of NR, along its long axis, would begin to bulge, and shorten within the silica coating (conserving the gold volume). Reshaping was evidenced by a slight reduction in the enhancement due to a shortening of the long rod axis and an slight decrease in the polarisation amplitude which implies that the rod is becoming less rod-like and more spherical.

The enhancement to eHCARS from various length, 40 to 120 nm, focus ion beam (FIB) fabricated gold nanorod dimers by Hecht were measured in Chapter 5 Sec. 5.3. Due to their increased size, functions between dimers and higher order modes there is significantly stronger enhancement, up to x100, from there dimers compared to stand-alone NRs. The largest enhancement seen from a dimers whose anti-bonding mode overlaps with either the pump or Stokes wavelength and having a longer an-

tenna, higher order mode, which overlaps with the CARS wavelength. To follow this work, further investigations of various NR size and silica shell thickness should be carried out to see if the reshaping can be suppressed by increasing the thermal mass and spatial confinement strength of the shell. Once optimisation of the shelling is completed, one can move forward to make attempts to sense nanoscale materials in the vicinity of NRs. A proof of concept, starting point, for nanoscale sensing using this technique would be to fix the gold NRs to a surface, and flow a fluid containing nanoscale polystyrene beads at a very low flow rate over the NR. As a nanoscale polystyrene bead passes the NR, the observer should see a signal change corresponding to that event (ensuring the eHARS is tuned to the polystyrene resonance). One of the major goals of this work is to progress with developing a sensor capable of imaging nanodomains in a supported lipid bilayer. To do so, NRs would have to be placed underneath a supported lipid bilayer. More work would have to be done in finding a compatible surface functionalisation protocol for covalently binding the NRs to the glass surface which is also compatible with the formation of supported lipid bilayers. NRs must be bound to the glass or they will be optically trapped, and moved, by the incident laser. Synthetic supported lipid bilayers require a hydrophilic surface to form, unfortunately the tosyl chloride used for binding the sNRs to the glass will cause the surface to become more hydrophobic; therefore either finding a specific concentration of tosyl chloride that gives enough binding sites for NRs and still allows the formation of supported lipid bilayers or a different protocol would have to be used.

Bibliography

[1] Wiley spectral database https://spectrabase.com/spectrum/6swzdh2utyb.

[2] Jiun-Jeng Chen, Kimberly N Struk, and Anthony B Brennan. Surface modification of silicate glass using 3-(mercaptopropyl) trimethoxysilane for thiol–ene polymerization. *Langmuir*, 27(22):13754–13761, 2011.

[3] Wen-Hao Chen, Yen-Ta Tseng, Shuchen Hsieh, Wan-Chun Liu, Chiung-Wen Hsieh, Chin-Wei Wu, Chen-Han Huang, Hsing-Ying Lin, Chao-Wen Chen, Pei-Ying Lin, et al. Silanization of solid surfaces via mercaptopropylsilatrane: a new approach of constructing gold colloid monolayers. *RSC Advances*, 4(87):46527–46535, 2014.

[4] Greg T Hermanson. *Bioconjugate techniques*. Academic press, 2013.

[5] Clara Sue Ball. The early history of the compound microscope. *Bios*, pages 51–60, 1966.

[6] David Bardell. The invention of the microscope. *Bios*, 75(2):78–84, 2004.

[7] Galileo Galilei. *Le opere di Galileo Galilei*, volume 1. Societa editrice fiorentina, 1842.

[8] David Bardell. The first record of microscopic observations. *BioScience*, 33(1):36–38, 1983.

[9] Robert Hooke. *Micrographia*. The Royal Society, 1665.

[10] Brian J Ford. Single lens. *The Story of the Simple Microscope. London*, 1985.

[11] Howard Gest. The discovery of microorganisms by robert hooke and antoni van leeuwenhoek, fellows of the royal society. *Notes and records of the Royal Society of London*, 58(2):187–201, 2004.

[12] Frits Zernike. How i discovered phase contrast. *Science*, 121(3141):345–349, 1955.

[13] Walter Lang. *Nomarski differential interference-contrast microscopy*. Carl Zeiss, 1982.

[14] Ernst Abbe. Vii. on the estimation of aperture in the microscope. *Journal of the Royal Microscopical Society*, 1(3):388–423, 1881.

[15] David Halliday, Robert Resnick, and Jearl Walker. *Fundamentals of physics*. John Wiley & Sons, 2013.

[16] Richard A Zsigmondy. Properties of colloids. *Nobel lecture*, 11, 1926.

[17] Max Knoll and Ernst Ruska. Das elektronenmikroskop. *Zeitschrift für physik*, 78(5):318–339, 1932.

[18] G. Binnig, H. Rohrer, Ch. Gerber, and E. Weibel. Surface studies by scanning tunneling microscopy. *Phys. Rev. Lett.*, 49:57, 1982.

[19] Mohsen Rajaei, Mohammad Ali Almajhadi, Jinwei Zeng, and H Kumar Wickramasinghe. Near-field nanoprobing using si tip-au nanoparticle photoinduced force microscopy with 120: 1 signal-to-noise ratio, sub-6-nm resolution. *Optics express*, 26(20):26365–26376, 2018.

[20] Maciej Dabrowski, Yanan Dai, and Hrvoje Petek. Ultrafast microscopy: Imaging light with photoelectrons on the nano–femto scale. *The journal of physical chemistry letters*, 8(18):4446–4455, 2017.

[21] Sayantan Mahapatra, Yingying Ning, Jeremy F Schultz, Linfei Li, Jun-Long Zhang, and Nan Jiang. Angstrom scale chemical analysis of metal supported trans-and cis-regioisomers by ultrahigh vacuum tip-enhanced raman mapping. *Nano letters*, 19(5):3267–3272, 2019.

[22] Jeff W Lichtman and José-Angel Conchello. Fluorescence microscopy. *Nature methods*, 2(12):910–919, 2005.

[23] Ian Harper. *Fluorescence applications in biotechnology and life sciences*, chapter 2. Wiley-Blackwell, 2009.

[24] E. Betzig, G.H. Patterson, R. Sougrat, O.W. Lindwasser, S. Olenych, J.S. Bonifacino, M.W. Davidson, J. Lippincott-Schwartz, and H.F. Hess. Imaging intracellular fluorescent proteins at nanometer resolution. *Science*, 313:1643, 2006.

[25] Stephen W Paddock. Principles and practices of laser scanning confocal microscopy. *Molecular biotechnology*, 16(2):127–149, 2000.

[26] James Pawley. *Handbook of biological confocal microscopy*, volume 236. Springer Science & Business Media, 2006.

[27] Krzysztof Czamara, Katarzyna Majzner, Marta Z Pacia, K Kochan, Agnieszka Kaczor, and M Baranska. Raman spectroscopy of lipids: a review. *Journal of Raman Spectroscopy*, 46(1):4–20, 2015.

[28] Conor L. Evans and X. Sunney Xie. Coherent anti-stokes raman scattering microscopy: Chemical imaging for biology and medicine. *Annu. Rev. Anal. Chem.*, 1:883–909, 2008.

[29] Chi Zhang and Ji-Xin Cheng. Perspective: Coherent raman scattering microscopy, the future is bright. *Apl Photonics*, 3(9):090901, 2018.

[30] C.V. Raman and R.S. Krishnan. A new type of secondary radiation. *Nature*, 121:501–502, 1928.

[31] Andreas Zumbusch, Wolfgang Langbein, and Paola Borri. Nonlinear vibrational microscopy applied to lipid biology. *Progress in Lipid Research*, 52:615–632, 2013.

[32] John Paul Pezacki, Jessie A Blake, Dana C Danielson, David C Kennedy, Rodney K Lyn, and Ragunath Singaravelu. Chemical contrast for imaging living systems: molecular vibrations drive cars microscopy. *Nat. Chem. Biol.*, 7:137–145, 2011.

[33] M. Paar, C. Jüngst, N. A. Steiner, C. Magnes, F. Sinner, D. Kolb, A. Lass, R. Zimmermann, A. Zumbusch, S. D. Kohlwein, and H. Wolinski. Remodeling of lipid droplets during lipolysis and growth in adipocytes. *J Biol Chem*, 287(14):11164–73, 2012.

[34] Josephine Bradley, Iestyn Pope, Francesco Masia, Randa Sanusi, Wolfgang Langbein, Karl Swann, and Paola Borri. Quantitative imaging of lipids in live mouse oocytes and early embryos using cars microscopy. *Development*, 143(12):2238–2247, 2016.

[35] Fanghao Hu, Zhixing Chen, Luyuan Zhang, Yihui Shen, Lu Wei, and Wei Min. Vibrational imaging of glucose uptake activity in live cells and tissues by stimulated raman scattering. *Angewandte Chemie International Edition*, 54(34):9821–9825, 2015.

[36] Christian W. Freudiger, Wei Min, Brian G. Saar, Sijia Lu, Gary R. Holtom, Chengwei He, Jason C. Tsai, Jing X. Kang, and X. Sunney Xie. Label-free biomedical imaging with high sensitivity by stimulated raman scattering microscopy. *Science*, 322:1857, 2008.

[37] Milos Miljkovic, Tatyana Chernenko, Melissa J. Romeo, Benjamin Bird, Christian Matthaus, and Max Diem. Label-free imaging of human cells: algorithms for image reconstruction of raman hyperspectral datasets. *Analyst*, 135:2002–2013, 2010.

[38] Claudia Di Napoli, Francesco Masia, Iestyn Pope, Cees Otto, Wolfgang Langbein, and Paola Borri. Chemically-specific dual/differential cars microspectroscopy of saturated and unsaturated lipid droplets. *J. Biophotonics*, 7:68 – 76, 2014.

[39] Nils Billecke, Gianluca Rago, Madeleen Bosma, Gert Eijkel, Anne Gemmink, Philippe Leproux, Guillaume Huss, Patrick Schrauwen, Matthijs K. C. Hesselink, Mischa Bonn, and Sapun H. Parekh. Chemical imaging of lipid droplets in muscle tissues using hyperspectral coherent raman microscopy. *Histochem. Cell Biol.*, 141:263 – 273, 2014.

[40] M.D. Duncan, J. Reintjes, and T.J. Manuccia. Scanning coherent anti-stokes raman microscope. *Opt. Lett.*, 7(8):350–352, 1982.

[41] Ji-Xin Cheng and X Sunney Xie. Coherent anti-stokes raman scattering microscopy: instrumentation, theory, and applications. 2004.

[42] Dan Fu, Tong Ye, Thomas E Matthews, Gunay Yurtsever, and Warren S Warren Sr. Two-color, two-photon, and excited-state absorption microscopy. *Journal of biomedical optics*, 12(5):054004, 2007.

[43] Prathyush Samineni, Baolei Li, Jesse W Wilson, Warren S Warren, and Martin C Fischer. Cross-phase modulation imaging. *Optics letters*, 37(5):800–802, 2012.

[44] Shah Faisal B Mazhar and Robert R Alfano. Modulation instability induced by cross-phase modulation of transient stimulated raman scattering and self-phase modulation in calcite. *Optics Letters*, 45(11):3167–3170, 2020.

[45] Kristof Reynkens, Stéphane Clemmen, Haolan Zhao, Ali Raza, Tom Vanackere, Andim Stassen, Michiel Van Daele, Jolien Dendooven, and Roel Baets. Gold-induced photothermal background in on-chip surface enhanced stimulated raman spectroscopy. *Optics Letters*, 46(5):953–956, 2021.

[46] Stéphane Berciaud, David Lasne, Gerhard A Blab, Laurent Cognet, and Brahim Lounis. Photothermal heterodyne imaging of individual metallic nanoparticles: Theory versus experiment. *Physical Review B*, 73(4):045424, 2006.

[47] Pascal Berto, Esben Ravn Andresen, and Herv? Rigneault. Background-free stimulated raman spectroscopy and microscopy. *Phys. Rev. Lett.*, 112:053905, 2014.

[48] Hilde A. Rinia, Koert N. J. Burger, Mischa Bonn, and Michiel Müller. Quantitative label-free imaging of lipid composition and packing of individual cellular lipid droplets using multiplex cars microscopy. *Biophys. J.*, 95:4908–4914, 2008.

[49] Francesco Masia, Adam Glen, Phil Stephens, Paola Borri, and Wolfgang Langbein. Quantitative chemical imaging and unsupervised analysis using hyperspectral coherent anti-stokes raman scattering microscopy. *Anal. Chem.*, 85(22):10820–10828, 2013.

[50] Francesco Masia, Arnica Karuna, Paola Borri, and Wolfgang Langbein. Hyperspectral image analysis for cars, srs, and raman data. *J. Raman Spectrosc.*, 46(8):727–734, 2015.

[51] Feruz Ganikhanov, Conor L. Evans, Brian G. Saar, and X. Sunney Xie. High-sensitivity vibrational imaging with frequency modulation coherent anti-stokes raman scattering (FM CARS) microscopy. *Opt. Lett.*, 31:1872–74, 2006.

[52] Fake Lu, Wei Zheng, and Zhiwei Huang. Elliptically polarized coherent anti-stokes raman scattering microscopy. *Opt. Lett.*, 33:2842, 2008.

[53] Romedi Selm, Martin Winterhalder, Andreas Zumbusch, Günther Krauss, Tobias Hanke, Alexander Sell, and Alfred Leitenstorfer. Ultrabroadband background-free coherent anti-stokes raman scattering microscopy based on a compact er:fiber laser system. *Opt. Lett.*, 35(19):3282–3284, Oct 2010.

[54] Dmitry Pestov, Robert K. Murawski, Gombojav O. Ariunbold, Xi Wang, Miaochan Zhi, Alexei V. Sokolov, Vladimir A. Sautenkov, Yuri V. Rostovtsev, Arthur Dogariu, Yu Huang, and Marlan O. Scully. Optimizing the laser-pulse configuration for coherent raman spectroscopy. *Science*, 316:265–268, 2007.

[55] Wolfgang Langbein, Israel Rocha-Mendoza, and Paola Borri. Coherent anti-stokes raman micro-spectroscopy using spectral focusing: Theory and experiment. *J. Raman Spectrosc.*, 40:800–808, 2009.

[56] Israel Rocha-Mendoza, Wolfgang Langbein, Peter Watson, and Paola Borri. Differential coherent anti-stokes raman scattering microscopy with linearly-chirped femtosecond laser pulses. *Opt. Lett.*, 34:2258–2260, 2009.

[57] Iestyn Pope, Wolfgang Langbein, Peter Watson, and Paola Borri. Simultaneous hyperspectral differential-cars, tpf and shg microscopy with a single 5 fs ti:sa laser. *Opt. Express*, 21(6):7096–7106, 2013.

[58] Claudia Di Napoli, Iestyn Pope, Francesco Masia, Peter Watson, Wolfgang Langbein, and Paola Borri. Hyperspectral and differential cars microscopy for quantitative chemical imaging in human adipocytes. *Biomed. Opt. Express*, 5(5):1378–1390, May 2014.

[59] Ji-Xin Cheng, Andreas Volkmer, and X. Sunney Xie. Theoretical and experimental characterization of coherent anti-stokes raman scattering microscopy. *J. Opt. Soc. Am. B*, 19:1363, 2002.

[60] J.-X. Cheng and X.S. Xie. Coherent anti-stokes raman scattering microscopy: Instrumentation, theory, and applications. *J. Phys. Chem. B*, 108(3):827–840, 2004.

[61] Ji-xin Cheng, Andreas Volkmer, Lewis D. Book, and X. Sunney Xie. An epi-detected coherent anti-stokes raman scattering (e-cars) microscope with high spectral resolution and high sensitivity. *J. Phys. Chem. B*, 105(7):1277–1280, 2001.

[62] E. O. Potma and X. S. Xie. Detection of single lipid bilayers with coherent anti-stokes raman scattering (cars) microscopy. *J. Raman Spectrosc.*, 34:642, 2003.

[63] Erik T. Garbacik, Jeroen P. Korterik, Cees Otto, Jennifer L. Herek, and Herman L. Offerhaus. Epi-detection of vibrational phase contrast coherent anti-stokes raman scattering. *Opt. Lett.*, 39:5814–5817, 2014.

[64] Wolfgang Langbein, David Regan, Iestyn Pope, and Paola Borri. Invited article: Heterodyne dual-polarization epi-detected cars microscopy for chemical and topographic imaging of interfaces. *APL Photonics*, 3(9):092402, 2018.

[65] Wolfgang Langbein, Dafydd Sion Harlow, David Regan, Iestyn Pope, and Paola Borri. Heterodyne dual-polarization epi-detected cars microscopy for chemical and topographic imaging of interfaces. In *Label-free Biomedical Imaging and Sensing (LBIS) 2019*, volume 10890, page 1089003. International Society for Optics and Photonics, 2019.

[66] Eric O. Potma, Conor L. Evans, and X. Sunney Xie. Heterodyne coherent anti-stokes raman scattering (cars) imaging. *Opt. Lett.*, 31(2):241–243, Jan 2006.

[67] M. Jurna, J. P. Korterik, C. Otto, J. L. Herek, and H. L. Offerhaus. Vibrational phase contrast microscopy by use of coherent anti-stokes raman scattering. *Phys. Rev. Lett.*, 103:043905, Jul 2009.

[68] George Zoriniants, Francesco Masia, Naya Giannakopoulou, Wolfgang Langbein, and Paola Borri. Background-free 3d nanometric localization and sub-nm asymmetry detection of single plasmonic nanoparticles by four-wave mixing interferometry with optical vortices. *Phys. Rev. X*, 7:041022, Oct 2017.

[69] WE Moerner and David P Fromm. Methods of single-molecule fluorescence spectroscopy and microscopy. *Review of Scientific instruments*, 74(8):3597–3619, 2003.

[70] Lu Wei, Zhixing Chen, Lixue Shi, Rong Long, Andrew V Anzalone, Luyuan Zhang, Fanghao Hu, Rafael Yuste, Virginia W Cornish, and Wei Min. Super-multiplex vibrational imaging. *Nature*, 544(7651):465–470, 2017.

[71] Katrin Kneipp, Yang Wang, Harald Kneipp, Lev T Perelman, Irving Itzkan, Ramachandra R Dasari, and Michael S Feld. Single molecule detection using surface-enhanced raman scattering (sers). *Physical review letters*, 78(9):1667, 1997.

[72] Shuming Nie and Steven R Emory. Probing single molecules and single nanoparticles by surface-enhanced raman scattering. *science*, 275(5303):1102–1106, 1997.

[73] Pablo G Etchegoin and EC Le Ru. A perspective on single molecule sers: current status and future challenges. *Physical Chemistry Chemical Physics*, 10(40):6079–6089, 2008.

[74] Tae-Woong Koo, Selena Chan, and Andrew A Berlin. Single-molecule detection of biomolecules by surface-enhanced coherent anti-stokes raman scattering. *Optics letters*, 30(9):1024–1026, 2005.

[75] Steven Yampolsky, Dmitry A Fishman, Shirshendu Dey, Eero Hulkko, Mayukh Banik, Eric O Potma, and Vartkess A Apkarian. Seeing a single molecule vibrate through time-resolved coherent anti-stokes raman scattering. *Nature Photonics*, 8(8):650–656, 2014.

[76] Yu Zhang, Yu-Rong Zhen, Oara Neumann, Jared K. Day, Peter Nordlander, and Naomi J. Halas. Coherent anti-stokes raman scattering with single-molecule sensitivity using a plasmonic fano resonance. *Nat. Commun.*, 5:4424, 2014.

[77] Marek Cebecauer, Mariana Amaro, Piotr Jurkiewicz, Maria Joao Sarmento, Radek Sachl, Lukasz Cwiklik, and Martin Hof. Membrane lipid nanodomains. *Chemical reviews*, 118(23):11259–11297, 2018.

[78] Ilya Levental, Kandice R Levental, and Frederick A Heberle. Lipid rafts: controversies resolved, mysteries remain. *Trends in cell biology*, 30(5):341–353, 2020.

[79] Robert W. Boyd. *Nonlinear Optics*. Elsevier, 2003.

[80] Hervé Rigneault and Pascal Berto. Tutorial: Coherent raman light matter interaction processes. *Apl Photonics*, 3(9):091101, 2018.

[81] Shaowei Li, Yanping Li, Rongxing Yi, Liwei Liu, and Junle Qu. Coherent anti-stokes raman scattering microscopy and its applications. *Frontiers in Physics*, 8:515, 2020.

[82] Bahaa E. A. Saleh and Malvin Carl Teich. *Fundamentals of photonics*. John Wiley & Sons, Ltd, 2007.

[83] Vincenzo Amendola, Roberto Pilot, Marco Frasconi, Onofrio M Maragò, and Maria Antonia Iatì. Surface plasmon resonance in gold nanoparticles: a review. *Journal of Physics: Condensed Matter*, 29(20):203002, 2017.

[84] Eric Le Ru and Pablo Etchegoin. *Principles of Surface-Enhanced Raman Spectroscopy: and related plasmonic effects*. Elsevier, 2008.

[85] Judith Langer, Dorleta Jimenez de Aberasturi, Javier Aizpurua, Ramon A Alvarez-Puebla, Baptiste Auguié, Jeremy J Baumberg, Guillermo C Bazan, Steven EJ Bell, Anja Boisen, Alexandre G Brolo, et al. Present and future of surface-enhanced raman scattering. *ACS nano*, 14(1):28–117, 2019.

[86] Jie Cao, Tong Sun, and Kenneth TV Grattan. Gold nanorod-based localized surface plasmon resonance biosensors: A review. *Sensors and actuators B: Chemical*, 195:332–351, 2014.

[87] Xuan Yang, Miaoxin Yang, Bo Pang, Madeline Vara, and Younan Xia. Gold nanomaterials at work in biomedicine. *Chemical reviews*, 115(19):10410–10488, 2015.

[88] Feng Wang and Y Ron Shen. General properties of local plasmons in metal nanostructures. *Physical review letters*, 97(20):206806, 2006.

[89] Jing Wang, Yiting Chen, Xi Chen, Jiaming Hao, Min Yan, and Min Qiu. Photothermal reshaping of gold nanoparticles in a plasmonic absorber. *Optics express*, 19(15):14726–14734, 2011.

[90] Stephan Link, Clemens Burda, B Nikoobakht, and Mostafa A El-Sayed. Laser-induced shape changes of colloidal gold nanorods using femtosecond and nanosecond laser pulses. *The Journal of Physical Chemistry B*, 104(26):6152–6163, 2000.

[91] A Plech, V Kotaidis, S Grésillon, C Dahmen, and G Von Plessen. Laser-induced heating and melting of gold nanoparticles studied by time-resolved x-ray scattering. *Physical Review B*, 70(19):195423, 2004.

[92] Ekaterina Y Lukianova-Hleb, Lindsey JE Anderson, Seunghyun Lee, Jason H Hafner, and Dmitri O Lapotko. Hot plasmonic interactions: a new look at the photothermal efficacy of gold nanoparticles. *Physical Chemistry Chemical Physics*, 12(38):12237–12244, 2010.

[93] Gelon Albrecht, Monika Ubl, Stefan Kaiser, Harald Giessen, and Mario Hentschel. Comprehensive study of plasmonic materials in the visible and near-infrared: linear, refractory, and nonlinear optical properties. *Acs Photonics*, 5(3):1058–1067, 2018.

[94] Hyunho Kang, Joseph T Buchman, Rebeca S Rodriguez, Hattie L Ring, Jiayi He, Kyle C Bantz, and Christy L Haynes. Stabilization of silver and gold nanoparticles: preservation and improvement of plasmonic functionalities. *Chemical reviews*, 119(1):664–699, 2018.

[95] Stefan Iglauer, Abdulsalam Salamah, Mohammad Sarmadivaleh, Keyu Liu, and Chi Phan. Contamination of silica surfaces: Impact on water co2 quartz and glass contact angle measurements. *International Journal of Greenhouse Gas Control*, 22:325–328, 2014.

[96] Ramadan Abd-Allah. Chemical cleaning of soiled deposits and encrustations on archaeological glass: A diagnostic and practical study. *Journal of Cultural Heritage*, 14(2):97–108, 2013.

[97] H Caro. Hauptversammlung des vereins deutscher chemiker am 1. bis 4. juni 1898 zu darmstadt. *Angew. Chem.*, 11:845–846, 1898.

[98] Damon Diemente. The hydronium ion: How do we know? *Journal of Chemical Education*, 68(7):568, 1991.

[99] Robert Acres, Amanda Ellis, Jason Alvino, Claire Lenehan, Dmitriy Khodakov, Gregory Metha, and Gunther Andersson. Molecular structure of 3-aminopropyltriethoxysilane layers formed on silanol-terminated silicon surfaces, 02 2012.

[100] J Canning, I Petermann, and K Cook. Surface treatment of silicate based glass: base piranha treatment versus 193nm laser processing. In *Third Asia Pacific Optical Sensors Conference*, volume 8351, page 83512N. International Society for Optics and Photonics, 2012.

[101] Jaideep Chatterjee. Limiting conditions for applying the spherical section assumption in contact angle estimation. *J. Colloid Interface Sci.*, 259(1):139 – 147, 2003.

[102] Charles A Goss, Deborah H Charych, and Marcin Majda. Application of (3-mercaptopropyl) trimethoxysilane as a molecular adhesive in the fabrication of vapor-deposited gold electrodes on glass substrates. *Analytical Chemistry*, 63(1):85–88, 1991.

[103] Yasuro Niidome, Hironobu Takahashi, Shinji Urakawa, Koji Nishioka, and Sunao Yamada. Immobilization of gold nanorods on the glass substrate by the electrostatic interactions for localized plasmon sensing. *Chemistry Letters*, 33(4):454–455, 2004.

[104] Annabelle Bertin and Helmut Schlaad. Mild and versatile (bio-) functionalization of glass surfaces via thiol- ene photochemistry. *Chemistry of Materials*, 21(24):5698–5700, 2009.

[105] Maroua Ben Haddada, Juliette Blanchard, Sandra Casale, Jean-Marc Krafft, Anne Vallée, Christophe Méthivier, and Souhir Boujday. Optimizing the immobilization of gold nanoparticles on functionalized silicon surfaces: amine-vs thiol-terminated silane. *Gold Bulletin*, 46(4):335–341, 2013.

[106] Lukas M. Payne, Wolfgang Langbein, and Paola Borri. Erratum: Polarization-resolved extinction and scattering cross-sections of individual gold nanoparticles measured by wide-field microscopy on a large ensemble [appl. phys. lett. 102, 131107 (2013)]. *Appl. Phys. Lett.*, 110(22):229901, 2017.

[107] Lukas M. Payne, Wolfgang Langbein, and Paola Borri. Wide-field imaging of single-nanoparticle extinction with sub-nm^2 sensitivity. *Phys. Rev. Appl*, 9:034006, 2018.

[108] Lukas M Payne, Wiebke Albrecht, Wolfgang Langbein, and Paola Borri. The optical nanosizer–quantitative size and shape analysis of individual nanoparticles by high-throughput widefield extinction microscopy. *Nanoscale*, 12(30):16215–16228, 2020.

[109] Wolfgang Langbein, Israel Rocha-Mendoza, and Paola Borri. Single source coherent anti-stokes raman microspectroscopy using spectral focusing. *Appl. Phys. Lett.*, 95(8):081109, 2009.

[110] Jialin Ma and Mengtao Sun. Nonlinear optical microscopies (noms) and plasmon-enhanced noms for biology and 2d materials. *Nanophotonics*, 9(6):1341–1358, 2020.

[111] EJ Liang, A Weippert, J-M Funk, A Materny, and W Kiefer. Experimental observation of surface-enhanced coherent anti-stokes raman scattering. *Chemical physics letters*, 227(1-2):115–120, 1994.

[112] Christian Steuwe, Clemens F Kaminski, Jeremy J Baumberg, and Sumeet Mahajan. Surface enhanced coherent anti-stokes raman scattering on nanostructured gold surfaces. *Nano letters*, 11(12):5339–5343, 2011.

[113] Jiapeng Zheng, Xizhe Cheng, Han Zhang, Xiaopeng Bai, Ruoqi Ai, Lei Shao, and Jianfang Wang. Gold nanorods: The most versatile plasmonic nanoparticles. *Chemical Reviews*, 121(21):13342–13453, 2021.

[114] Erik C. Dreaden, Alaaldin M. Alkilany, Xiaohua Huang, Catherine J. Murphy, and Mostafa A. El-Sayed. The golden age: Gold nanoparticles for biomedicine. *Chem. Soc. Rev.*, 41(7):2740–2779, 2012.

[115] Maria Lasalvia, Giuseppe Perna, and Vito Capozzi. Biochemical changes in human cells exposed to low concentrations of gold nanoparticles detected by raman microspectroscopy. *Sensors*, 19(10):2418, 2019.

[116] Andrew M Fales, William C Vogt, Keith A Wear, Ilko K Ilev, and T Joshua Pfefer. Pulsed laser damage of gold nanorods in turbid media and its impact on multi-spectral photoacoustic imaging. *Biomedical optics express*, 10(4):1919–1934, 2019.

[117] Song-Yuan Ding, Jun Yi, Jian-Feng Li, Bin Ren, De-Yin Wu, Rajapandiyan Panneerselvam, and Zhong-Qun Tian. Nanostructure-based plasmon-enhanced raman spectroscopy for surface analysis of materials. *Nature Reviews Materials*, 1(6):1–16, 2016.

[118] Guillermo González Rubio, Andrés Guerrero-Martínez, and Luis M Liz Marzan. Reshaping, fragmentation, and assembly of gold nanoparticles assisted by pulse lasers. *Accounts of chemical research*, 49(4):678–686, 2016.

[119] Valentina Piotto, Lucio Litti, and Moreno Meneghetti. Synthesis and shape manipulation of anisotropic gold nanoparticles by laser ablation in solution. *The Journal of Physical Chemistry C*, 124(8):4820–4826, 2020.

[120] Mohamad G Banaee and Kenneth B Crozier. Mixed dimer double-resonance substrates for surface-enhanced raman spectroscopy. *ACS nano*, 5(1):307–314, 2011.

[121] Kristin L Wustholz, Anne-Isabelle Henry, Jeffrey M McMahon, R Griffith Freeman, Nicholas Valley, Marcelo E Piotti, Michael J Natan, George C Schatz, and Richard P Van Duyne. Structure- activity relationships in gold nanoparticle dimers and trimers for surface-enhanced raman spectroscopy. *Journal of the American Chemical Society*, 132(31):10903–10910, 2010.

[122] Jia Zhang, Shu Chen, Junqiao Wang, Kaijun Mu, Chunzhen Fan, Erjun Liang, and Pei Ding. An engineered cars substrate with giant field enhancement in crisscross dimer nanostructure. *Scientific reports*, 8(1):1–9, 2018.

[123] Jinna He, Chunzhen Fan, Pei Ding, Shuangmei Zhu, and Erjun Liang. Near-field engineering of fano resonances in a plasmonic assembly for maximizing cars enhancements. *Scientific reports*, 6(1):1–8, 2016.

[124] Amy M Michaels, Jiang Jiang, and Louis Brus. Ag nanocrystal junctions as the site for surface-enhanced raman scattering of single rhodamine 6g molecules. *The Journal of Physical Chemistry B*, 104(50):11965–11971, 2000.

[125] Kevin T Crampton, Alexander Fast, Eric O Potma, and V Ara Apkarian. Junction plasmon driven population inversion of molecular vibrations: a picosecond surface-enhanced raman spectroscopy study. *Nano letters*, 18(9):5791–5796, 2018.

[126] Michael Galperin. Photonics and spectroscopy in nanojunctions: a theoretical insight. *Chemical Society Reviews*, 46(13):4000–4019, 2017.

[127] Prashant K Jain, Susie Eustis, and Mostafa A El-Sayed. Plasmon coupling in nanorod assemblies: optical absorption, discrete dipole approximation simulation, and exciton-coupling model. *The Journal of Physical Chemistry B*, 110(37):18243–18253, 2006.

[128] Alison M Funston, Carolina Novo, Tim J Davis, and Paul Mulvaney. Plasmon coupling of gold nanorods at short distances and in different geometries. *Nano letters*, 9(4):1651–1658, 2009.

[129] Victor Deinhart, Lisa-Marie Kern, Jan N Kirchhof, Sabrina Juergensen, Joris Sturm, Enno Krauss, Thorsten Feichtner, Sviatoslav Kovalchuk, Michael Schneider, Dieter Engel, et al. The patterning toolbox fib-o-mat: Exploiting the full potential of focused helium ions for nanofabrication. *Beilstein journal of nanotechnology*, 12(1):304–318, 2021.